The Only Constant is Change: Dynamics and Stability in On-chip Nanoscale Semiconductor Lasers for Phased Arrays

Jiang, Sizhu

2022

UNIVERSITY OF CALIFORNIA SAN DIEGO

The Only Constant is Change: Dynamics and Stability in On-chip Nanoscale Semiconductor Lasers for Phased Arrays

A Dissertation submitted in partial satisfaction of
the requirements for the degree
Doctor of Philosophy

in

Electrical Engineering (Photonics)

by

Sizhu Jiang

Committee in charge:

Professor Yeshaiahu Fainman, Chair
Professor Ertugrul Cubukcu
Professor Zhaowei Liu
Professor Paul Siegel

2022

The Dissertation of Sizhu Jiang is approved, and it is acceptable in quality and form for publication on microfilm and electronically.

University of California San Diego

2022

DEDICATION

To my mom and dad for their endless love and support.

To my significant other Victor Gunawan for the encouragement and companion.

To my puppies Mellow, Meehoo, and Meeno for the joy they bring.

TABLE OF CONTENTS

LIST OF FIGURES

LIST OF TABLES

ACKNOWLEDGEMENTS

I would like to first thank my mentor Professor Yeshaiahu Fainman who always believes in me and supports me. Without your mentorship and guidance in both research and life, I would not be able to thrive! I also want to thank all my academic mentors for their guidance.

I would also like to thank my colleagues and friends Dr. Si Hui Pan and Dr. Suruj Deka for the valuable guidance and discussions with your endless patience. Thank you for treating me like a sister and making me feel not lonely on this tough road. I would also like to thank Dr. Phuong H. L. Nguyen and Dr. Jordan Davis for your friendship and support. I also want to thank Dr. Cheng-Yi Fang and Dr. Mu-Han Yang for generously passing your knowledge and skills to me. I would like to thank all my colleagues for your help.

I would like to thank all the past and present Nano3 staff members for the help.

Finally, I would like to express my deepest gratitude to my mom and dad, my significant other Victor Gunawan, and my cutest puppies Mellow, Meehoo, and Meeno. Your love and support are the biggest reasons that make this long journey possible. I am very lucky as your daughter, your love, and your mom.

Chapter 2, in part, is a reprint of the material as it appears in S. Jiang, S. S. Deka, S. H. Pan, and Y. Fainman, “Effects of High-β on Phase-Locking Stability and Tunability in Laterally Coupled Lasers”, *IEEE Journal of Selected Topics in Quantum Electronics*, vol. 28, no. 1, Jan./Feb. 2022. The dissertation author was the primary investigator and author of the publications and the unpublished materials.

Chapter 3, in part, is a reprint of the material as it appears in S. Jiang, D. Belogovskii, S. S. Deka, S. H. Pan, and Y. Fainman, “Experimental Demonstration of Mode Selection in Bridge-Coupled Metallo-Dielectric Nanolasers”, *Optics Letters*, vol. 46, no. 23, Dec. 2021. The dissertation author was the primary investigator and author of the publications and the unpublished materials.

Chapter 4, in part, is a reprint of the material as it appears in S. Jiang, S. H. Pan, S. S. Deka, C.-Y. Fang, Z. Chen, Y. Fainman and A. El Amili, “Impact of Fundamental Temperature Fluctuations on the Frequency Stability of Metallo-Dielectric Nanolasers”, *IEEE Journal of Quantum Electronics*, vol. 55, no. 5, Oct. 2019. The dissertation author was the primary investigator and author of the publications and the unpublished materials. Chapter 4 also contains unpublished materials. The dissertation author was the primary author of this part.

Chapter 5, in part, is a reprint of the material as it appears in S. S. Deka, S. Jiang, S. H. Pan and Y. Fainman, “Nanolaser arrays: toward application-driven dense integration”, *Nanophotonics*, vol. 10, no. 1, Jan. 2021.The dissertation author contributed towards the literature review and manuscript writing of this work.

VITA

2017	Bachelor of Science in Electrical Engineering, Beijing University of Posts and Telecommunications
2019	Master of Science in Electrical Engineering (Photonics), University of California San Diego
2022	Doctor of Philosophy in Electrical Engineering (Photonics), University of California San Diego

PUBLICATIONS

Journal articles:

- **S. Jiang**, S. H. Pan, S. S. Deka, C.-Y. Fang, Z. Chen, Y. Fainman and A.El Amili, "Impact of Fundamental Temperature Fluctuations on the Frequency Stability of Metallo-Dielectric Nanolasers", *IEEE Journal of Quantum Electronics*, vol. 55, no. 5, Oct. 2019.

- **S. Jiang***, S. S. Deka*, S. H. Pan, and Y. Fainman, "Effects of High-β on Phase-Locking Stability and Tunability in Laterally Coupled Lasers", *IEEE Journal of Selected Topics in Quantum Electronics*, vol. 28, no. 1, Jan./Feb. 2022.

- **S. Jiang**, D. Belogolovskii, S. S. Deka, S. H. Pan, and Y. Fainman, "Experimental Demonstration of Mode Selection in Bridge-Coupled Metallo-Dielectric Nanolasers", *Optics Letters*, vol. 46, no. 23, Dec. 2021.

- S. S. Deka, **S. Jiang**, S. H. Pan and Y. Fainman, "Nanolaser arrays: toward application-driven dense integration", *Nanophotonics*, vol. 10, no. 1, Jan. 2021.

- S. S. Deka, S. H. Pan, **S. Jiang**, A. E. Amili, F. Vallini, Q. Gu, and Y. Fainman, "Real-time dynamic wavelength tuning and intensity modulation of metal-clad nanolasers", *Optics Express*, vol. 28, no. 19, Sep. 2021.

- Z. Chen, S. S. Deka, S. H. Pan, **S. Jiang**, C. -Y. Fang, Y. Fainman, and A. El Amili, "Intensity noise and bandwidth analysis of nanolasers via optical injection", *Optics Express*, vol. 27, no. 6, Mar. 2019.

Conference presentations:

- **S. Jiang**, S. H. Pan, S. S. Deka, C.-Y. Fang, Z. Chen, Y. Fainman and A.El Amili, "Linewidth Broadening Induced by Fundamental Thermal Fluctuations in Metallo-Dielectric Nanolasers", *CLEO 2020*, JTu2D.4, May 2020.

- **S. Jiang,** S. S. Deka, S. H. Pan and Y. Fainman, "Effects of High-β on the Stability of Phase-locking in Coupled Semiconductor Lasers", *CLEO 2022,* SM3G, May 2022.

- **S. Jiang,** D. Belogolovskii, S. S. Deka, S. H. Pan, and Y. Fainman, "Experimental Demonstration of Mode Selection in Metallo-Dielectric Nanolasers Coupled via a Bridge", *CLEO 2022,* STu4E, May 2022.

- Y. Fainman and **S. Jiang**, "Nanolasers: dynamics and phase locking", *SPIE OPTO*, 116841C, Mar. 2021.

- Y. Fainman and **S. Jiang**, "Nanolasers: towards large-scale phase-locked laser arrays", 67th IEDM, 19-3, Dec. 2021.

- Y. Fainman, S. H. Pan, S. Deka, **S. Jiang**, and A. El Amili, "Heterogeneously integrated on-chip nanolasers", 14th *CLEO: Pacific Rim,* C1C_1, Aug. 2020.

ABSTRACT OF THE DISSERTATION

The Only Constant is Change:
Dynamics and Stability in
On-chip Nanoscale Semiconductor Lasers for Phased Arrays

by

Sizhu Jiang

Doctor of Philosophy in Electrical Engineering (Photonics)

University of California San Diego, 2022

Professor Yeshaiahu Fainman, Chair

The last two decades have witnessed the fruitful research on nanoscale semiconductor lasers due to their compact footprint, low energy consumption and fast modulation speed, that are advantageous merits for nanolasers serving as light sources in future ultra-dense photonic integrated circuits (PIC). Previously, most of the research efforts have focused on the demonstration of individual devices with improving performance. Recently, there has been escalating interest in investigating the interaction of dual nanolasers, aiming at exploring the behavior of larger-size laser arrays. Before applying nanolasers in future laser array systems, certain aspects require further investigation, where this dissertation aims to fill the blank. While most of the laser parameters that have impact on the phase-locking stability of coupled nanolasers are studied in previous literatures, spontaneous emission factor has not been explored. This can be justified by the fact that conventional semiconductor has negligible spontaneously emitted photons funneling into the lasing mode due to their comparably large dimension. The compact resonator size of nanoscale lasers leads to pronounced spontaneous emission factor and necessitates research effort in evaluating the phase-locking stability on such factor. In Chapter 2, we have employed the bifurcation analysis based on the coupled laser rate equations and presented the theoretical impact of spontaneous emission factor on the nonlinear dynamics of coupled nanolasers. We show that the stability is enhanced with increasing spontaneous emission factor, which indicates the huge potential of nanolasers being applied in array forms. To experimentally access the requirement for such stability, we have engineered a novel coupling geometry in Chapter 3. By controlling the coupling bridge that locates in between two nanolasers, we have shown that either an in-phase or out-of-phase mode can be selected, which is confirmed by the experimental results. In Chapter 4, we have theoretically explained the broad linewidths in nanolasers, focusing on the thermal noise and intensity noise inside these nanoscale cavities. We have observed that the fundamental thermal fluctuation is a huge contribute towards the measured linewidth at room temperature, that is on the order of 1nm. In Chapter 5, we have reviewed some recent progress that researchers have made in building dense nanolaser arrays with applications ranging from biosensing to long-haul communications. Chapter 6 concludes the thesis and discusses some future directions that remain to explore.

Chapter 1 Introduction

Nanolasers with the capability of generating coherent light in small volume resonators have become promising on-chip light sources for future ultra-compact photonic integrated circuits. They have outstanding merits such as ultra-small footprint and low power consumption that meet the need the various applications ranging from biosensing [1, 2], super-resolution imaging [3, 4], chemical detection [5-7], to optical interconnects for large data centers [8] and optical computing [9].

By far, nanolasers with various architectures have been demonstrated based on III-V gain materials, such as photonic crystal lasers [10-15], plasmonic lasers (SPASERs) [16-21], nanowires [22, 23], metal-clad coaxial cavities [24], and metallo-dielectric nanolasers [25-33], as shown in Figure **1.1**. Due to the ultra-compact mode volumes of nanolasers, they have intrinsically high spontaneous emission factors due to the suppression of spontaneously emitted photons into the non-lasing mode and free-space modes [15, 34, 35]. Therefore, low lasing threshold and high energy efficiency can be achieved as most of the spontaneous emission funnels into the lasing mode. The enhanced spontaneous emission due to Purcell effect can further accelerate the carrier response rate in nanocavities, which leads to potential fast modulation speed of over 100GHz in these nanolasers [36]. Furthermore, the lasing action of these high-β nanolasers that is difficult to identify through conventional light-in-light-out characterization [10-33] can be confirmed by the second-order intensity correlation measurements [37].

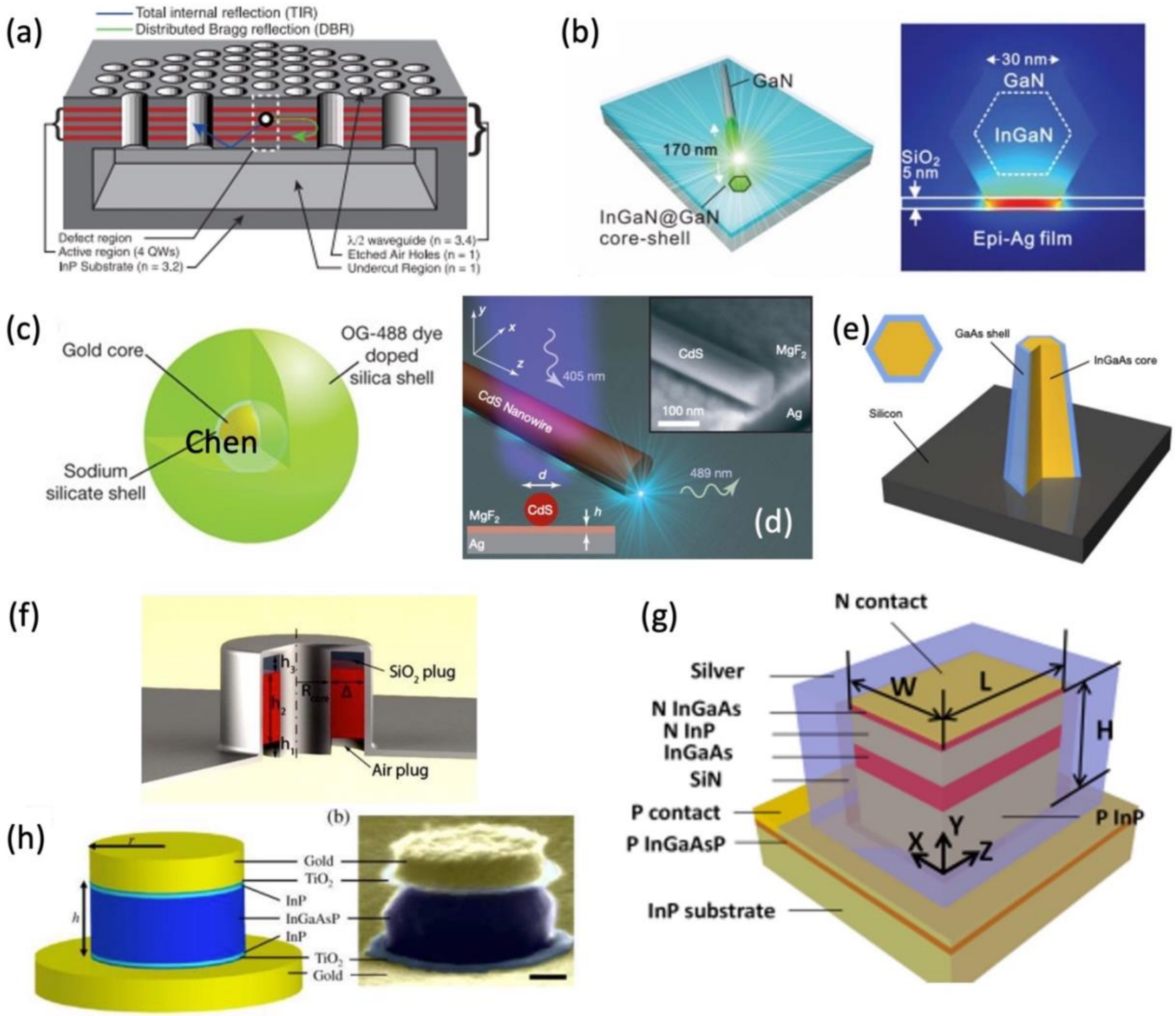

Figure 1.1 Examples of nanolasers. Schematics of (a) a photonic crystal nanolaser (reprinted from [11]); (b) a nanorod laser based on surface plasmon amplification by stimulated emission of radiation (SPASER) and its electromagnetic energy distribution (reprinted from [16]); (c) a hybrid nanopartical SPASER (reprinted from [17]); (d) a SPASER based on CdS semiconductor nanowires (reprinted from [18]); (e) a nanopillar laser monolithically grown on silicon (reprinted from [22]); (f) a metal-clad coaxial nanolaser (reprinted from [24]); (g) a metal-clad photonic-mode nanolaser (reprinted from [25]); and (h) a metallo-dielectric nanopatch semiconductor laser and its scanning electron microscope image (reprinted from [26]).

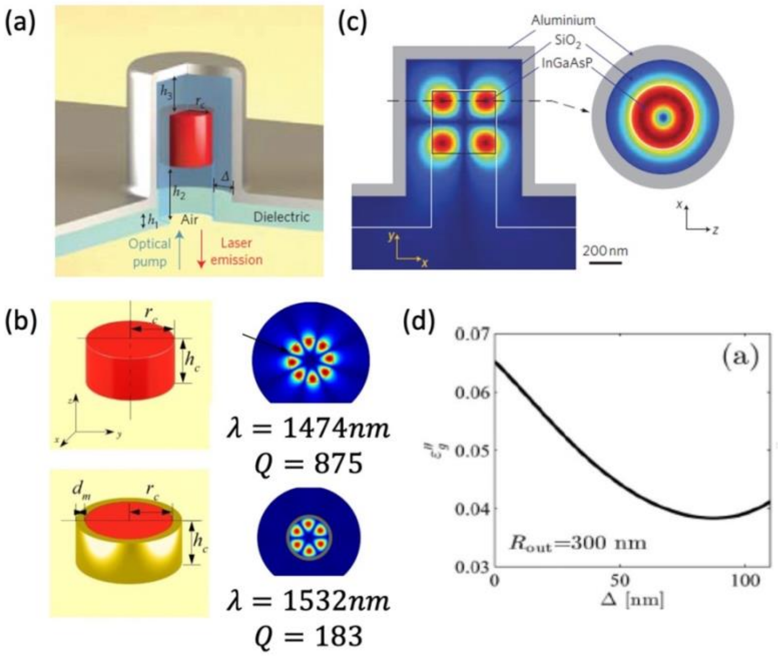

Figure 1.2 (a) Schematic of optically pumped metallo-dielectric nanolaser. (b) Schematic (left) and mode profiles (right) of nanolasers without (top) and with (bottom) metal claddings. (c) Mode profiles of the metallo-dielectric nanolaser. Reprinted from [28]. (d) Threshold gain as a function of dielectric thickness. Reprinted from [38].

While nanolasers with photonic cavity usually suffer from low optical confinement and/or large cavity dimension that can be on the order of micrometers [10-15], those based on plasmonic cavities have intrinsically large dissipation losses due to the utilization of metal [16-21]. Metallo-dielectric nanolasers combine the advantages of photonic and plasmonic cavities, leading to ultra-compact footprint in all three dimensions and low lasing threshold for room-temperature operations [25-33]. A schematic of a metallo-dielectric nanolaser is shown in Figure **1.2**. To confine the optical mode in all three dimensions and increase the light matter interactions in nanocavities, metal cladding is employed as the cavity mirrors [28]. However, the optical mode overlaps with the lossy metal will leverage the lasing threshold of the nanolasers. To overcome this issue, the researchers have inserted a layer of low-index dielectric shield in between the gain region and the metal cladding in their design to push the optical mode away from the metal walls.

The thickness of the dielectric layer is further optimized to reach the minimum lasing threshold [38]. Furthermore, the researchers have replaced the SiO_2 dielectric in their initial design with Al_2O_3 due to the better heat dissipation of the latter. Therefore, room-temperature operated metallo-dielectric nanolasers with the following advantages, including sub-wavelength footprint in 3D, electromagnetic isolation provided by the metal cladding, telecommunication wavelength operation, energy efficiency and potential high modulation speed have been successfully demonstrated [39, 40].

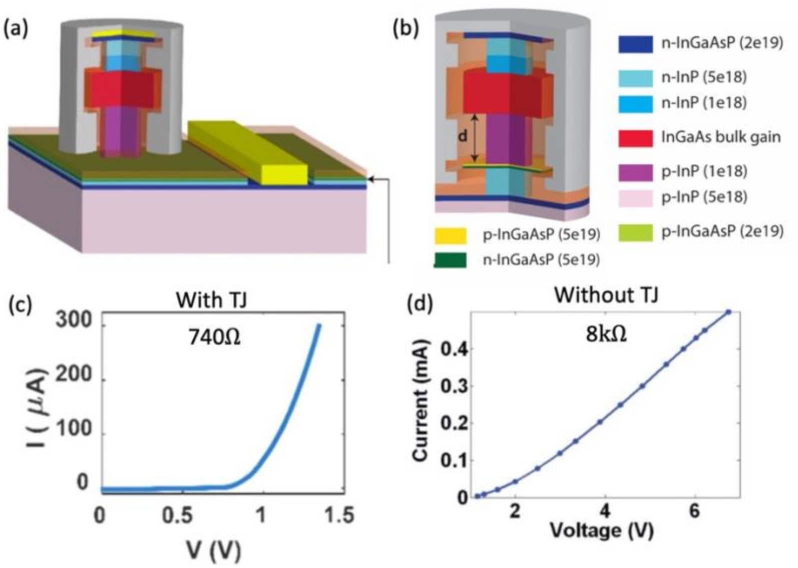

Figure 1.3 (a) Schematic, (b) epitaxial layers, and (c) I-V curve of the electrically pumped metallo-dielectric nanolaser with tunnel junction. (a) is reprinted from [41. (b) and (c) are reprinted from [42]. (d) I-V curve of the same nanolaser design but without tunnel junctions. Reprinted from [43].

In Figure **1.2**, an air gap below the gain region is formed for optical pumping [28, 37, 40]. To make nanolasers useful for practical on-chip application, current injection is required [25, 31, 33]. For this propose, electrically pump nanolasers have also been designed, whose schematic is shown in Figure **1.3** [41, 42]. Conventional current injected nanolasers utilizes metal contacts that are connected to heavily n- and p-doped InP layers. Due to their small contact regions and the high-resistance of p-type contact, these nanolasers suffer from prohibitively high threshold voltage, and ultimately limiting performance due to the Joule heating [34]. The electrically pumped nanolasers demonstrated in [41] incorporate a tunnel junction to alleviate the heating problem. The presence of the tunnel junction under negligible reversed bias allows current being injected into the active region effectively by replacing the bottom p-type contact with another n-type contact with much lower resistance [41, 42]. Compared to the conventional architecture, this novel design reduces the device resistance by an order of magnitude [43] and leverages the operating temperature to record 180K [41].

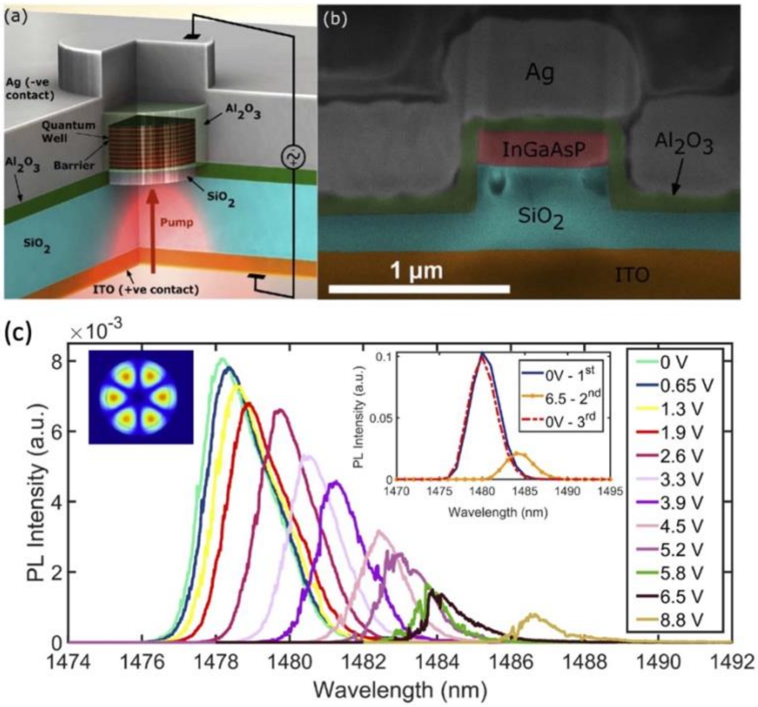

Figure 1.4 (a) Schematic of the direct modulated optically pumped nanolaser. (b) Cross-section of the fabricated devices. (c) Emission spectra with increasing applied voltages. Reprinted from [44].

Based on the successful device-level demonstration, fascinating research has been conducted on metallo-dielectric nanolasers to demonstrate their potential for future on-chip applications. Deka et al. has reported the first direct intensity modulation of metal-clad nanolasers with wavelength tunability, which is well-suited for chip-scale wavelength division multiplexing

(WDM) applications (see Figure **1.4**) [44]. By applying DC voltage across the multiple quantum wells, a tuning sensitivity, defined as $\Delta\lambda/\Delta V$, of ~1.01nm/V has been achieved. For the proof of concept, the nanolasers can be modulated up to 400MHz, which is limited by the detector bandwidth. Xu et al. has reported the intrinsic frequency response of metal-clad nanolasers that are both theoretically evaluated and experimentally investigated [45]. A 3-dB modulation bandwidth of 9GHz with low pumping rate of $0.25mW/\mu m^2$ has been reported, that is an order of magnitude larger than that of other semiconductor lasers. Although essential work needs be done to push the modulation speed of metal-clad nanolasers to the theoretical values of beyond 100GHz, these works pave the way for applying fast nanolasers as light-sources for future photonic circuits [46-50].

Leveraging the knowledge about individual nanolasers, the next phase of nanolaser research would be geared toward the interaction of two nanolasers, and ultimately scaling up design to form arrays for applications ranging from biological sensing [51], bioimaging [52], Lidar systems [53], cryptography [54], to long-range communications [55] and defense systems. A dual nanolaser system can be regarded as a unit cell or building block that can help understand the behaviors to be expected in larger lattices, and therefore is extensively investigated. Deka et al. has demonstrated that even with metal claddings, two nanolasers in close proximity (<100nm) can still interact with each other as their evanescent waves tunnel through the barrier region [39]. Such coupling gives rise to the creation of two supermodes, i.e., the so-called bonding (in-phase) mode and antibonding (out-of-phase) mode. The characteristic splitting of the two supermodes in both frequency and loss can be observed as the two cavities approach each other (see Figure **1.5**). Similar supermodes creation is also reported for other nanolaser systems, such as photonic crystals [56, 57]. Moreover, the coupling behaviors of these devices can be tailored by the physical geometry of them. For example, Haddadi et al. show in their study that the varying size of the holes in the barrier region of the evanescently coupled photonic crystal nanolasers, both the amount of wavelength splitting as well as the excited state mode can be selected [57].

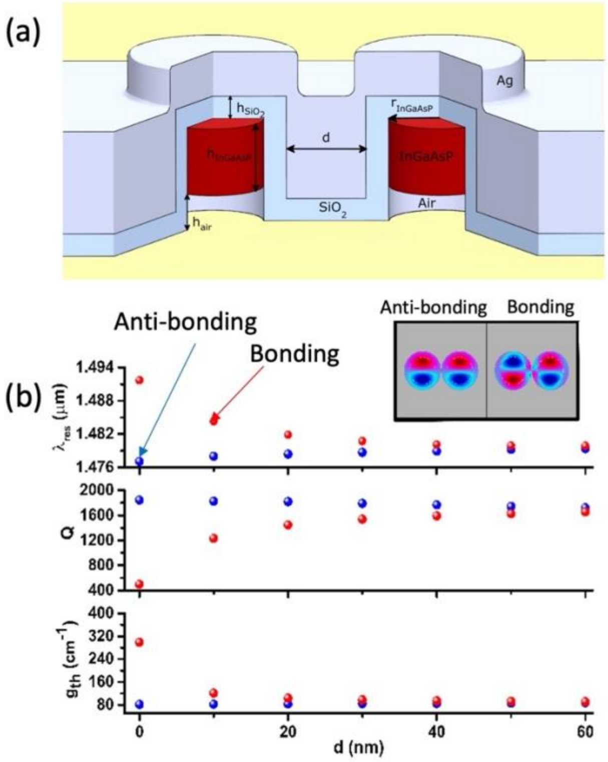

Figure 1.5 (a) Schematic of evanescently coupled metallo-dielectric nanolasers. (b) Frequency, qualify factors, and threshold gain of the bonding and antibonding modes [39].

Besides the supermodes, the coupling between nanolasers also produce rich nonlinear dynamics due to multiple factors including distinct time scales of photons and carriers, differences in the laser dimensions, and amplitude-phase coupling for semiconductor materials. These dynamics can be theoretically predicted by the coupled laser rate equations with varying control parameters, such as pump rate, coupling strength, and dimension difference. By controlling these parameters, interesting phenomenon has been observed, including spontaneous symmetry breaking [56], asymmetric mode scattering [58], radio frequency (RF) oscillation [59], and chaotic synchronization [60], that can be essential for designing novel photonic devices. Although the impact of a variety of important parameters such as current injection rate, linewidth enhancement factor, carrier and photon lifetimes has been addressed in these analysis [59, 61-65], one parameter that has always been neglected is the spontaneous emission factor β. As the rapid development of nanolasers with intrinsic high-β factors in the past two decades, it becomes necessary to investigate how the β-factors affect the nonlinear dynamics of coupled lasers. Among various types of dynamics, phase-locking stability has been extensively investigated owing to the potential of phase-locked nanolasers in generating high-power and coherent optical beams if all the elements are locked in-phase [52, 55, 66]. Therefore, in Chapter 2, we have applied bifurcation analysis to evaluate the impact of β values on the stability of coupled semiconductor lasers by numerically solving the coupled laser rate equations with β ranging from 10^{-5} to the theoretical limit of 1. Such study is essential to answer the question of whether nanolasers are suitable for building large-size arrays.

To scale up the chip-scale phase-locked laser arrays, in-depth understanding of their building blocks in the form of dual coupled lasers is important, which can be theoretically evaluated by the dynamical analysis in Chapter 2. It is imperative to design a building block that can operate in the in-phase mode, as the constructive interference can leads to efficient power scaling. However, the conventional strategies to attain the in-phase locking, such as gain-guiding [63], global antenna coupling [67], and diffractive coupling via Talbot effect [68] are not suitable for metal-clad nanolasers due to the limitation of the device dimensions and increase the fabrication complexity. In Chapter 3, we have employed the bifurcation analysis to seek for the appropriate coupling coefficients that lead to stable in-phase locking. Then, we present a novel coupling architecture, the so-called “bridge coupled nanolasers”, which is an analogy of the “barrier engineering” in photonic crystals [57]. We then explore the performance of the fabricated devices using conventional laser characterization techniques and confirm their in-phase operation.

While nanolasers are shown to be promising light sources due to their energy-efficiency and fast-modulation potentials, certain performances require improvement before applying them in practical photonic systems. Compared to conventional semiconductor lasers, nanoscale lasers are also known for their broad linewidths, that are on the order of 1nm for various designs, including photonic crystals [10-15], SPASERs [16-21], coaxial [24], and metallo-dielectric nanolasers [25-33], etc. The linewidth of a light source arises from the phase noise, and is strongly related to the degree of coherence, i.e., coherence time and coherence length. For applications that require narrow linewidth, such as Lidar systems, coherent optical communications, and optical sensors, commercial DFB and DBR lasers are better candidates, as their linewidths can be as narrow as a few MHz or KHz. Further understanding in the origins of the broad linewidths of nanolasers will significantly help to engineer future devices that can be advantageous for the applications stated above. Therefore, Chapter 4 of this dissertation is dedicated to the theoretical investigation of the noise sources and their impact on the laser linewidth.

In Chapter 5, we will review some of the recent progress in the research of dual nanolasers and nanolaser arrays. Finally, in Chapter 6, we summarize the results presented in the thesis and discuss a few future directions for the nanolaser research.

Chapter 2 Stability of high-β coupled lasers

2.1 Introduction

Phase-locked laser arrays have been extensively investigated owing to their potential in generating high-power and coherent optical beams valuable for applications such as LiDAR, optical communications, and remote sensing [53, 55, 66]. Additionally, the ability to tune the phase difference between constituent elements in an on-chip semiconductor laser array is vital for beam forming and steering applications [69, 70]. To realize the desired phase offset of the lasers in the arrays, i.e. in-phase operation for high power emission and shifted phase operation for beam forming and scanning, establishing stable phase locking is imperative. However, such stability is challenging to achieve due to multiple factors such as mode competition, distinct time scales of photon and carrier dynamics, complex nonlinear dynamics over a wide range of physical parameters including inter-cavity distances and differences in resonator dimensions of coupled lasers, and most notably, due to the amplitude-phase coupling in semiconductor lasers quantified by the linewidth enhancement factor [71, 72]. Despite the challenges, stable in-phase locking has been demonstrated through spatial and spectral mode engineering, including evanescent coupling in topological cavities [73], non-Hermitian coupling in super-symmetry arrays [74], diffractive coupling via Talbot effect [68], global antenna coupling [67], and gain matching [75]. Achieving similar phase synchronization in laterally coupled lasers arranged in close proximity, although difficult, is highly desirable since it involves simpler fabrication procedures and offers denser on-chip integration compared to the other coupling schemes mentioned above. Moreover, the dynamical behavior of laterally coupled lasers can be accurately analyzed and predicted by non-complex mathematical models.

In fact, theoretical analysis of the stability in laterally coupled semiconductor lasers has been widely reported in the literature [59, 61-65]. In these studies, a plethora of dynamical regimes including stable continuous-wave operation, periodic and period-doubling oscillations, chaos, bistability, and chimera states are identified via bifurcation analysis. These dynamical behaviors are obtained by either analytically or numerically solving the coupled rate equations that govern the temporal dynamics of the emitted laser field. The impact of a variety of important parameters such as current injection rate, linewidth enhancement factor, laser size differences, as well as carrier and photon lifetimes, are addressed in these analyses. However, one critical parameter consistently overlooked in the majority of the theoretical works in the literature thus far is the spontaneous emission factor β. This β factor, defined as the fraction of spontaneous emission funneled into the lasing mode relative to all the other supported modes, is smaller than 10^{-3} in typical commercial laser diodes, and thus is reasonably neglected in most bifurcation studies [59, 63, 64]. Over the past two decades, however, nanolasers that exhibit intrinsically high and non-negligible β values have been demonstrated on various platforms [24, 35, 37, 76]. These nanoscale light sources offer unique advantages such as ultracompact footprints, low power consumption and high-speed modulation that make them ideal candidates for dense, on-chip integration [2, 41, 44, 77]. A handful of studies so far have reported on the significant impact that spontaneous emission can exert on coupling behavior such as mode switching for coupled photonic crystal nanolasers

[56, 68] and partial locking for mutually coupled micropillar lasers operating in the few-photon regime [78, 79]. Notably, some previous theoretical investigations have suggested that the larger damping effect induced by higher β may help suppress the instability encountered in lateral coupling schemes [62, 80]. This hypothesis as well as the rapid advances in nanolaser technology necessitate an in-depth analysis of how large values of β can contribute towards stable phase-locking operation.

2.2 Theoretical Model and Methods

The coupled rate equations, with β included, that govern the temporal dynamics of two laterally coupled laser cavities considered here are described in [56]:

$$\frac{d\left|E_{1,2}\right|}{d\tau}=\left(\mathit{\Gamma} G_N\left(N_{1,2}-N_0\right)-\frac{1}{\tau_p}\right)\frac{\left|E_{1,2}\right|}{2}+\frac{\mathit{\Gamma} F_p\beta N_{1,2}}{2\tau_{rad}\left|E_{1,2}\right|^2}\left|E_{1,2}\right| \mp\kappa\,sin(\mathit{\Delta\Phi})\left|E_{2,1}\right|+\gamma\,cos(\mathit{\Delta\Phi})\left|E_{2,1}\right| \tag{2.1a}$$

$$\frac{dN_{1,2}}{d\tau}=P_{1,2}-\frac{N_{1,2}}{\tau_{nr}}-\frac{\left(F_p\beta+1-\beta\right)N_{1,2}}{\tau_{rad}}-G_N\left(N_{1,2}-N_0\right)\left|E_{1,2}\right|^2 \tag{2.1b}$$

$$\frac{d\mathit{\Delta\Phi}}{d\tau}=\frac{\alpha}{2}\mathit{\Gamma} G_N(N_2-N_1)+\mathit{\Delta} w+\kappa\left(\frac{|E_1|}{|E_2|}-\frac{|E_2|}{|E_1|}\right)cos(\mathit{\Delta\Phi})-\gamma\left(\frac{|E_1|}{|E_2|}+\frac{|E_2|}{|E_1|}\right)sin(\mathit{\Delta\Phi}) \tag{2.1c}$$

where $\left|E_{1,2}\right|$ are the amplitudes of the electric fields in cavities 1 and 2, $\left|E_{1,2}\right|^2$ are the photon densities, $N_{1,2}$ are the carrier densities and $\mathit{\Delta\Phi}=\mathit{\Phi}_2-\mathit{\Phi}_1$ is the phase difference between the electric fields in the two cavities. The definitions of the other parameters and their representative values for an InGaAsP material system that is considered in the numerical simulations, are summarized in Table **2.1**. Practically, β cannot be varied solely without changing other parameters. Additionally, Purcell factor F_p and β are related and both are indeed functions of mode volume [76, 81, 82]. In theory, the laser rate equations can be simplified to consider mode volume as the only variable if one assumes a specific laser design where F_p and β depend solely on the mode volume. However, in this study, F_p and β are treated as independent from one another as well as the mode volume for the simplicity and intuitiveness of the analysis. Moreover, we are primarily interested in the universal trends of stability with respect to increasing values of β irrespective of different specific cavity designs. A deterministic model using an average β instead of a stochastic model considering random intensity noise in lasers is applied because the continuation analysis requires the system to start from a steady state [83]. The effect of noise on the phase-locking stability is discussed later.

Table 2.1 Laser parameters used for rate equation simulations.

Symbol	Definition	Value (Unit)
τ_p	Photon lifetime	1.5 (ps) [34, 39]
τ_{rad}	Radiative carrier lifetime	2 (ns) [26]
τ_{nr}	Nonradiative carrier lifetime	0.625 (ns) [26]
α	Henry factor	4 [34]
Γ	Confinement factor	0.8 [39]
N_0	Transparent carrier density	2×10^{24} (m^{-3}) [34]
F_p	Purcell factor	1
G_N	Differential gain	4.28×10^{-12} (m^{-3}) [26, 84]
$P_{1,2}$	Pump rate	10^{35} to $1.2 \times 10^{36} (m^{-3} \cdot s^{-1})$
Δw	Frequency detuning between two lasers $\Delta w = w_2 - w_1$	-2 to 2 (THz)

Finally, the coupling between the two cavities is introduced in a phenomenological manner via a complex coupling coefficient $i\kappa + \gamma$, that includes a dispersive coupling rate κ and a dissipative coupling rate γ. The parameters κ and γ originate from the dissimilarities in effective refractive indices and losses, respectively, between the two eigenmodes – bonding and anti-bonding - supported by the coupled cavities. To be more precise, κ can be calculated from the frequency splitting between the bonding and antibonding modes (denoted by + and -) using $\kappa = (w_+ - w_-)/2$, while γ can be calculated from the loss splitting as $\gamma = \left(\frac{w_-}{Q_-} - \frac{w_+}{Q_+}\right)/4$,where $Q_{+/-}$ are the quality factors of the supermodes [56]. To generalize the effects of increasing β for any laterally coupled system, the dependence of κ and γ on either coupling geometry or material properties is neglected, and their values are chosen to be within a range that can be feasibly achieved in coupled laser platforms [78, 80]. Although both the sign and the values of κ and γ can be precisely controlled through altering the coupling geometry and material composition [57, 85-87], such as changing the size of the nanoholes in the center barrier for coupled photonic crystal lasers, we first assume $\gamma = 0$ and $\kappa > 0$ for the simplicity of understanding the model and results presented here. Once we obtain enough initial insight into how stability depends on β and the other control parameters, we extend the study to consider a complex coupling coefficient with $\gamma \neq 0$ and the coupling rates demonstrating both positive and negative signs. This allows the model to reflect scenarios where either of the supermodes can exhibit higher eigenfrequency and/or higher losses. In other words, in addition to the coupling geometry and material composition, the sign and values of κ and γ also depend on the comparative values of the eigenfrequencies and losses of the two supermodes. It is worthy to mention that the mathematical model and bifurcation analysis used in this work can be applied to a wide range of laser platforms, including metal-clad lasers [37, 41, 44], plasmonic lasers [17], nanowire lasers [59], photonic crystal lasers [56] or even conventional semiconductor lasers with larger dimension. The lateral coupling can be achieved by evanescent waves, gain guiding, index guiding, or the combination of these methods [56, 59, 63, 64].

2.3 Phase-locking Stability V.S. $\boldsymbol{\beta}$

In this study, the stable phase locking regions for the two laterally coupled lasers are identified as functions of β, pump rate P and the frequency detuning Δw using the bifurcation software XPPAUT, which contains the numerical continuation package AUTO [83]. The electric fields and carrier densities in equation (2.1) are normalized to reduce the simulation time. The time scale of the rate equations is also normalized with respect to the photon lifetime τ_p (see Appendix A). Additionally, a small signal analysis is performed to provide physical insight into the results (see Appendix A for details). In this work, only three types of bifurcation points are discussed – pitchfork, saddle-node (SN) and Hopf bifurcations – since the stable regions are found to be exclusively bounded by these three types of bifurcations.

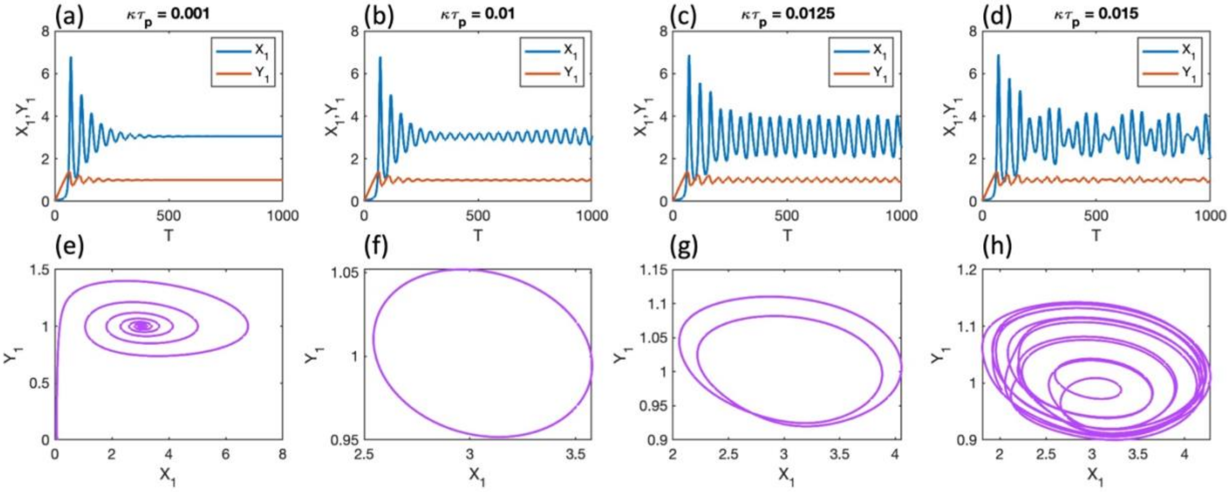

Figure 2.1 Temporal evolution (top row) and phase diagrams (bottom row) of normalized electric field amplitude X_1 and carrier density Y_1 as $\kappa\tau_p$ increases from 0.001 to 0.015 while keeping $\beta = 0.001$.

Figure **2.1** presents the evolution of the normalized electric field X_1 and normalized carrier density Y_1 as $\kappa\tau_p$ increases from 0.001 to 0.015 while keeping $\beta = 0.001$. The top figures show the temporal evolution, while the bottom figures show the phase diagram. Stable phase-locking, periodic oscillation, period doubling, and chaotic oscillations can be observed. It is important to note here that although the numerical continuation analysis of the coupled laser model reveals a plethora of dynamical regimes, we only consider the conditions that yield stable phase-locking. As a result, the latter three dynamical behaviors are categorized as unstable locking regimes for the purposes of this study.

2.3.1 Imaginary Coupling Coefficient

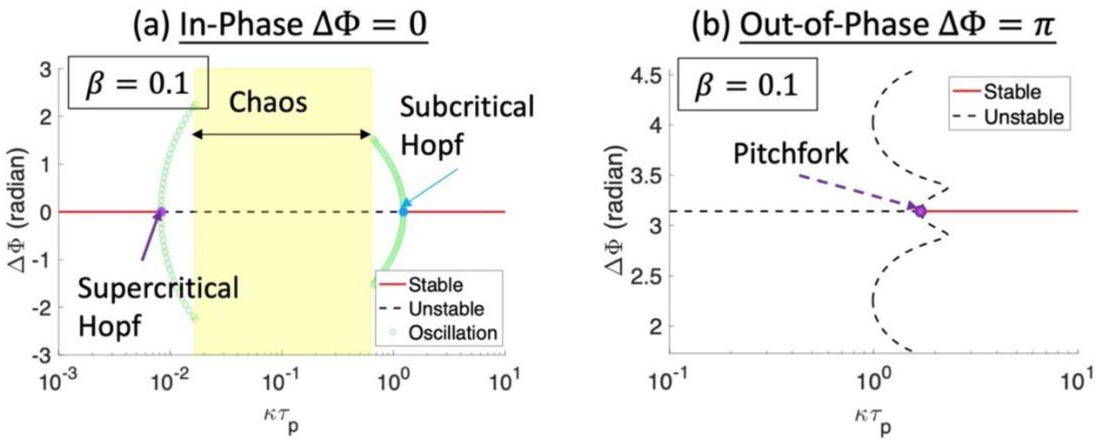

Figure 2.2 1-D bifurcation diagrams for (a) in-phase and (b) out-of-phase solutions, respectively. $\beta = 0.1, P_{1,2} = 1.2P_{th}$.

The simplest representation of the model assumes no frequency detuning, a constant pump rate and a purely imaginary coupling coefficient represented as $i\kappa\tau_p$, which is representative of the case when the two supermodes experience similar losses. Figure **2.2** (a) and (b) present the 1D bifurcation plots for in-phase $(\Delta\Phi = 0)$ and out-of-phase $(\Delta\Phi = \pi)$ solutions, respectively, when $\beta = 0.1$ and $P_{1,2} = 1.2P_{th}$. The variable P_{th} denotes the pump power at lasing threshold for a single laser and can be identified from the steady-state solutions of the rate equations when no coupling is considered. It can be seen for the in-phase solution that the system enters the periodic oscillation regime after the supercritical Hopf point and returns to steady state after the subcritical

Hopf point. For the out-of-phase solution, stability only exists at large coupling coefficient after a Pitchfork bifurcation point.

Figure **2.3** (a) and (b) illustrate the stability maps within the same parameter space for in-phase ($\Delta\Phi = 0$) and out-of-phase ($\Delta\Phi = \pi$) solutions, respectively, as a function of $\kappa\tau_p$ and β at a pump power of $P_{1,2} = 1.2P_{th}$. The solid purple and blue lines in Figure **2.3**(a) denote the Hopf bifurcation boundary and the dashed purple line in Figure **2.3**(b) represents the pitchfork bifurcation boundary. The Hopf boundary in Figure **2.3**(a) can be further demarcated into the supercritical Hopf (purple) and the subcritical Hopf (blue) branches. The regions colored in green, and orange denote the stable and unstable locking regimes, respectively, for both figures. The coexistence of in-phase and out-of-phase solutions for some values of $\kappa\tau_p$ and β can be explained by the fact that the two supermodes exhibit identical losses ($\gamma = 0$). A phenomenon common to both Figure **2.3**(a) and (b) is the expansion of the green stable regions as β is increased from 10^{-5} to its maximum possible value of 1. For the out-of-phase solutions depicted in Figure **2.3**(b), the slight increase in the area of the stable phase-locking region, located to the right of the plot at higher $\kappa\tau_p$ values, is easier to distinguish due to the solitary pitchfork boundary present in this graphic. In comparison, the supercritical and subcritical Hopf bifurcations for in-phase solutions in Figure **2.3**(a) dissect the parameter space into multiple sections. For $\beta \leq 10^{-2}$, only one stable region exists at very small coupling rates and it remains nearly unchanged in area as β increases from 10^{-5} to 10^{-2}, bounded by the supercritical Hopf bifurcation point. In comparison, for $\beta > 10^{-2}$, it can be observed that the stable locking region in the weak coupling regime significantly expands when β is increased due to the supercritical Hopf bifurcation point moving to much higher values of $\kappa\tau_p$. Moreover, as the coupling coefficient $\kappa\tau_p$ further increases, a second stable region appears after the subcritical Hopf point, seen towards the right side of Figure **2.3**(a). This second stability region has not been reported in literature till date, where mainly weak coupling $\kappa\tau_p \ll 1$ and negligible β are considered.

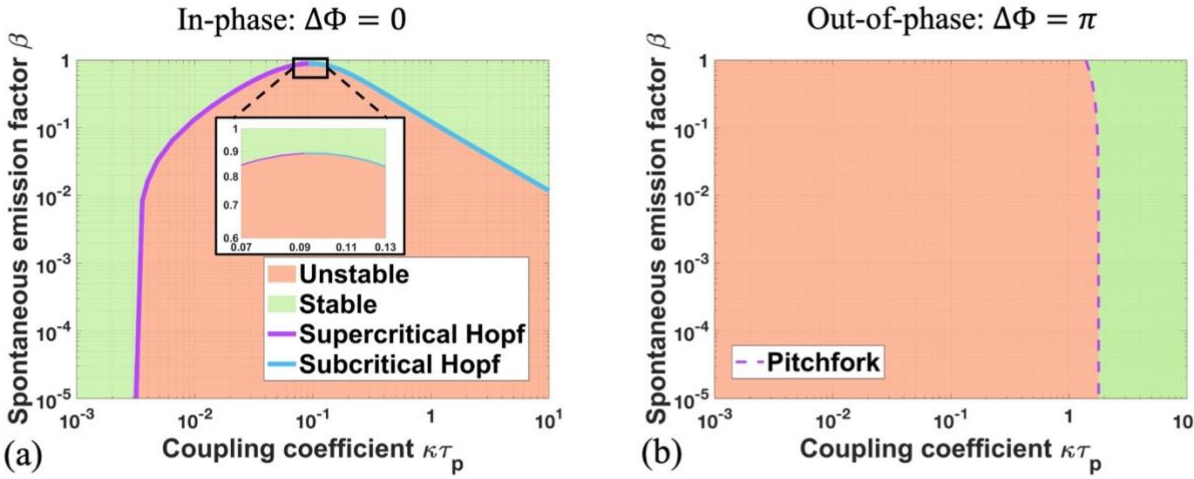

Figure 2.3 2-D bifurcation diagrams of the (a) in-phase solution and (b) out-of-phase solution in $(\kappa\tau_p, \beta)$ plane with $P_1 = P_2 = 1.2P_{th}$. Stable locking region is shown in green, unstable region in orange. Solid lines are the supercritical (purple) and subcritical (blue) Hopf bifurcation boundaries. Dashed line is the pitchfork bifurcation boundary.

Despite the complex demarcations in Figure **2.3**(a), it can be clearly observed that increasing β leads to a narrowing of the unstable region as the boundaries of the two Hopf bifurcations move towards each other. In fact, when $\beta = 0.89$, the two bifurcation branches become connected at $\kappa\tau_p \approx 0.09$ as shown in the inset of Figure **2.3**(a). For values of β beyond this point of confluence (i.e. $\beta > 0.89$), the steady-state solutions of the rate equations yield in-phase, stable solutions irrespective of the coupling strength. Intuitively, the positive effect of β on the phase-locking stability can be explained by the faster damping rate of high-β lasers and robustness of them to a perturbation involving photon fluctuations [40] (also see Appendix A). This result holds major significance as it suggests that nanolasers with β values approaching 1 are ideal candidates to be used in phase-locking arrays to generate high power far-field emission.

2.3.2 Pump Rate

In the previous section, the pump rate was fixed at a constant value for both lasers. In order to gauge whether increasing β leads to a similar expansion in the stability regions for any arbitrary pump rate, 3-dimensional (3-D) stability plots with varying P/P_{th} ($P_1 = P_2 = P$) being the third dimension, are created for the in-phase and out-of-phase solutions as shown in Figure **2.4**(a) and (b), respectively. The stable regions are denoted in white while the unstable ones are shaded in grey in these figures. For the in-phase solutions depicted in Figure **2.4**(a), when $\beta \leq 0.01$, the supercritical bifurcation branch (surface on the left) moves towards larger $\kappa\tau_p$ as the pump rate P/P_{th} increases, thereby enhancing the stability. This trend has also been reported in another study that focused exclusively on weak coupling and did not consider the effect of the β factor [63]. For $\beta \geq 0.01$, however, increasing the pump rate can cause the supercritical bifurcation to shift to smaller $\kappa\tau_p$, and thus shrink the stable locking region. This stability reduction as pump rate increases can be explained by the small signal analysis detailed in the Appendix A. Essentially, for weak coupling, the damping rate of the small perturbations can be mathematically approximated to be that of the relaxation oscillations, with this rate increasing for small β and decreasing for large β as pump rate increases. Therefore, as the pump rate is increased for large β, the lower damping rate means that the system is now more susceptible to small perturbations and hence, exhibits less stability. Similarly, for the subcritical bifurcation branch (right side of the surface in Figure **2.4**(a)), an increasing pump rate P/P_{th} pushes the branch to larger coupling coefficients, which also leads to narrowing of the stable locking region. Despite these seemingly disparate effects of the pump on stability, however, the most important observation from Figure **2.4**(a) is that the two Hopf bifurcation branches always move towards each other as β increases. The increasing proximity of the two bifurcations in turn, results in an expansion of the stability region. Therefore, it can be concluded that although varying the pump rate affects the stability in a non-uniform manner, higher β values always contribute towards increased in-phase locking irrespective of the pump rate.

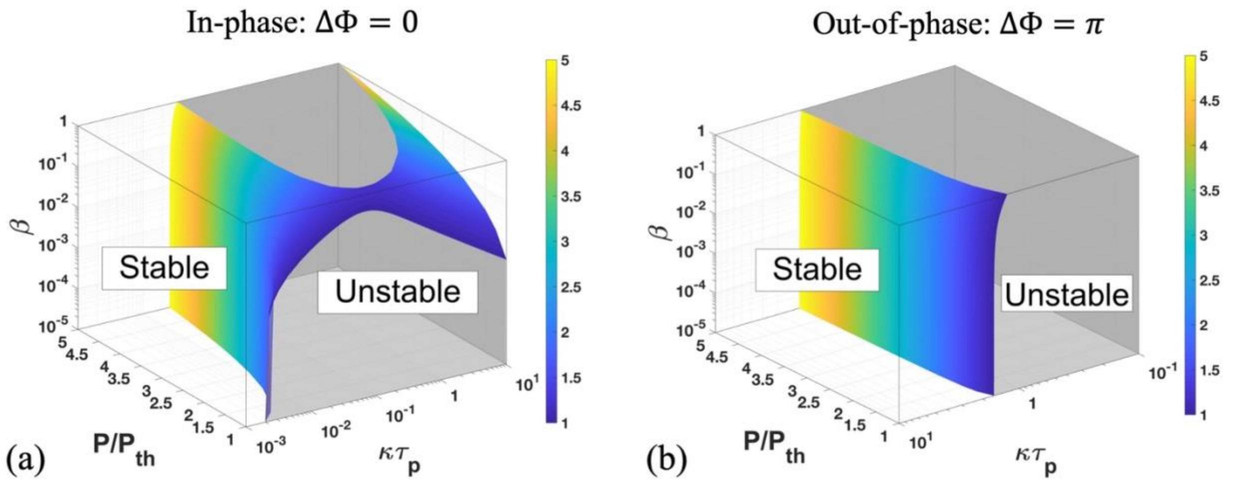

Figure 2.4 3-D bifurcation diagrams with varying pump rate. (a) 3-dimensional stability plot in the $(\kappa\tau_p, P\ /\ P_{th}\ , \beta)$ plane for in-phase solutions. The 3-D surface is the Hopf bifurcation stability boundary. The color denotes various pump rate as shown in the colorbar. Stable phase locking region is shown in white, and the unstable region in grey. (b) 3-D stability plot in the $(\kappa\tau_p, P/P_{th}\ , \beta)$ plane for out-of-phase solutions using same color convention as in (a). The surface now represents the pitchfork bifurcation stability boundary.

In contrast, for the out-of-phase solutions depicted in Figure **2.4**(b), the pitchfork bifurcation boundary remains almost unaltered despite varying both P/P_{th} and β. The reason for this can be inferred from small signal analysis (see Appendix A), which reveals that the pitchfork boundary is approximately proportional to $N_{1,2} - N_0$. Given that $N_{1,2}$ clamps to a threshold value as P/P_{th} increases, the stability boundary therefore stays almost constant. Though higher β values result in a slight increase of $N_{1,2}$, the consequent expansion of the stability region is miniscule. Fortuitously, for most applications, only the in-phase solutions are of interest as they are essential for the generation of higher power density. Therefore, in the next section when we consider frequency detuning, we focus exclusively on the solutions around $\Delta\Phi = 0$, which are referred to as “in-phase solutions” for simplicity.

2.3.3 Frequency Detuning

Now we consider the case where two cavities exhibit disparate resonance frequencies and investigate whether a stability enhancement from high-β can be observed in this scenario. While frequency detuning is usually induced by dissimilarities in the dimensions of the resonators caused by fabrication imperfections, it can also be intentionally introduced into the coupled structure for certain applications. For example, phase-locked laser arrays with shifted frequencies between the adjacent elements can be implemented in ultra-high-resolution lidar systems for distance-angle beam steering tasks [88-90].

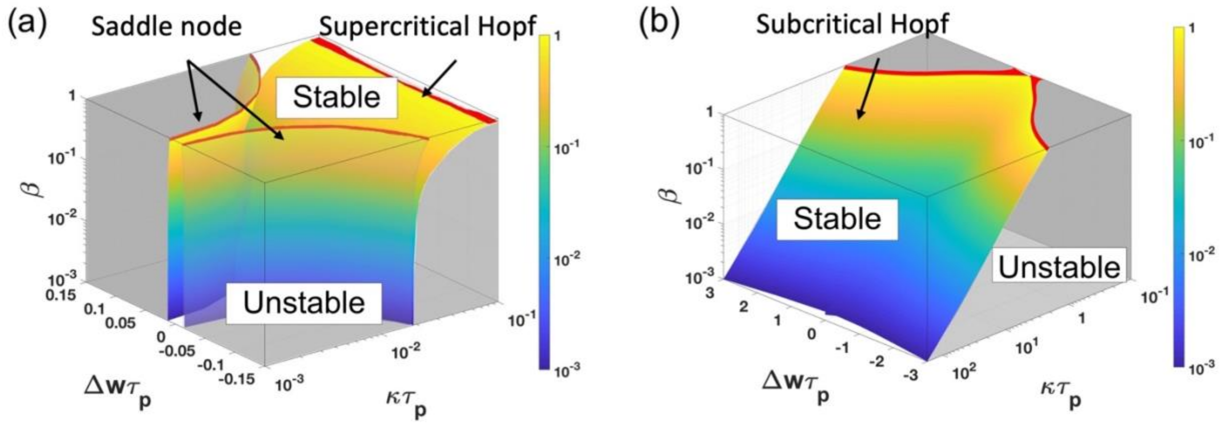

Figure 2.5 3-D bifurcation diagrams with varying detuning. (a) 3-D stability plot in the $(\kappa\tau_p, \Delta w\tau_p, \beta)$ plane for in-phase solutions with $\kappa\tau_p \in [10^{-3}, 10^{-1}]$. The 3-D surfaces are the stability boundaries for Hopf and SN bifurcations. The colors denote varying β as shown in the colorbar. The red region denotes $\beta \geq 0.89$. Stable phase locking region is shown in white, and the unstable region is colored in grey. (b) 3-D stability plot in the $(\kappa\tau_p, \Delta w\tau_p, \beta)$ plane for in-phase solutions with $\kappa\tau_p \in [10^{-1}, 200]$ using the identical color convention as in (a).

In Figure **2.5**, the stable regions of the in-phase solutions are depicted in a 3-D parameter space $(\kappa\tau_p, \Delta w\tau_p, \beta)$ with $P/P_{th} = 1.2$. To provide a more intuitive visualization, the parameter space is dissected into two regions at $\kappa\tau_p = 0.1$, which is the approximate point of confluence where the supercritical and subcritical Hopf branches become connected, as shown in the zoomed-in inset of Figure **2.3**(a). Consequentially, Figure **2.5**(a) represents the region of $\beta \leq 0.1$ containing the supercritical Hopf bifurcation while Figure **2.5** (b) illustrates the scenario when $\kappa\tau_p \geq 0.1$ and the subcritical Hopf branch is observed. Like in Figure **2.4** the stable and unstable regions are represented in white and grey, respectively, in Figure **2.5**(a) and (b) as well.

Detuning the frequency gives rise to two symmetric SN bifurcation boundaries for the case of weak coupling ($\kappa\tau_p \leq 0.1$) depicted in Figure **2.5**(a). These SN bifurcation surfaces, along with the supercritical Hopf boundary, enclose the stable in-phase locking region. As detuning is decreased, the SN boundaries move closer to one another but remain unconnected for the case of zero detuning resulting in only Hopf bifurcation boundaries that are observed in this case. More importantly, as β increases, although the SN boundaries remain largely unperturbed, the supercritical Hopf branch relocates to higher $\kappa\tau_p$values. This, in turn, expands the stable phase locking region in Figure **2.5**(a). Similarly, for $\kappa\tau_p \geq 0.1$ in Figure **2.5**(b), the stable phase locking region is also seen to expand for higher β values when the subcritical Hopf bifurcation serving as its sole boundary shifts towards smaller $\kappa\tau_p$. It is important to note here that the subcritical Hopf points for ultra-small β (the bluer-parts of the 3-D surface in Figure **2.5**(b)) require extremely high values of $\kappa\tau_p$ ($\kappa\tau_p > 10$) which are not realistically achievable in experiment. This explains why the second stability region shown in Figure **2.5**(b) has not been previously reported in the literature where usually, only weak coupling and negligible β are considered. The results here indicate that increasing β helps expand the stable, in-phase locking regions for both weak and strong coupling cases despite the lasers demonstrating dissimilar frequencies.

In Figure **2.3**(a), it was seen that when $\beta \geq 0.89$, stability holds irrespective of the strength of coupling for the $\Delta w = 0$ case. However, the same does not hold true when the frequency detuning between the two lasers is non-zero. For $\beta \geq 0.89$, with non-zero detuning, the stability boundaries are colored in red as shown in Figure **2.5**(a) and (b) and indicate that the stability is lost when detuning is non-negligible. To better illustrate the in-phase stability map with frequency detuning in the low, moderate and high β regimes, we combine the parameter spaces shown in Figure **2.5**(a) and (b) and present them in Figure **2.6** as 2-D parameter projections at $\beta = 10^{-3}, 0.25,$ and approaching 1. The stable regions are now denoted in green while their unstable counterparts are colored in orange. Considering first the case of $\beta = 10^{-3}$ in Figure **2.6**(a), the stable solutions can be seen to be enclosed in an extremely narrow parameter space by the SN (dashed purple lines) and supercritical Hopf (solid purple line) bifurcations. As β is increased to 0.25 in Figure **2.6**(b), the stable region expands to cover a much larger area while a second stable region is created at high $\kappa\tau_p$ values due to the presence of the subcritical Hopf boundary (solid blue line). Finally, as β is increased beyond 0.89 in Figure **2.6**(c), the supercritical and subcritical Hopf boundaries merge, resulting in stable in-phase locking regions that span a significantly larger range of both $\kappa\tau_p$ and $\Delta w\tau_p$values. Akin to what was observed when varying the pump rate, the desirable result of high- β increasing the stability of two laterally coupled lasers is preserved even when frequency detuning is considered.

It is worth mentioning here that the enhancement of stability due to large β for the non-zero frequency detuning case is not restricted only to the pump rate assumed in the above results. Though they have not been included in this work, additional simulations show that increasing or decreasing the pump rate around $P/P_{th} = 1.2$ will only slightly modify the quantitative value of the bifurcation points while the main features of the stability plots remain unaltered. Specifically, increasing the pump rate provides increased stability for coupled lasers with small β and a reduction in the stable region for coupled lasers with high β, as observed in Figure **2.4**(a). More importantly, it is observed that for any given pump rate, systems with higher β always demonstrate a larger stable phase locking region over the parameter space $(\kappa\tau_p, \Delta w\tau_p)$, i.e. better stability. Another reason for choosing the pump rate of $P/P_{th} = 1.2$ for the above simulations is that in practice, lasers operating lightly above threshold have the highest energy transfer efficiency, i.e. wall plug efficiency (WPE) [91], and can also be prevented from overheating due to large current injection. Since nanolasers with high β exhibit a low pumping threshold [40], it is not only energy efficient to operate slightly above threshold, but stable phase locking is also most achievable with a high β value and low pump rate.

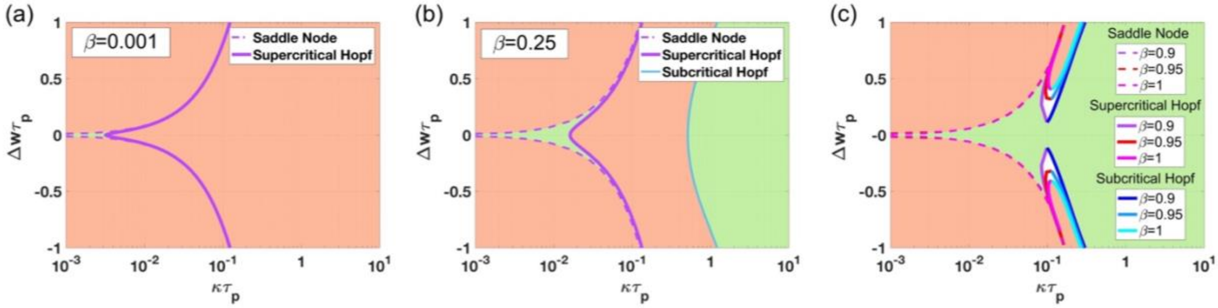

Figure 2.6 2-parameter bifurcation diagrams with varying detuning. Stability of the in-phase solutions in the $(\kappa\tau_p, \Delta w\tau_p)$ plane with $P_1 = P_2 = 1.2P_{th}$ for (a) $\beta = 10^{-3}$, (b) $\beta = 0.25$, and (c) $\beta \geq 0.9$. Stable locking regions are colored in green, unstable regions in orange. Solid lines represent the supercritical (purple, red, magenta) and subcritical (blue, light blue, cyan) Hopf bifurcation boundaries. Dashed lines denote the SN bifurcation points.

2.3.4 Complex coupling coefficients

To further extend the analysis to account for the scenarios where the supermodes exhibit dissimilar losses, a complex coupling coefficient $i\kappa + \gamma$- where κ and γ can be either positive or negative - is used to replace the purely imaginary coupling coefficient used thus far in the model. This modification is especially important if considering coupling geometries employing gain-guiding and carrier-induced index antiguiding [63], where either of the supermodes can exhibit higher eigenfrequencies and/or higher losses. In order to simplify the ensuing bifurcation analysis, the coupling amplitude $|\boldsymbol{\kappa}|$ and phase $\theta_{\boldsymbol{\kappa}}$ are used instead of κ and γ to provide better intuition for the control parameters used, i.e. $i|\boldsymbol{\kappa}|e^{j\theta_{\kappa}} = i\kappa + \gamma$, $\kappa = |\boldsymbol{\kappa}|cos\theta_{\boldsymbol{\kappa}}$, and $\gamma = -|\boldsymbol{\kappa}|sin\theta_{\boldsymbol{\kappa}}$, where $\theta_{\boldsymbol{\kappa}} \in [-\pi, \pi]$. Furthermore, the pump rates are assumed to be $P/P_{th} = 1.2$ to obtain a high energy efficiency in practice. Altering the pump rate around this value does not significantly impact the general shape of the stability regions and only negligibly shifts the boundaries. Therefore, the variation of the stable phase locking regions due to β is unlikely to be affected by the choice of the pump rate level. Finally, the frequency detuning is assumed to be 0 initially for simplicity, with a more detailed analysis on non-zero detuning discussed briefly towards the end of this section.

The stability plots, when considering the complex coupling coefficient and varying $\beta = 10^{-3}, 0.05, 0.25,$ and 1 are superimposed and presented in Figure **2.7**(a). Although the bifurcation analysis yields a plethora of bifurcation boundaries, in Figure **2.7**(a), we only show those that directly demarcate the stable and unstable regions, i.e., Hopf points (solid lines) and the pitchfork points (dashed lines). In Figure **2.7**(a), the regions in red represent stable in-phase solutions, the ones colored in blue denote stable out-of-phase solutions and the white, unshaded regions represent unstable solutions. From this figure, it can be observed that the stability regions of in-phase (red) and out-of-phase solutions (blue) with the same β values are identical in shape albeit shifted with respect to each other by π radians. The reason for this horizontal shift, which can be easily deduced from the rate equations (Appendix A equation (A.1)), is that if γ flips its sign, i.e. $\theta_{\boldsymbol{\kappa}}$ becomes $\theta_{\boldsymbol{\kappa}} + \pi$, then $\Delta\Phi$ is shifted by π radians. This underlines the significance that the signs of κ and γ hold and how controlling them would allow a coupled system to achieve the desired phase difference as predicted by the rate equations. However, the even more significant finding from Figure **2.7**(a) is that as β increases, both the in-phase and out-of-phase solutions expand in size, which is consistent with what was observed in Figure **2.3**(a) and (b). We would like to note that not all coupling values illustrated in Figure **2.7**(a) are realistically achievable in experiment. For instance, for coupled systems with $Q_{+/-}$on the order of hundreds of more, γ cannot be on the same order as κ and therefore $\boldsymbol{\theta_\kappa}$ values around $\pm\frac{\pi}{2}$ cannot be realized from the definition of the coupling coefficient provided in Chapter 2.2. Nevertheless, the purpose of choosing this wide range of complex coupling coefficients is to provide an accurate picture of how the stability regions expand as β is increased. Moreover, a large span of coupling coefficients have been demonstrated in common laser platforms. For example, evanescently coupled metallo-dielectric nanolasers have been reported to exhibit frequency and loss splitting that leads to $\kappa\tau_p$ from 4.16 to 0.04 and $\theta_\kappa \approx -\pi$ when the distance between two nanolasers ranges from 0nm to 90nm, respectively [39]. Using the same coupling mechanism in photonic crystal nanolasers, $|\kappa\tau_p| \approx 1.88$ and $\theta_\kappa \approx 0.01\pi$ are achieved, and the coupling coefficients can further be modulated by controlling the size and number of air holes in the coupling region [56]. Therefore, even though not all the coupling parameters in the $(\theta_\kappa, |\kappa\tau_p|)$ plane in Figure **2.7** are realistic, a wide range of coupling coefficients can be achieved by typical coupled-laser designs, which justifies the choice of the range of $(\theta_\kappa, |\kappa\tau_p|)$ in our simulation.

Another interesting observation is the coexistence of in-phase and out-of-phase solutions in certain parts of the $(\theta_\kappa, |\kappa\tau_p|)$ parameter space, specifically around $\theta_\kappa = 0$ (and $\theta_\kappa = \pi$). Recall that around these values, the supermodes have nearly identical losses and therefore exhibit approximately equal probability of being supported by the coupled system. The same coexistence of solutions was also observed in Figure **2.3**(a) and (b), since the purely imaginary and positive coupling coefficient used in the analysis in that section can be viewed as a special case of $\theta_\kappa = 0$. The evolution of these bistable regions as β is varied is plotted in Figure **2.7**(b)-(e). It can be clearly observed that in addition to expanding stable regions, increasing β can also lead to a larger overlap of the in-phase and out-of-phase stable solutions, thereby increasing the likelihood of achieving bistability. Within these bistable regions, the final steady state depends on the initial state of the phase relations between the two solutions. Such bistable operation poses great potential for use as memories such as for optical flip-flops [56, 92] as well as for optical analogues of the degenerated spins in an Ising machine [93].

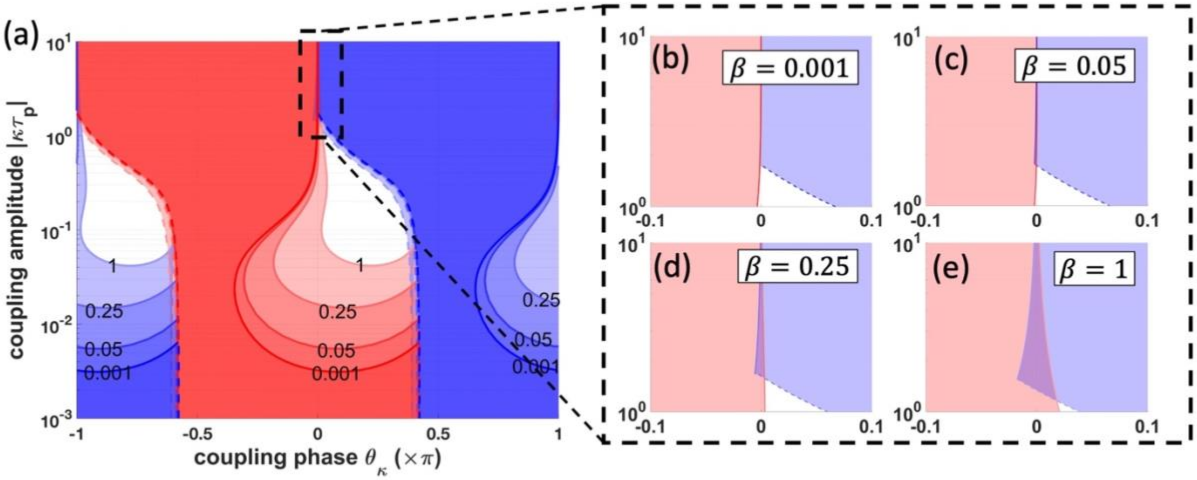

Figure 2.7 Bifurcation diagrams with complex coupling coefficients. (a) 2-parameter bifurcation diagrams of in-phase and out-of-phase solutions in the $(\theta_\kappa, |\kappa\tau_p\ |)$ plane with $\beta = 10^{-3}$, 0.05,0.25 and 1. The stable in-phase locking region is shown in red; the stable in-phase locking region is shown in red; the stable out-of-phase locking region is colored in blue, and the unstable region is shown in white. The solid lines denote Hopf bifurcations, while the dashed lines denote Pitchfork bifurcations. (b) – (e) Zoom-in of the region $\theta_{\boldsymbol{\kappa}} \in [-0.1\pi, 0.1\pi], |\boldsymbol{\kappa}\tau_p| \in [1,10]$ for $\beta = 0.001, 0.05, 0.25, 1$, respectively.

When non-zero frequency detuning is considered along with the complex coupling coefficient, it is observed that both the in-phase and out-of-phase stable regions have a lower bound in $|\kappa\tau_p|$, which is due to the SN boundary arising from the non-zero Δw. As Δw increases, both the SN and Hopf bifurcation points are shifted in a manner that reduces the stable phase locking region in the parameter space $(\theta_\kappa, |\kappa\tau_p|)$. However, for any non-zero Δw, an enhanced stability from higher β can always be observed, which is consistent with the results from previous sections. Though discussed briefly here, the detailed results are not included in this work for brevity.

In summary, with regards to stable phase-locking, increasing β unequivocally leads to an expansion in the stability regions despite considering varying pump rates, detuned frequencies and both imaginary and complex coupling coefficients. The robustness of the desirable effects of high β on stability truly emphasize the tantalizing potential of nanolaser arrays to harness this advantage and help in the generation of high optical power via in-phase locking. Additionally, high-β nanolaser arrays can also aid in the development of next generation active optical phased arrays as discussed in the next section.

2.4 Phase Difference Modulation V.S. β

In the previous section, the stability of phase locking was studied as functions of $\beta, P, \Delta w$, and θ_κ. The results were focused on the in-phase ($\Delta\Phi = 0$) and out-of-phase ($\Delta\Phi = \pi$) solutions for their potential in high-power beam generation and optical memory. In some other applications such as beam steering for Lidar and imaging systems, a tunable phase offset between adjacent lasers is required. In fact, having a wide range of tunable phase differences between coupled lasers can prove essential in these applications, since this attribute can help increase the azimuthal and vertical scanning ranges. Using lasers as array elements instead of passive phase shifters injected by a single laser source offers the advantage of both frequency and phase reconfiguration, which are essential for complex detection and sensing applications [88, 89]. In this section, we theoretically propose and analyze a method to modulate the phase difference between two coupled lasers. For a symmetrically coupled system like we have considered thus far, i.e. equal pumping rate $P_1 = P_2$, the case of zero-frequency detuning $\Delta w = 0$ yields only two possible solutions for the steady-state phase difference $\Delta\Phi$: the in-phase ($\Delta\Phi = 0$) and the out-of-phase solutions ($\Delta\Phi = \pi$). If the symmetry between the two lasers is broken by pumping the cavities at dissimilar rates, then values of $\Delta\Phi$ that are neither 0 nor π are achievable. In fact, $\Delta\Phi$ can then be tuned within the stable phase-locking range according to the ratio of the pump rates for the two lasers.

To identify the feasibility of nanolasers to be implemented in novel phased arrays for beam steering, the dependence of the phase difference tunability on β is investigated. In the simulation for each β value, the pump rate for one of the lasers, P_1, is fixed while the pump rate for its neighbor, P_2, is varied. We choose to keep $P_1/P_{th} = 1.2$ for the same reason of energy efficiency that was mentioned in the previous sections. To realize phase difference modulation, P_2 needs to be varied within a range where only stable phase locking is supported by the coupled cavities. Additionally, P_2 needs to be experimentally achievable and is thus varied only from P_{th} to $12P_{th}$ throughout this simulation. The three sequential steps followed to perform the analysis are as follows: First, by keeping β and P_1 constant, a one-parameter bifurcation analysis by varying P_2 is conducted, and the maximum and minimum possible $\Delta\Phi$ within the stable region are recorded. Secondly, the above step is repeated for β's ranging from 10^{-5} to 1, and the maximum and minimum $\Delta\Phi$ that can be achieved by varying P_2 are recorded for each β value. Finally, these results are depicted in Figure **2.8**(a) where the maximum and minimum $\Delta\Phi$ values are plotted as a function of β, as well as in Figure **2.8** (b) where the phase tuning range representing the differences between the maximum and minimum $\Delta\Phi$ is also shown as a function of β. For these simulations, the frequency detuning between the two lasers is neglected, and γ is assumed to be 0 for simplicity. Additionally, only an imaginary and constant coupling rate of $\kappa\tau_p = 10^{-3}$ is considered. It is important to note here that phase tunability was only observed with a coupling rate within the first stability region (to the left of the supercritical Hopf bifurcation boundary in Figure **2.3**(a)) and not for $\kappa\tau_p$ values in the second stability region (to the right of the subcritical Hopf boundary in Figure

2.3(a)). Moreover, within the first stability region, varying $\kappa\tau_p$ affects the values of $\Delta\Phi$ only in a negligible manner.

As can be clearly observed in Figure **2.8**(a) and (b), as β is increased, a wider range of tuning in $\Delta\Phi$ is afforded. Specifically, in the yellow region demarcated by extremely low-β (10^{-5} to 10^{-3}), the maximum and minimum $\Delta\Phi$ achievable are around -0.05π and 0.05π, respectively. As β is increased to values in the blue region, the range for $\Delta\Phi$ expands significantly to about $[-\pi/2\ ,\pi/2]$. Therefore, the phase tuning range shown in Figure **2.8**(b) increases from around 0.1π to π as β increases from that of conventional semiconductor lasers, i.e. $\beta \leq 10^{-3}$, to that of microscale and nanoscale lasers, i.e. $\beta > 0.01$. The reason for this wider range of phase tunability brought about by increasing β lies in the manner in which bifurcation points alter the stable solutions. For the range of extremely low- β values shaded as the yellow region in Figure **2.8**(a), the coupled lasers remain stable for all values of $P_2/P_{th} \in [1{,}12]$ as shown in Figure **2.8**(c). However, when β is increased to values in the pink region of Figure **2.8**(a), an SN bifurcation point arises that pushes the lower limit of $\Delta\Phi$ closer to $-\pi/2$. This result is encapsulated in Figure **2.8**(d) for a specific value of $\beta = 0.0175$ that lies within the pink region in Figure **2.8**(a). Finally, for high- β values in the blue region of Figure **2.8**(a), two SN bifurcation points further define the stability boundary such that $\Delta\Phi$ can now vary from $-\pi/2$ to $\pi/2$ when P_2/P_{th} varies within a small range around 1.2, as illustrated in Figure **2.8**(e) for $\beta = 0.1$. Therefore, increasing β can significantly increase the range of phase differences possible for stable phase-locked solutions, highlighting the fact that laterally coupled nanolasers with intrinsically high β values can prove valuable in realizing wide scanning angles in optical phased arrays.

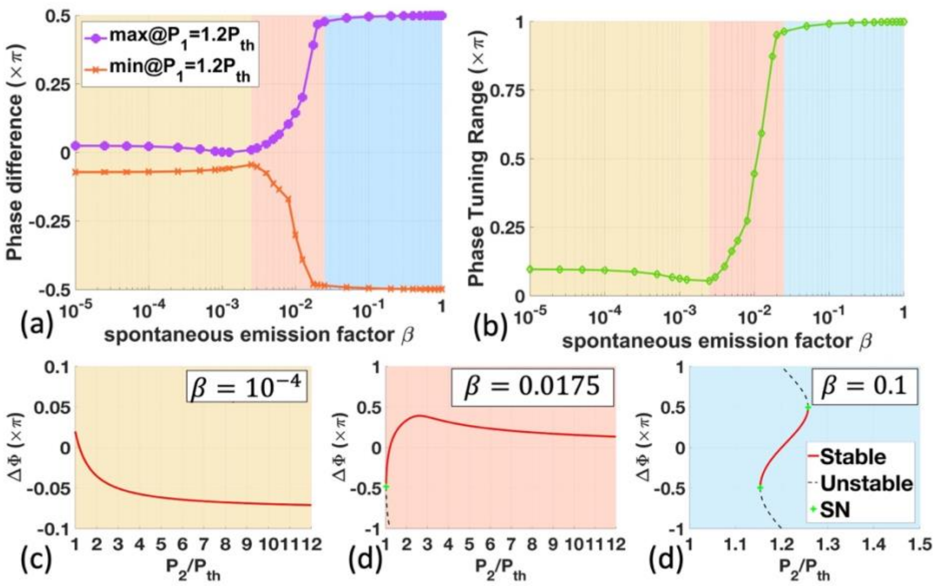

Figure 2.8 (a) Maximum (purple) and minimum (orange) phase differences achieved by varying the pump rate P_2 while keeping P_1 constant, plotted as a function of β. For each β value, the maximum values are marked with circles, and the minimum values are marked with asterisks. P_1 is set to be $1.2P_{th}$. (b) Phase difference tuning range as a function of β. The colored regions in both (a) and (b) represent the number of bifurcation points observed in the solutions. This is better illustrated in (c)-(e) which show the steady-state phase differences for three different values of β- 10^{-4}, 0.0175, and 0.1. Depending on the value of β, there may exist zero (c), one (d) or two (e) SN bifurcations points in the solution, corresponding to the yellow, pink and blue regions in (a), respectively.

2.5 Stability analysis of triple and quadruple lasers

Having analyzed the beneficial effects of β on the stability of two laterally coupled lasers, it is now important to extend these ideas to arrays larger than two. Ultimately, the goal is to identify an array topology that is most suitable to function as a unit cell that can be used to extrapolate the probable behavior of much larger scale arrays. Therefore, we have theoretically studied the stable in-phase locking regime of coupled nanolaser arrays consisting of 3-4 elements as a function of multiple parameters unique to nanolasers, including the spontaneous emission factor β, as well as other parameters such as the coupling strength, κ and the pumping rate P. In the following sub-sections, we present some of our initial results on solving the coupled rate equations for different array topology designs of 3 and 4 nanolasers while varying some key parameters.

In order to design laterally coupled nanolasers to achieve high-power, it is imperative to first assess the optimal manner in which to arrange the individual elements. For an array of just two nanolasers as was considered in the previous section, the only possible arrangement is in a line. However, for lattices greater than two, the choice of the laser placement can alter the rate equations describing the system and consequently the stability regions. Our preliminary work involving three nanolasers suggests that arranging them in a triangle pattern where each source is coupled to its two neighbors yields an increased stability region (Figure **2.9**(a)) than when the nanolasers are arranged in a straight line with each source only coupled to its nearest neighbor (Figure **2.9**(b)). For both arrangements, however, increasing β leads to an expansion of the "green" stability regions as was the case for just two nanolasers (see Figure **2.3**(a)) further emphasizing the scalability and immense potential of using high-β lasers for phase-locked arrays.

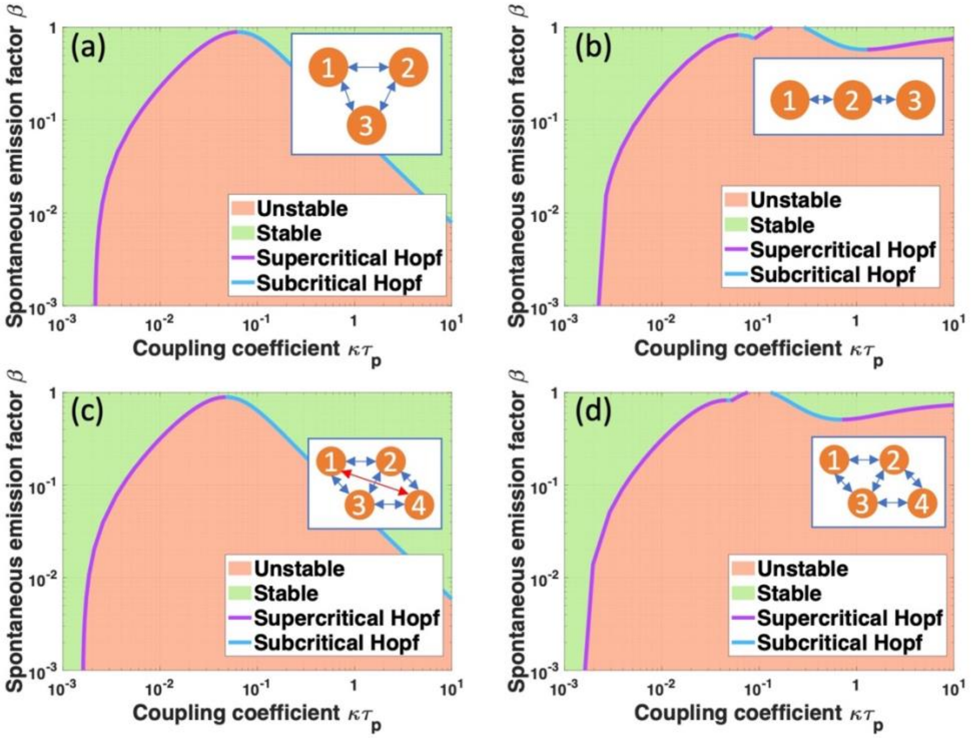

Figure 2.9 Stability maps as a function of coupling coefficient $\kappa\tau_p$ and spontaneous emission factor β for triple and quadruple lasers. Triple lasers arranged in (a) a triangle and (b) a line. Quadruple lasers arranged in (c) fully connected network and (d) nearest-neighbor coupling network.

Thus far, we have also considered the stability of four coupled lasers by adding the fourth element next to a triangle unit cell and consider two scenarios for coupling relationships shown in the insets of Figure **2.9**(c) and (d). In Figure **2.9**(c), all the four lasers are coupled to all the other three elements. The coupling between elements 1 and 4 can be achieved in practice by adding a bridge in between or a waveguide to introduce the optical coupling. In comparison, in Figure **2.9**(d), the four lasers are only coupled to their nearest neighbor such that 1 and 4 are not coupled.

From Figure **2.9**(c), it can be postulated that the stability of four coupled lasers in a fully connected network, i.e., laser 1 and 4 are coupled, follows that of three lasers coupled in a triangle. If there is no coupling between laser 1 and 4 as shown in Figure **2.9**(d), then it can be observed that the stability follows that of triplets coupled in a straight line. The existence of the coupling between 1 and 4 significantly alters the stability of the laser array. For the more feasible platform, i.e., nearest-neighbor coupling, not all the array elements are in-phase. Specifically, 2 and 3 as well as 1 and 4 are in-phase locked, while the phase differences between 1 and 2 as well as 1 and 3 are non-zero, in fact, have the same value but opposite sign. This phenomenon of clustered synchronization has been reported in coupled fiber lasers [94, 95], where a laser array forms two clusters and the lasers in only one of clusters are in-phase locked. In this case, our results indicate that a certain level of phase-locking (which can be inferred by the visibility of the interference fringes for instance), despite the absence of perfect phase-locking, can be achieved in practical arrays and still significantly increase the output power. Therefore, exploring the dependence of the phase-locking solutions and stability on the architecture of the laser array, including how the lasers are arranged and how many neighbors each laser is coupled to, can yield important results that can prove crucial towards scaling up the array sizes. The salient question that needs to be answered is - if the laser array is also formed into clusters, then what is the level of phase-locking that can be achieved? Additionally, is it possible that only the elements on the edges are not phase-locked with the ones in the center, while all the other elements are still in-phase? If that is the case, then the output power of an $N * N$ laser array will be $N^2 - 4N$ and can be approximated to N^2 as N is increased to sufficiently large values. This hypothesis is based on our preliminary results where lattices that are fully connected (each laser element is coupled to every other element in the array) seem to exhibit in-phase locking for all elements regardless of size (Figure **2.9**(a) and (c)). In contrast, in non-fully connected lattices, some of the edge elements that are not coupled to every element in the array appear slightly out-of-phase (Figure **2.9**(b) and (d)).

An important feature that must be reiterated is that under all scenarios, an increased β always leads to enhanced stability, even for the preliminary analyses of 3 and 4-element arrays. Additionally, for high β values approaching 1, the stability of such laser arrays is not even affected by the architecture of the laser array. Therefore, employing nanolasers with intrinsic high β is of vital importance to build a robust and ultra-dense laser array.

2.6 Discussion

In the previous analysis, the noise contribution from the intrinsic intensity fluctuation and spontaneous emission is neglected. Such random noise can be mathematically accounted for by introducing Langevin noise into the stochastic rate equations [56], which cannot be analyzed by the bifurcation analysis software [83]. However, we will discuss qualitatively how intensity fluctuations can affect the results presented earlier. The intensity noise introduces instant asymmetry in photon numbers in two coupled cavities and causes the phase difference to deviate from $\Delta\Phi = 0$ or π depending on the difference in the photon numbers ΔN_{ph} compared to the mean value $\overline{N_{ph}}$, i.e., $\Delta n_{ph} = \Delta N_{ph}/\overline{N_{ph}}$. While the instantaneous Δn_{ph} is small, the coupled system will have a quasi-phase-locking state with $\Delta\Phi$ close to 0 or π. However, when Δn_{ph} is very large, phase-locking in two distinct cavities cannot be achieved, and the system can be driven by the intensity noise into unstable regime until a noise event with small Δn_{ph} pulls the system back into the stable regime. Therefore, coupled lasers with large signal to noise ratio (SNR) is more robust to intensity fluctuation as the noise contribution can be safely neglected. For example, the average photon number in an experimentally demonstrated metallo-dielectric nanolaser with a radius of 350nm and $\beta = 0.25$ [37] is estimated to be 1090 when the pump power is around two times the threshold [91]. This corresponds to around 3.4×10^5 photons in a pulse considering a pulse width of 11ns and repetition rate of 290KHz. Using such type of high-β lasers in the coupled system, we can assume that quasi-in-phase or out-of-phase locking can be achieved even when intensity fluctuations are considered. However, smaller lasers that have higher β values and lower photon numbers can be more prone to intensity noise. The robustness of stable phase-locking in coupled nanolasers with β approaching 1 and that have low photon numbers will be analyzed in a future study. Nevertheless, for the same noise level, increasing the pump power to obtain a higher SNR can help to mitigate the effect of the intensity noise [96]. Another way to squeeze the intensity noise is to use quiet pumping with the help of new designs for extreme dielectric confinement, such as a bow-tie structure [97].

2.7 Summary

The theoretical effects of varying the spontaneous emission factor, β, on the stability and tunability of phase-locking in two laterally coupled semiconductor lasers are presented in this study. In order to first determine how β affects the stability of the coupled system, bifurcation analysis is performed over the laser rate equations using numerical continuation. Initial results with a simplistic model considering constant and equal pump rates, identical resonance frequencies and an imaginary coupling coefficient reveal that increasing β leads to an overall expansion of the stable phase-locking regions. To account for realistic experimental conditions and practical device designs, additional control parameters such as varying pump rate, frequency detuning and complex coupling coefficients were considered in the model. The desirable effects of high-β on stability were found to be robust to the addition of these multiple parameters. More importantly, the stable in-phase locking regions, conducive for generating high output optical power, were observed to increase in area as a direct result of increasing β. Such stability enhancement becomes even more significant for $\beta \geq 0.89$, where the in-phase solutions are stable over a wide range of coupling coefficients and frequency detuning. During the stability analysis, regions of bistability that increase in area due to increasing β were also observed. The simultaneous coexistence of two solutions in this manner can find applications in optical memories. Finally, higher values of β were also found to exert influence on the range of stable phase differences attainable from a laterally coupled system. By breaking the symmetry of pumping for the two lasers while altering β, a range of phase differences as wide as π (from $-\pi/2$ to $\pi/2$) was attained for $\beta > 0.025$. Wide ranges of tunability of this form are desirable in applications that require a large scanning angle and beam steering such as in lidar systems. This is the first study demonstrating rigorous analysis on the specific effects of high-β on the phase-locking stability and tunability of laterally coupled semiconductor lasers, to the best of our knowledge. Future analysis on the stability of coupled lasers can consider more than just two interacting lasers, specific coupling geometries and the contribution from intrinsic noise terms.

2.8 Acknowledgement

Chapter 2, in part, is a reprint of the material as it appears in S. Jiang, S. S. Deka, S. H.

Pan, and Y. Fainman, “Effects of High-β on Phase-Locking Stability and Tunability in Laterally Coupled Lasers”, *IEEE Journal of Selected Topics in Quantum Electronics*, vol. 28, no. 1, Jan./Feb. 2022. The dissertation author was the primary investigator and author of the publications and the unpublished materials.

Chapter 3 Mode selection in bridge-coupled nanolasers

3.1 Introduction

Nanolasers have attracted considerable attention in the past two decades due to their ultra-compact footprint, low power consumption, and high modulation speed, that are the outstanding merits of on-chip light sources that meet the needs of various applications, such as biosensing [1], super-resolution imaging [3], and optical interconnects [8]. Previously, most of the research on nanolasers has focused on the demonstration of individual devices [24, 28, 41, 44, 45, 98]. Recently, there is an escalating interest in exploring the coupling behavior in microscale and nanoscale lasers, as a plethora of fascinating dynamics can be achieved in these platforms, including spontaneous symmetry breaking, synchronization, as well as mode selection and switching [56, 63, 64, 75, 99, 100].

Realizing stable phase-locking in coupled nanolasers has been the long-established pursuit for many applications. Specifically, with all the constituents in an array operating in-phase, on-chip nanolaser arrays can be applied in high-power optical beam generation for bio-imaging [52], remote sensing [66], and optical communication [55]. Phase-locked nanolaser arrays with binary phases across the array can contribute to the next generation optical cryptography [54], and those with shifted phases between adjacent elements have shown great potential in virtual and augmented reality devices [101, 102] and lidar systems [53]. Room-temperature metallo-dielectric nanolasers (MDNLs) are excellent candidates to be employed in these nanolaser arrays, as their three- dimensional (3D) subwavelength footprint allows denser on-chip integration.

3.2 Manipulation of coupling

To design chip-scale phase-locked MDNL arrays, in-depth understanding of their building blocks in the form of two coupled lasers is important. The first step is to investigate their dynamics and stability, which can be predicted by the coupled laser rate equations [63, 64, 99, 100]. The physical coupling between two cavities can be mathematically described by a complex coupling coefficient $i\kappa + \gamma$, with κ and γ being the dispersive and dissipative coupling rates, respectively, that can be calculated from the resonance frequencies and quality (Q) factors of the in phase and out-of-phase modes [56]. Among all the coupling platforms, evanescently coupled MDNLs are easy to fabricate and can be densely integrated on a chip. Supermodes with separate resonance frequencies and Q factors due to optical coupling have been observed in such platforms [39]. However, theoretical dynamical analysis of such structure has revealed that they have coupling coefficients that lead to the two cavities always operating in the out-of-phase mode [99].

Selection of the in-phase or out-of-phase lasing modes in coupled photonic crystal lasers can be achieved by barrier engineering [57, 58]. Similarly, in this chapter, we have experimentally demonstrated the mode selection by incorporating a coupling bridge between dual nanolasers. The geometry of the coupling region adds extra degrees of freedom that allows to modify the resonance frequencies and the losses for both modes such that only one mode is supported. Specifically, we have investigated the dependence of coupling coefficients on the length of the composite bridge, then fabricated and characterized bridge-coupled devices with desired parameters. We have confirmed the lasing action of these devices through the light-in light-out (L-L) characterization and identified the operating mode by measuring their near-field and far-field emission patterns. This work, to the best of our knowledge, is the first demonstration of in-phase and out-of-phase mode selection in coupled MDNLs.

3.3 Bridge-coupled structure

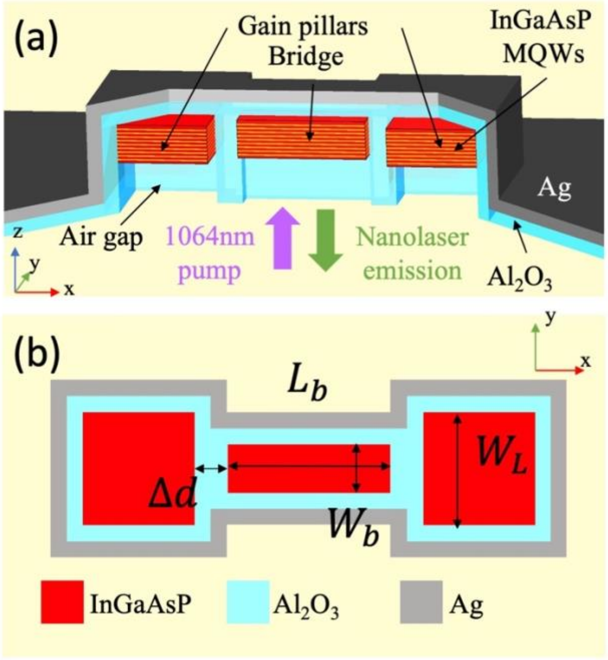

Figure 3.1 (a) 3-D schematic of the bridge-coupled nanolaser. (b) Cross-section of the structure.

The 3-D design of the bridge-coupled nanolasers is shown in Figure **3.1**(a), and the cross-section is shown in Figure **3.1**(b). The structure is constituted of two rectangular nanolasers and a composite coupling bridge in between. The gain pillars and the bridge core are composed of 9 pairs of InGaAsP multiple quantum wells (MQWs). The gain pillars have a width of W_L and a height of 300nm, whereas the bridge core has a length of L_b and a width of W_b. The Al_2O_3 dielectric layer serves as a shield between the gain and the metal cladding to lower the lasing threshold [38], while allowing photon tunneling between the rectangular shaped lasers and the composite bridge. The distance between the gain pillars and the coupling bridge Δd is 170nm. Throughout the work, W_b is kept constant at 300nm., which ensures sufficient photon coupling between the two gain pillars and maintains their high Q factors by having most of the optical field localized in the gain pillars. See Appendix B for details of the fabrication steps.

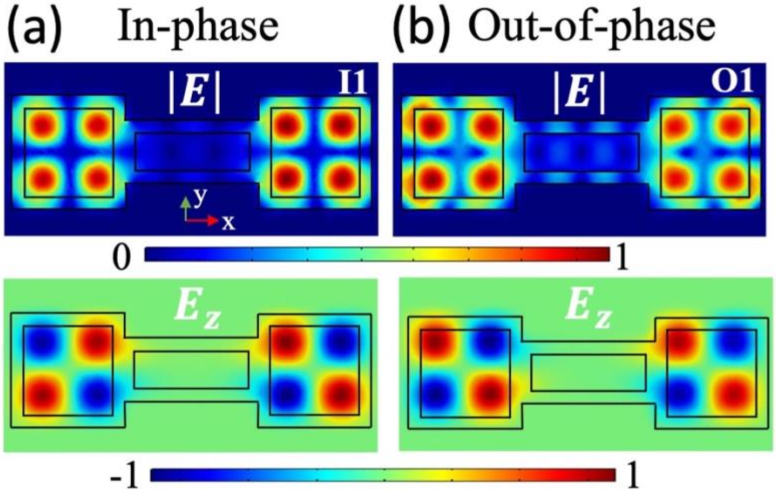

Figure 3.2 Mode profiles of (a) the in-phase mode and (d) the out-of-phase mode for a device with $L_b = 860nm, W_b = 300nm, W_L = 700nm$, and Δd=170nm, with the top row showing $|E|$ and bottom row showing E_z. Black lines denote the material boundaries shown in Figure 3.1(b).

Figure **3.2**(a) and (b) show the normalized electrical field $|E|$ and the longitudinal component E_z of the two supermodes, i.e., in-phase and out-of-phase modes, respectively, obtained by a 3D finite-element-method (FEM) simulation in COMSOL. These two modes have the highest Q factors and frequencies that are within the gain spectrum of the InGaAsP MQWs. We can observe an axial (or translational) symmetry of the E_z field in the two pillars and an odd (or even) number of lobes within the bridge region in $|E|$ for the in-phase (or out-of-phase) mode shown in Figure **3.2**(a) (or (b)). The fabrication process of bridge-coupled nanolasers generally follows that of a single MDNL, as reported in [28]. Scanning electron microscope (SEM) images of the device after important fabrication steps including dry etching using reactive ion etching, Al_2O_3 shield formation using atomic layer deposition (ALD), and Ag cladding deposition using electron beam evaporation, are shown in Figure **3.3**(a)-(b), respectively. The metal-coated sample is then transferred onto a copper substrate using silver epoxy for better heat dissipation.

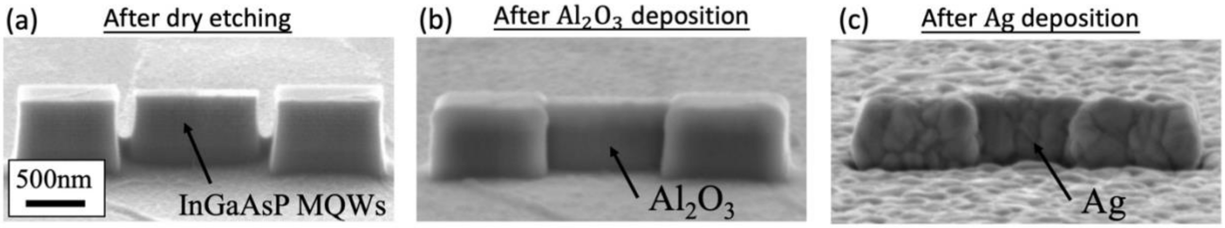

Figure 3.3 SEM images of the device after fabrication steps: (a) dry etching, (b) Al_2O_3 deposition, and (c) Ag deposition, respectively.

3.4 Effect of bridge-length

To understand the influence of the bridge geometry on the mode selection of bridge-coupled nanolasers, we first vary the length of the gain bridge L_b while keeping $W_b = 300nm$ and $\Delta d = 170nm$ constant and calculate the corresponding eigenfrequencies $f_{i,o}$ and the Q factors $Q_{i,o}$ of the two supermodes (see Figure **3.4** (a) and (b)). Here, the subscripts i and o stand for in-phase and out-of-phase modes, respectively. The coupling coefficients κ and γ can be calculated from $f_{i,o}$ and $Q_{i,o}$ as [56]:

$$\kappa = \pi(f_i - f_o) \tag{3.1a}$$

$$\gamma = \frac{\pi}{2}\left(\frac{f_o}{Q_o} - \frac{f_i}{Q_i}\right) \tag{3.1b}$$

The dependence of κ and γ on L_b is shown in Figure **3.4** (c) and (d), respectively. When $L_b \leq 300nm$, both $f_{i,o}$ and $Q_{i,o}$ follow the trend of evanescently coupled MDNLs (yellow regions) [39]. In this regime, both κ and γ are negative, which results in a stable out-of-phase mode operation above the threshold as predicted from the rate equations [99].

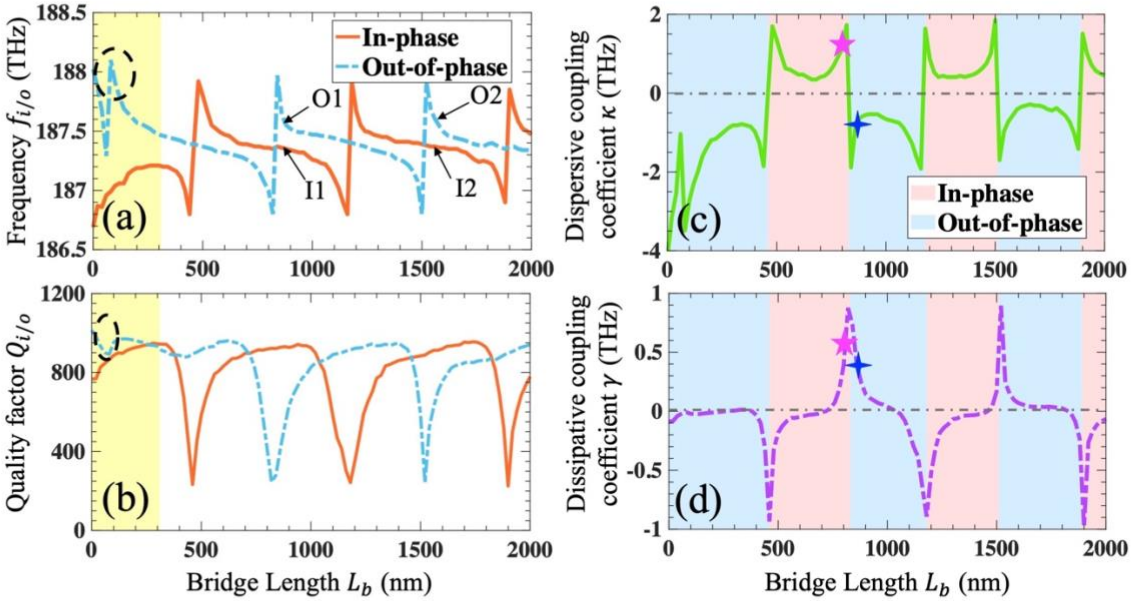

Figure 3.4 (a) Resonance frequency $f_{i,o}$ and (b) Q factor $Q_{i,o}$ of the in-phase (solid orange) and out-of-phase (dashed blue) modes versus L_b. The sudden jumps in f_o and Q_o around $L_b = 80nm$ (in black dashed circles) are due to the increased influence of the coupling bridge. (c) Dispersive κ and (d) dissipative γ coupling coefficients as functions of L_b. The pink pentagram (or blue cross) in (c) (or (d)) labels the parameters of the device I (or the device O), i.e., $L_b = 820$nm (or L_b=860nm).

When the length of the bridge L_b exceeds 300nm, periodic variations of both $f_{i,o}$ and $Q_{i,o}$ with respect to $L_b$can be observed, with a period of around 700nm. Such changes with a fixed interval can be explained by the fact that two more lobes will occupy the bridge region in the next period for each mode (see Figure **3.2**(a)-(b) and Figure **3.5**(a)-(b) for mode I1, O1, I2, and O2, respectively). Specifically, within one cycle, the increase in L_b leads to lower $f_{i,o}$ and higher $Q_{i,o}$, which is expected for a Fabry-Perot cavity such as the coupling bridge region. The sudden drop in Q factor and jump in resonance frequency mark the end of one period and the onset of the next one. The trends of $f_{i,o}$ as functions of L_b for the two modes are shifted from each other by half a period, leading to the in-phase mode having a frequency higher for half of a cycle and lower for the other half compared to that of the out-of-phase mode. Similar trends for $Q_{i,o}$ are also observed in Figure **3.4**(b). Such behavior leads to periodic sign flipping in both κ and γ, as shown in Figure **3.4**(c) and (d). The effective periods of the sign flipping for both κ and γ are around 350nm. The regions for L_b that support either in-phase or out-of-phase modes above threshold are colored in red and blue in Figure **3.4**(c) and (d), respectively. The detailed analysis of the dependence of stable phase-locking regions on κ and γ can be found in [99].

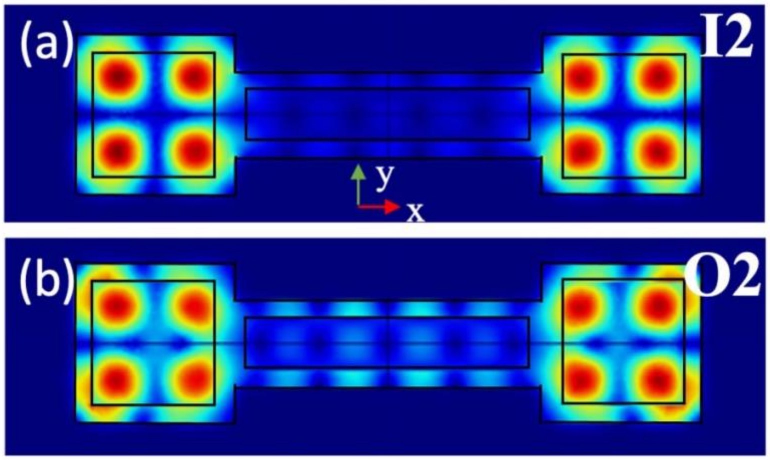

Figure 3.5 (a) Normalized electric field $|E|$ of the modes I2 and (b) O2 as labelled in Figure **3.4** (a) with L_b=1560nm.

3.5 Experimental demonstration

For experimental validation of the mode selection in bridge-coupled nanolasers, devices with varying L_b are fabricated and characterized. The laser parameters, and specifically L_b, are measured under SEM. The coupled nanolasers are optically pumped by a 1064nm laser with a pulse repetition rate of 290kHz and a pulse width of 11ns at room temperature. A long working distance microscope objective (MO) with a numerical aperture of NA=0.4 simultaneously focuses the pump beam onto the sample with a spot diameter of around 15μm and collects the coupled nanolasers output.

3.5.1 In-Phase mode operation

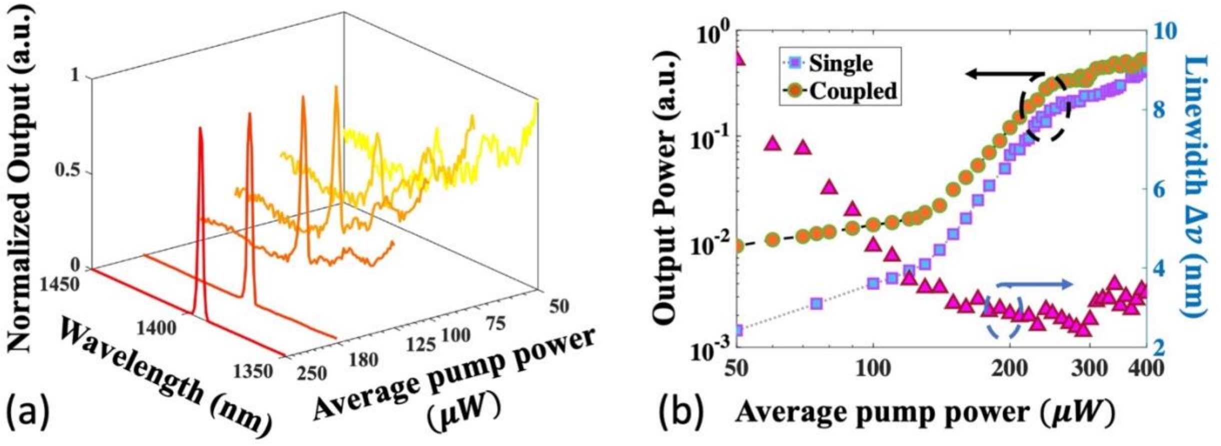

Figure 3.6 Characterization of the in-phase mode: (a) Normalized spectral evolution of the device I; (b) Log-log L-L curves of single and coupled nanolasers (left) and emission linewidth evolution of coupled nanolasers (right).

Figure **3.6** shows the characterizations of a coupled device (device I) that is designed to operate in the in-phase mode, it has a measured bridge length of $L_b = 820nm$ as denoted by the pink pentagram in Figure **3.4**(c). Figure **3.6**(a) presents the spectral evolution of device I from below to above threshold using values that best reveal the transition of the lasing peaks in different operational regimes. As the pump power increases, the broadband photoluminescence is suppressed, and a narrow emission peak emerges at around 1393nm. In Figure **3.6**(b), the kink in the log-log scale L-L curve confirms the onset of the lasing of the device I. In the same plot, linewidth narrowing and saturation above the threshold can also be seen. We have measured multiple single rectangular nanolasers that have the same width as the gain pillars in the device I, and they show similar threshold behaviors and L-L characteristics. We choose to present a typical curve of these single devices in Figure **3.6**(b). Compared with the single nanolaser, the bridge-coupled device has a similar lasing threshold ($\sim 200\mu W$ average pump power and $0.71kW/mm^2$ peak pump density), but higher output power both below and above threshold. Theoretically, the in-phase coupled device should have an output power density that is four times greater than that of a single nanolaser due to the coherent superposition of the field amplitudes of the emitted waves. This expected power scaling could be obtained if a MO with higher NA would be applied, as the one used in our experiment is insufficient to collect all the emitted light from such a small-size device.

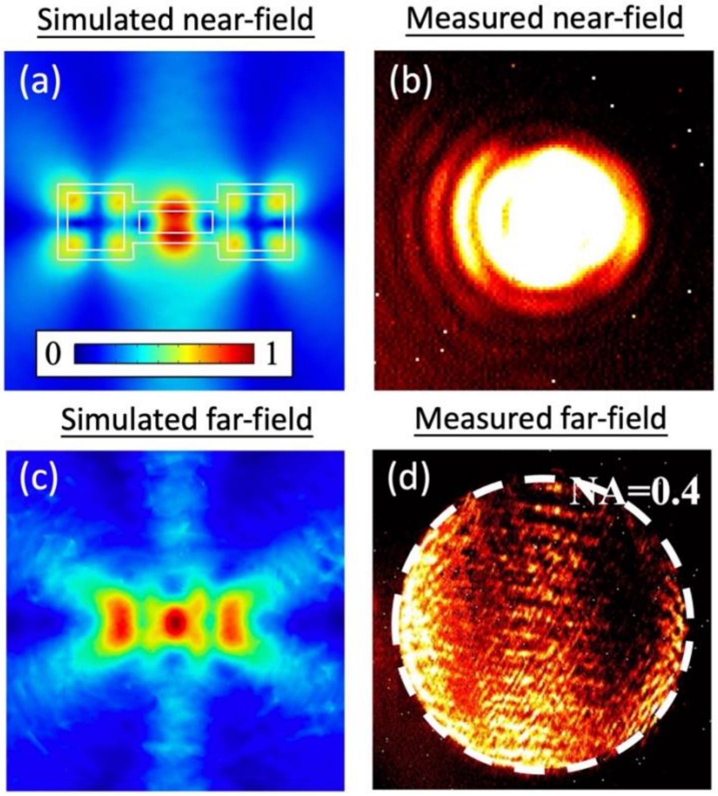

Figure 3.7 (a) Simulated and (b) measured near-field; (c) Simulated and (d) measured far-field of the device I.

To distinguish between the in-phase and out-of-phase modes, FEM simulations of their near field and far field emission are conducted. The near-field intensity profiles of the bridge-coupled nanolasers are experimentally measured by the conventional 4-f telecentric imaging system, whereas the far-field emission patterns are measured by inserting an additional lens performing a Fourier transform of the nanolaser output plane [56]. The simulation results reveal that, as expected, the in-phase mode has a peak in the center of the structure for both near-field and far-field due to the constructive interference of the two rectangular cavities, as shown in Figure **3.7**(a) and (c), respectively. Figure **3.7** (b) presents the near field of device I recorded by a CCD camera. Although the specific field distribution cannot be observed because of the low resolution of the MO and the emission saturating the camera, it can be observed that most of the energy is located in the center of the structure, suggesting the in-phase lasing mode. The orientation of the stronger fringes indicates that the constructive interference occurs between the two nano-cavities. The far-field emission pattern of the device I is presented in Figure **3.7** (d). Due to the small footprint of the coupled device, the far-field emission has a comparably large divergence angle, so only a part of the far-field emission is collected by the MO. However, a bright peak in the center of the bridge with dark field and side lobes on both sides can be identified, which matches the simulation. The asymmetric far-field mode profile is due to the slight pumping asymmetry caused by misalignment.

3.5.2 Out-of-phase mode operation

To further demonstrate that the bridge-coupled nanolasers can also support an out-of-phase mode, the device O with a measured L_b=860nm is characterized (see blue cross point in Figure **3.4**). Compared to the device I, the device O has a coupling bridge that is 40nm longer, which leads to a mode switching caused by the sign flipping of κ, as suggested in Figure **3.4**. Figure **3.8**(a) shows the emission spectra with increasing pump power, where a narrow lasing peak located around 1354nm is observed above threshold. The device O has a shorter center wavelength than the device I, which follows the same trend as the simulation. The discrepancy between the measurement and the simulation are caused by the fabrication imperfection. The lasing action is confirmed by the kink in the L-L curve of the device O, as seen in Figure **3.8** (b). The linewidth of the device O narrows with increasing pump power below threshold and reaches a plateau at around $240\mu W$ ($0.852 kW/mm^2$), marking the onset of lasing. Compared to the same single rectangular nanolaser as in Figure **3.6**(b), device O has a slightly higher threshold and higher output power below threshold due to larger gain volume, and lower output above threshold due to destructive interference. A comparison of the performance of device I and device O shows that the in-phase mode has a lower threshold and a higher output power, which was also observed for the other devices we have measured (not shown). This can be partially explained by the higher modal gain of the InGaAsP MQWs at longer wavelengths [44], which suggests that mode selection in bridge-coupled nanolasers can further benefit from the spectral mode matching of the desired lasing mode with higher MQW wafer gain.

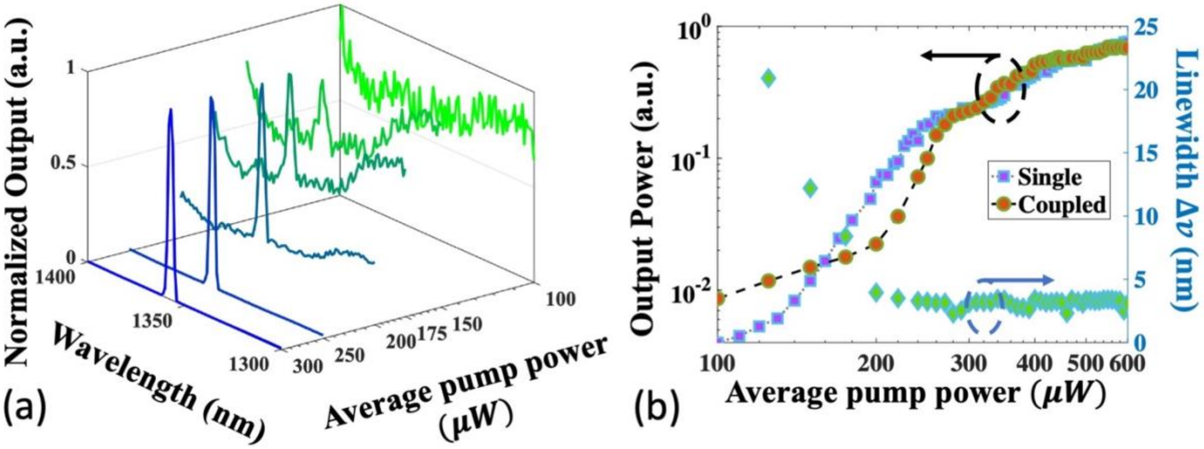

Figure 3.8 Characterization of the in-phase mode: (a) Normalized spectral evolution of the device O; (b) Log-log L-L curves of single and coupled nanolasers (left) and emission linewidth evolution of coupled nanolasers (right).

To prove that the coupled device is indeed working in the out-of-phase mode, we have also conducted FEM simulation and observed that for the out-of-phase mode, both the near-field and the far-field have vanished optical field in the center of the structure and stronger energy concentrated at the four corners due to the destructive interference between the two rectangular cavities (see Figure **3.9**(a) and (c), respectively). Good agreement between the experimentally measured near-field and far-field emission patterns (see Figure **3.9** (b) and (d), respectively) and the simulation proves the out-of-phase operating mode. In Figure **3.9**(b), the detection of the dark field in the center of the structure is prevented by the resolution limit of the MO. Note that the scattering field in the dashed white circles are caused by the surface roughness of the Ag cladding.

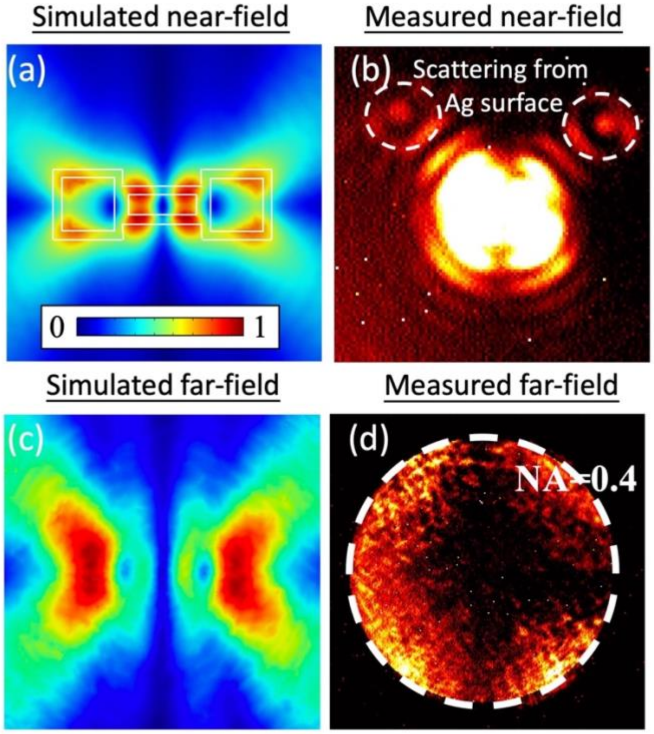

Figure 3.9 (a) Simulated and (b) measured near-field; (c) Simulated and (d) measured far-field of the device O.

3.6 Reliability testing

Indeed, the RIE etching machine we are using, i.e., Trion etcher, creates tilted sidewalls and uncertainty in the width of the lasers even if we use the same recipe every time. Most of the time, we also observe that the widths at the center of the pillars are smaller than the designed widths. In the cause of this research, in practice, we first fabricate dummy samples to obtain the values of this over-etching, then compensate for the over-etching in the design. For example, if the actual widths measured by SEM are 60-120nm smaller than the designed parameter and we want a device with 700nm width, we would write samples with widths varying from 700nm to 820nm, or even larger. We then measure the actual etched devices. Due to the limited resolution of SEM, even samples with same widths might have different measured values. To solve this challenge, we fabricate and measure many devices and obtain an average value. In this way, we can try to minimize the difference brought by the variations in the dry-etching process.

However, the dry-etching step will also introduce nonuniformity to the sample. This means that even the lasers with same parameters can have different performances, and we indeed observed this in our experiments. The fabrication difference manifest itself in two ways: 1) center wavelength of the emission shifts; and 2) variation in the output power. Due to the fabrication complexity, we only have

In Figure **3.10**, we show the statistics of our fabricated devices a few operational devices that have the same parameters within the same batch of devices, i.e., center wavelength and linear L-L curves of both single devices and the coupled devices.

The single devices all have a width of 700nm. The in-phase devices and out-of-phase devices all have $L_b = 820nm$ or 860nm, respectively. In-phase coupled device 1, out-of-phase coupled device 1, and single device 1 correspond to device I, device O and the single rectangular nanolaser in the manuscript, respectively. It can be observed that devices with same parameters still have different center wavelengths due to the fabrication imperfections. While the single devices have comparably robust emission wavelengths, the coupled devices can have a wavelength span of ~15nm due to the fabrication induced geometry difference. However, the in-phase devices always have higher emission wavelength than the out-of-phase devices, just as predicted by the simulation.

Another important observation is that, for the devices we have measured, the in-phase coupled devices always have lower lasing threshold and higher output power than the out-of-phase coupled devices. This energy efficiency is partially due to the higher modal gain at longer wavelength. In general, the in-phase coupled devices have moderately higher slope efficiency, also suggesting that the in-phase mode can be more energy efficient.

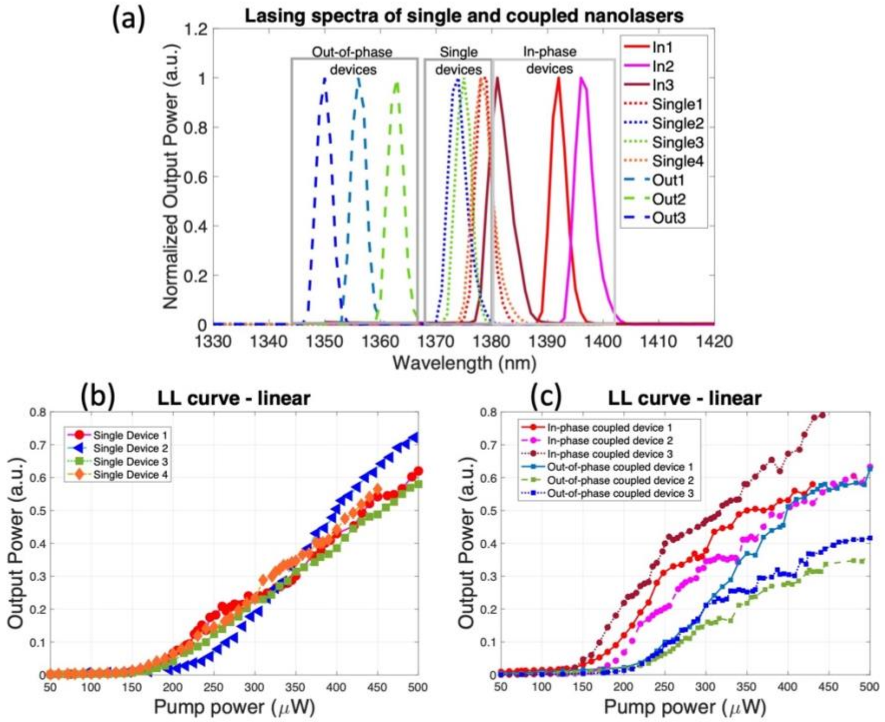

Figure 3.10 (a) Lasing spectra of single and coupled nanolasers. (b) L-L curves of the single device with $W_L = 700nm$. (c) L-L curves of the coupled devices with $L_b = 820nm$ (in-phase coupled devices) and $L_b = 860nm$ (out-of-phase coupled devices).

3.7 Summary

In summary, we have proposed and experimentally demonstrated coupled metallo-dielectric nanolasers that can lase in either an in-phase or out-of-phase mode controlled by a coupling bridge, whose length determines the specific lasing mode. We have experimentally confirmed lasing behavior from such bridge-coupled nanolasers by experimentally observing the presence of the kinks in the L-L curves, the pronounced lasing peaks in the spectra, as well as the linewidth narrowing below lasing threshold. Moreover, we have identified the lasing in-phase and the out-of-phase modes by measuring the near-field and far-field emission patterns and observed good agreement with the FEM simulations. The bridge-coupled nanolasers will serve as promising building blocks in large-scale laser arrays and pave the way for the future high-power generation, beam forming, imaging, and sensing systems that requires compactness and scalability. Future combination with nonlinear materials and electronic control can lead to controllable switching of the in-phase and out-of-phase modes in the same device, as well as leverage the nanolaser arrays for real-time control of relative phase across the aperture and high-speed operation.

3.8 Acknowledgement

Chapter 3, in part, is a reprint of the material as it appears in S. Jiang, D. Belogolovskii, S. S. Deka, S. H. Pan, and Y. Fainman, “Experimental Demonstration of Mode Selection in Bridge-Coupled Metallo-Dielectric Nanolasers”, *Optics Letters*, vol. 46, no. 23, Dec. 2021. The dissertation author was the primary investigator and author of the publications and the unpublished materials.

Chapter 4 Thermal noise and intensity noise in nanolasers

4.1 Introduction

The miniaturization of optical resonators has established nanolasers as promising coherent light source candidates for future integrated nanophotonics with wide applications in bio-sensing [103-105], imaging [106-108], far-field beam synthesis [2] and optical interconnects [109]. The ultra-compact mode volume of nanolasers also enables them to exploit the cavity quantum electrodynamics (QED) effect [47, 76, 110, 111]. In these nanocavities, conspicuous Purcell enhancement helps to dramatically increase the modulation speed and lower the power consumption for optical communication systems. However, shrinking the dimension of a nanolaser can also be detrimental to its performance. One of the intrinsic issues with nanoscale resonators is that, fundamental thermal fluctuation (FTF) is expected to be more pronounced in comparison to conventional lasers. According to the fluctuation-dissipation theorem, the variance of the temperature fluctuation ΔT is inversely proportional to the optical mode volume V [112, 113]:

$$< \Delta T^2 >= \frac{k_B T^2}{\rho c V} \tag{4.1}$$

where T is the classical temperature, ρ is the density of the host material ($g \cdot cm^{-3}$), c is the specific heat capacity ($J/g \cdot K$), and k_B is the Boltzmann constant (J/K). In semiconductor lasers, this continuous thermal fluctuation perturbs the refractive index of the resonator through the thermo-refractive effect, and hence causes the resonance frequency to fluctuate around its mean. As shown in equation (4.1), the thermal noise increases with decreasing mode volume and increasing temperature. Consequently, the bigger noise will impose a more prominent limitation on the frequency stability of the nanoscale light emitters. Therefore, understanding the impact of FTF on a nanolaser's spectral linewidth is of crucial importance, since FTF can be one of the dominant contributions to the broad linewidths measured in various nanolasers, that are usually on the order of 1nm [13, 14, 16, 17, 23-25, 27, 28, 36, 37]. Evaluating the linewidth broadening caused by FTF in nanolasers would be the first step towards engineering nanolasers to be employed in applications where narrow linewidth is desired, such as coherent optical communication [114] and near-field spectroscopy [115].

4.2 Theoretical model for thermal noise

In semiconductor resonators, thermal fluctuations perturb the refractive index of the constituent materials. Therefore, the temperature fluctuation $\Delta T(\vec{r},t)$ lead to a fundamental uncertainty of the cavity resonance via the thermo-refractive effect. By solving the temperature-perturbed wave-equation, the transient fluctuation of the frequency resonance $\Delta v(t)$ with respect to the center resonance frequency v_0 can be expressed as [116]:

$$\Delta v(t) = -\frac{v_0}{n}\frac{dn}{dT}\Delta\,\bar{T}(t) = -\frac{v_0}{n}\frac{dn}{dT}\int_V \Delta T(\vec{r},t)|E(\vec{r})|^2 d\vec{r} \tag{4.2}$$

where $\Delta\,\bar{T}(t)$ is the average thermal fluctuation over the mode volume, $\vec{E}(\vec{r})$ is the normalized electric field distribution of the eigenmode, n is the refractive index of the gain material, and

dn/dT is the thermo-optic coefficient. The center frequency v_0 can be determined by various approaches [117, 118]. In this work, v_0 is found by performing a three-dimensional (3-D) finite-element-method (FEM) simulation in COMSOL Multiphysics. The lasing mode is expected to have the highest quality factor and the lowest lasing threshold among the eigenmodes that lie within the gain spectrum of InGaAsP [39]. As shown in equation (4.2), the linewidth broadening can be estimated by determining $\Delta T(\vec{r}, t)$ and $E(\vec{r})$. Hence, in the following section, we first solve the electric field distribution $E(\vec{r})$ within the resonator. Then, we present the theoretical approach adopted to quantify the thermal fluctuations $\Delta T(\vec{r}, t)$.

4.2.1 Metallo-Dielectric Nanolaser Architecture

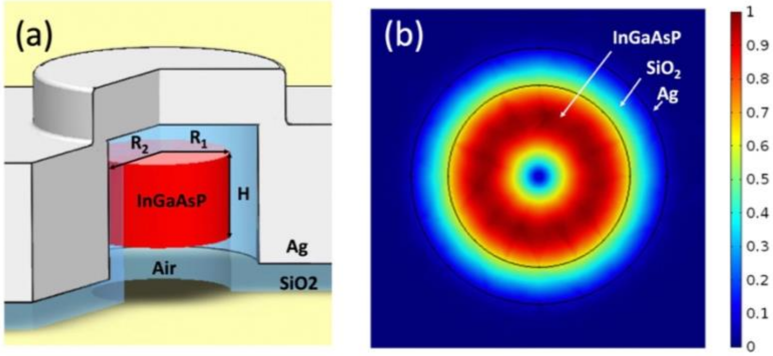

Figure 4.1 (a) 3D schematic of the metallo-dielectric nanolaser. R_1 is the radius of the gain medium InGaAsP, R_2 is the total radius of InGaAsP plus SiO_2 dielectric shield, and H is the height of the InGaAsP. The pillar is covered by adequately thick Ag cladding. The values are given in Table.I. (b) Normalized electric field distribution profile of the cross section (chosen at the center of the gain medium InGaAsP) of N-250 obtained from 3D FEM simulation. The black circles are the interfaces of InGaAsP/SiO_2 and SiO_2/Ag, respectively. Effective confinement in the gain region can be observed.

The architecture of the metallo-dielectric nanolaser under consideration throughout the manuscript is depicted in Figure **4.1**(a). The nanolaser has an InGaAsP gain medium with a radius of R_1 and a height of H. The gain region is wrapped by a SiO_2 shield, whose thickness is optimized to lower the lasing threshold [38]. The total radius of the InGaAsP core plus the SiO_2 shield is labelled as R_2. The values of R_1, R_2 and H for the devices N-250 and N-750 under consideration are given in Table **4.1**. A thick Ag cladding that covers the dielectric shield not only allows high mode confinement (Γ~86%), but also facilitates the heat dissipation of the nanolaser [24, 28, 29, 37, 42]. The metallo-dielectric nano-resonators are designed to support a transverse electric (TE) mode. For example, N-250 supports a first order TE_{011} mode, as shown in Figure **4.1**(b).

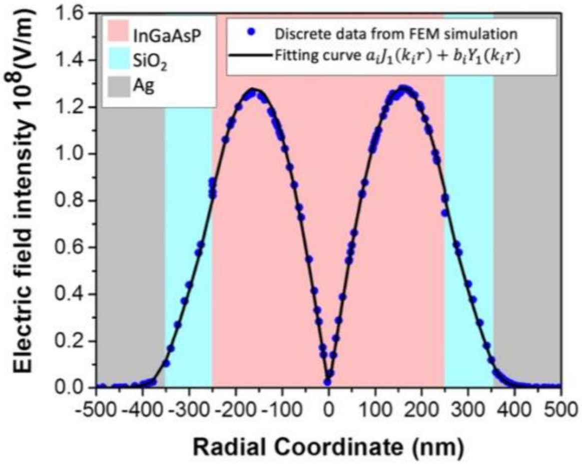

Figure 4.2 Transverse electric field distribution of the metallo-dielectric nanolaser N-250. Radius of the gain region: $R_1 = 250$nm; outer radius $R_2 = 350$nm. Radial coordinates greater than 350nm represent the metal cladding region. Blue dots are the discrete value obtained from numerical simulation. Solid black line is the corresponding fitting curve.

Table 4.1 Dimension Parameters of the Nanolasers for Calculation

Parameter (unit)	N-250	N-750
R_1 (nm)	250	750
R_2 (nm)	350	900
H (nm)	300	300

To obtain the continuous electric field $E(\vec{r})$ of a nanolaser shown in equation (4.2), a 3-D FEM simulation in COMSOL is first performed to extract the discrete electric field distribution. These discrete data are then fitted into continuous analytical solutions, that are Bessel functions, due to the radial symmetry of the cylindrical metallo-dielectric nanolasers. For example, the electric field solutions of the TE_{011} mode of N-250, as shown in Figure **4.1**(b), are the first order

Bessel functions, that can be expressed as:

$$\begin{gathered} E_{1,2}(r) = A_{1,2}J_1\big(k_{1,2}r\big) + B_{1,2}Y_1\big(k_{1,2}r\big), 0 \leq r \leq R_2 \\ E_3(r) = A_3 I_1(k_3 r) + B_3 K_1(k_3 r), r \geq R_2 \end{gathered} \tag{4.3}$$

where the subscripts denote different regions, with 1 being InGaAsP, 2 being SiO_2 and 3 being Ag. Figure **4.2** presents the plotting of equation (4.3) based on the discrete FEM simulation data. Approaches other than FEM simulations, such as in [111], can also be applied to derive the electric field in the semiconductor regions. The coefficients in the Bessel functions are given in Appendix C. Next, we derive the thermal fluctuations solutions $\Delta T(\vec{r}, t)$, the other prerequisite for evaluating the frequency shift $\Delta v(t)$.

4.2.2 Fundamental thermal noise calculation

To calculate the thermal fluctuations, $\Delta T(\vec{r}, t)$, a 2-D heat transport model with the boundary conditions imposed by the nanocavity structure is adopted. This model is based on a general assumption that the thermal fluctuations can be decomposed into a radial mode and a longitudinal mode. For metallo-dielectric nanolasers, the in-plane radial mode will be chosen for the following calculation. This choice is validated by two facts: 1) the in-plane-mode-dominated heat dissipation; 2) the resonant frequency of the TE mode shows more dependence on radial properties of the resonator. The 2-D heat transport model that we intend to use is governed by the stochastic heat transport equation. This equation includes a *Langevin* noise source $F(\vec{r}, t)$ to account for the randomness of the thermal fluctuation [119, 120], and is expressed as:

$$\frac{\partial \Delta T(\vec{r}, t)}{\partial t} - D_T \nabla_{\vec{r}}^2 \Delta T(\vec{r}, t) = F(\vec{r}, t) \tag{4.4}$$

where $D_T(\mathrm{cm}^2\mathrm{s}^2)$ is the thermal diffusion constant that we assume is homogeneous throughout each medium. $D_T = \eta/\rho c$, in which η $(W/cm \cdot K)$ is the thermal conductivity. Because the driving source $F(\vec{r}, t)$ is uncorrelated in space and time, the Green's function method is applied to derive the analytical solution for the thermal fluctuations $\Delta T(\vec{r}, t)$ [120]. To compute the broadening of the emission linewidth, the power spectral density (PSD) of the frequency noise $S_f(w)$ needs to be evaluated (where the subscript denotes the frequency noise). We restrict the noise source considered in this manuscript to only FTF. Therefore, the frequency noise is solely generated by thermal noise, and hence knowing $S_f(w)$ requires knowledge of the PSD of the thermal noise $S_{\Delta T}(w)$. A Fourier transform is performed on the corresponding Green's function of equation (4.4) and gives:

$$iwG(\vec{r}, \vec{r}'; iw) - D_T \nabla_{\vec{r}}^2 G(\vec{r}, \vec{r}'; iw) = \delta(\vec{r} - \vec{r}') \tag{4.5}$$

where w is the Fourier angular frequency and r' is the coordinate of the spatially uncorrelated *Langevin* heat source. The thermal fluctuations in the frequency domain then can be derived from the definition of Green's function as:

$$\Delta\tilde{T}(\vec{r}, w) = \int_V G(\vec{r}, \vec{r}'; iw)\, \tilde{F}(\vec{r}, iw) d\vec{r}' \tag{4.6}$$

Equation (4.6) shows that, in order to obtain $S_{\Delta T}(w)$ to evaluate the parasitic frequency noise $S_f(w)$, the spectral density of the Langevin noise source $F(\vec{r}, t)$ is needed. The spectral autocorrelation of the Langevin source that satisfies the fluctuation-dissipation theorem is shown to be [121, 122]:

$$< \tilde{F}(r, iw)\tilde{F}^*(r', iw') >= \frac{4\pi D_T A\, k_B T^2}{\rho c V} \nabla_r \nabla_{r'} \delta(r - r')\delta(w - w') \tag{4.7}$$

where A is the area of the InGaAsP cross-section. Here we assume that the heat source lies in the gain medium, since most of the energy is well confined to it (see Figure **4.1**(b)). According to Wiener-Kintchin theorem, the single-sided PSD $S_{\Delta T}(w)$ is shown to be (see Appendix D):

$$S_{\Delta T}(w) = \frac{1}{\pi} < \Delta\,\tilde{T}(w)\Delta\tilde{T}^*(w') >= \frac{4Ak_BT^2}{\rho cV} \times \int_{\mathrm{V}}\int_{V} Re[G(r,r';iw)]|E(r)|^2|E(r')|^2 rr'drdr' \tag{4.8}$$

The vanishing of the space-dependence of $S_{\Delta T}(w)$ is due to the fact that spatially dependent thermal fluctuations are integrated over the entire mode volume, as shown in equation (4.2).

To obtain the particular solutions $G(r,r';iw)$ in equation (4.8) for each domain, appropriate boundary conditions are applied to the general solutions. Due to the axial symmetry of the nanolasers, the general solutions are Bessel functions of the zeroth order. The Ag cladding acts as an effective heat sink. Therefore, we assume that fluctuations are absent at the SiO$_2$/Ag interface, i.e., $\Delta T|_{R_2} = 0$. With the detailed boundary conditions shown in Appendix C, we arrive at the Green's function solutions for different regions as:

$$\begin{gathered} 0 \le r \le r', G_1^{<}(r,r';iw) = g_1(r')J_0(k_{\rho 1}r) \\ r' \le r \le R_1, G_1^{<}(r,r';iw) = g_1(r')J_0(k_{\rho 1}r) \\ R_1 \le r \le R_2, G_2(r,r';iw) = g_3(r')J_0(k_{\rho 2}r) + h_3(r')Y_0(k\rho_2 r) \end{gathered} \tag{4.9}$$

where $k_{\rho 1} = \sqrt{-iw/D_1}$, $k_{\rho 2} = \sqrt{-iw/D_2}$. The Hankel Function $H_0^{(1)}$ accounts for the decaying of the heat diffusion away from the heat source and satisfies the singularity at the point heat source [123]. The expressions for g_i and h_i are given in Appendix C. Our analytical solutions present the first set of solutions of the thermal fluctuations in composite structures with semiconductor gain and metal clad.

By substituting the solutions for the Green's function and the electric field as stated in equations (4.9) and (4.3) into (4.8), we can obtain the PSD for FTF $S_{\Delta T}(w)$. Subsequently, the frequency noise $S_f(w)$ introduced by FTF and the linewidth broadening will be calculated next.

4.2.3 Frequency noise and linewidth broadening

To evaluate the PSD of the frequency noise generated by FTF, a Fourier transform is performed on the transient autocorrelation of the instantaneous frequency deviation $\Delta v(t)$ in equation (4.2). Since $\mathit{\Delta} v(t) = \mathit{\Delta} w(t)/2\pi$, we can also relate $S_f(f)$ and $S_f(w)$ as:

$$S_f(w) = 4\pi^2 S_f(f) = 4\pi^2\left(-\frac{v_0}{n}\frac{dn}{dT}\right)^2 S_{\mathit{\Delta} T}(w) \tag{4.10}$$

where $f = w/2\pi$ is the Fourier Transform basis frequency. To evaluate the linewidth broadening, we transfer the frequency noise into the statistics of the phase noise. The variance of the fluctuation of the optical phase $\mathit{\Delta}\phi$ reads [34]:

$$< \mathit{\Delta}\phi^2 >= \frac{\tau^2}{\pi}\int_0^{+\infty} S_f(w)\,\frac{sin^2\left(\frac{w\tau}{2}\right)}{(w\tau/2)^2}\,dw \tag{4.11}$$

where τ is the delay time in the autocorrelation function of the electric field, that is defined by:

$$< E(t)E^*(t-\tau) >= I_0\; exp(j2\pi v_0\tau)\,\langle exp(j\mathit{\Delta}\phi)\rangle \tag{4.12}$$

in which $\langle exp(j\mathit{\Delta}\phi)\rangle = exp(-\langle\Delta\phi^2\rangle/2)$ by assuming that $\Delta\phi$ follows a Gaussian distribution. This can be justified by the fact that the phase noise is introduced by many independent noise events [124]. We assume that FTF is the only noise source in the nanocavity, and the finite linewidth Δv is solely generated by the thermal noise, with Schawlow-Townes-Henry linewidth being neglected. As a result, the linewidth broadening can be taken to be twice the 3-dB bandwidth of the single-sided $S_{\Delta v}(\Delta v)$ spectrum, which is the spectral decomposition of equation (4.12). $\Delta v = v - v_0$ is the frequency deviation from the center frequency. Then, we can derive $S_{\Delta v}(\Delta v)$ by taking a Fourier transform of equation (4.12) yielding,

$$S_{\mathit{\Delta} v}(\mathit{\Delta} v) = I_0\int_{-\infty}^{\infty} exp(j2\pi\mathit{\Delta} v\tau)\; exp\left(-\frac{< \mathit{\Delta}\phi^2 >}{2}\right)d\tau \tag{4.13}$$

Table 4.2 Material Parameters of the Nanolasers for Calculations of the Linewidth at 300K [125].

Symbol (unit)	Quantity	InGaAsP	SiO_2
$\eta\ (W/cm \cdot K)$	Thermal conductivity	4.4	1.0
$c\ (J/g \cdot K)$	Specific heat capacity	0.31	0.74
$\rho\ (g/cm^3)$	density	4.8	2.2
$D_T\ (cm^2/s)$	Thermal diffusion constant	2.90	0.61
n	Refractive index	3.4	1.46
$dn/dT\ (10^{-4}/K)$	Thermo-optic coefficient	2	0.14

In the following section, we present the calculation results of both frequency noise and linewidth broadening using the parameters summarized in Table **4.2**.

4.3 Simulation results of thermal noise

In this section, numerical simulation results of the impact of FTF on the frequency noise and linewidth broadening in N-250 and N-750 are presented.

4.3.1 Dependence on mode volume

Figure **4.3**(a) shows the PSD of the frequency noise $S_f(f)$ of N-250 under ambient temperature 300K, 77K and 4K. The frequency noise $S_f(f)$ spectra behave as a low pass filter with a 3-dB bandwidth of ~ 6.1MHz. As shown in Figure **4.3**(a), $S_f(f)$ at room temperature (300K) is 4 orders of magnitude higher than that at 4K. Utilizing equations (4.10)-(4.13), the normalized single-sided PSD $S_{\Delta v}(\Delta v)$ for the frequency shift around the center frequency $\Delta v = v - v_0$ can be calculated and shown in Figure **4.3**(b). From this figure, the finite linewidth can then be read out as twice the 3-dB bandwidth of $S_{\Delta v}(\Delta v)$. We then convert Δv into $\Delta\lambda$ for a more straight-forward understanding of the results. The linewidth broadening caused by FTF are estimated to be 1.14nm, 0.31nm and 5.4pm at 300K, 77K, and 4K, respectively. As we can see for

N-250, due to the ultra-small optical cavity, FTF imposes a large limitation on the resonance stability via the thermo-refractive effect and induces a pronounced spectral linewidth under room temperature.

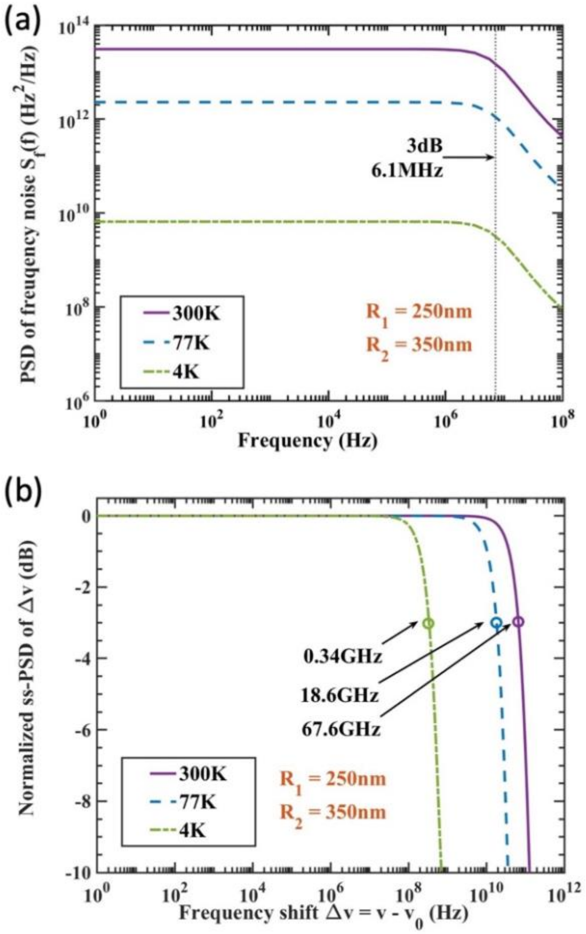

Figure 4.3 (a) PSD of the frequency noise $S_f(f)$ due to FTF at different ambient temperatures 300K (purple solid line), 77K (blue dashed line), and 4K (green dash-dotted line) in N-250. The grey vertical dotted lines are the 3-dB cut-off frequency. (b) The normalized single-sided PSD $S_{\Delta v}(\Delta v)$ of the frequency shift to the central frequency $\Delta v = v - v_0$ (Hz) due to FTF under different ambient temperatures 300K, 77K, and 4K for N-250. The 3-dB are 67.6GHz, 18.6GHz, and 0.34GHz, that correspond to linewidth broadenings of 1.14nm, 0.31nm, and 5.4pm under 300K, 77K, and 4K, respectively.

To better elucidate the impact of the decreasing mode volume, we investigate and compare the frequency noise and linewidth broadening in a larger cavity N-750 at the same temperatures. While N-250 has an inner radius of R_1 =250nm and an outer radius R_2 = 350nm, N-750 has R_1 =750nm and R_2 = 900nm. The electric field profile of N-750 from 3-D FEM simulation is depicted in Figure **4.4**(a). As five lobes in a semicircle are shown, the electric field solutions of N-750 are the fifth-order Bessel functions. Same fitting method described in Chapter 4.2 is adopted to derive a continuous field distribution from the discrete data obtained from FEM simulations.

The PSD of frequency noise spectra for the device N-750 are presented in Figure **4.4**(b). To understand how the dimensions of nanoscale cavities influence their linewidth performance, we compare the values at the plateau for N-250 and N-750 at the same temperature. From the observation of these results, a slightly lower frequency noise generated by FTF could be seen for N-750. Moreover, the 3-dB bandwidth of $S_f(f)$ for N-750, which is around 1.3MHz, is noticeably smaller than that of N-250, which is around 6.1MHz. A comparison between Figure **4.3**(a) and Figure **4.4**(b) implies that the nanoscale cavities not only escalate the frequency noise in low frequencies, but also expand the bandwidth for the thermal fluctuations.

Figure **4.4** (c) shows the linewidth broadening caused by FTF for N-750. We estimate the linewidth broadenings due to FTF as 0.16nm, 0.04nm and 2pm, corresponding to ambient temperatures of 300K, 77K and 4K, respectively. By comparing the values of the two devices for the same temperature, the significantly large difference between N-250 and N-750 in linewidths is observed. This confirms the hypothesis we made in the last section that a larger finite linewidth will be generated due to the reduction of the device dimensions. For instance, at room temperature (300K), N-250 has a radius 3 times smaller than that of N-750 while showing a 7 times larger thermal broadening compared to that of N-750. Our calculation corroborates the idea that nanoscale optical cavities are more prone to FTF than lasers with larger mode volumes, and thus exhibits broader linewidths due to the parasitic frequency noise.

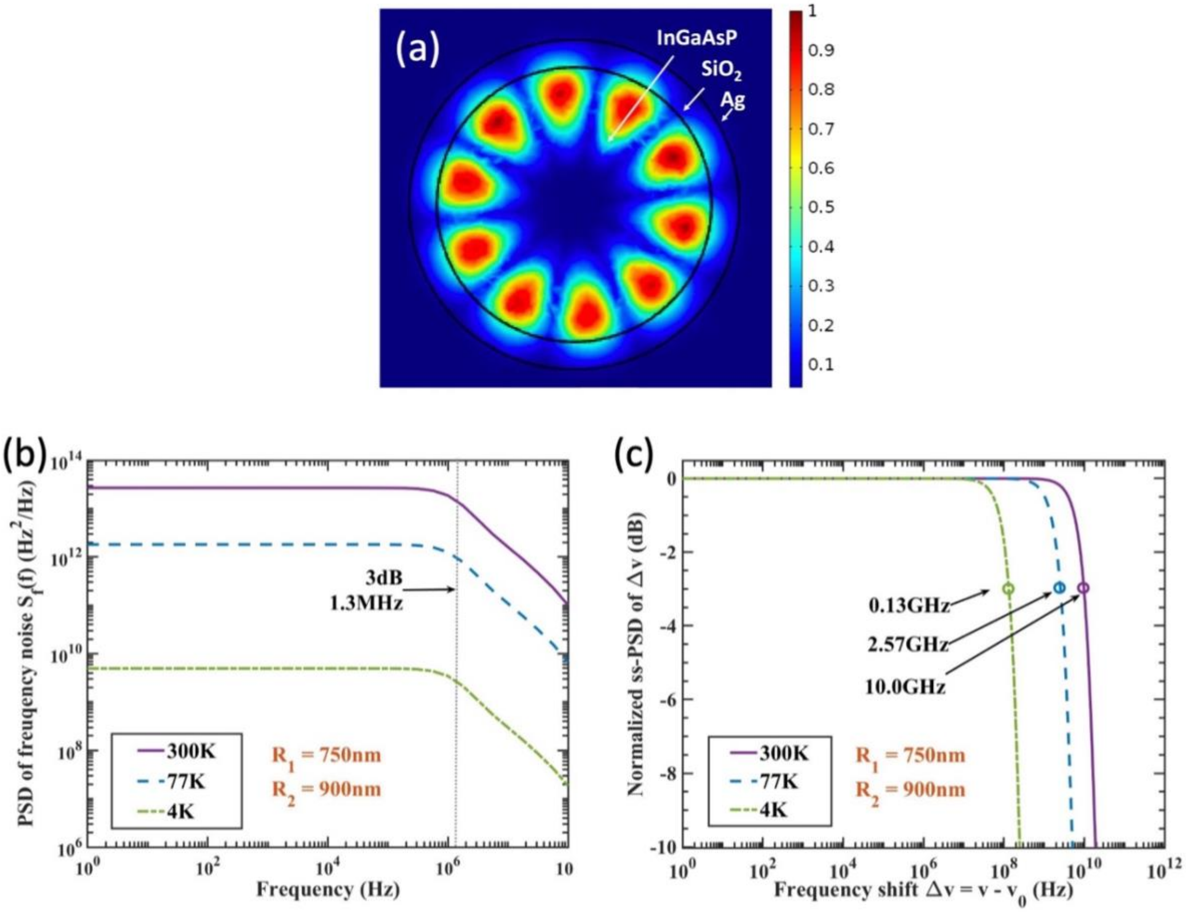

Figure 4.4 (a) Normalized Electric field distribution profile of the cross section (chosen at the center of the gain medium InGaAsP) of N-750 obtained from 3D FEM simulation. (b) PSD of the frequency noise $S_f(f)$ due to FTF at different ambient temperatures 300K (purple solid line), 77K (blue dashed line), and 4K (green dash-dotted line) in N-750. The grey vertical dotted lines are the 3-dB cut-off frequency. (c) The normalized single-sided PSD $S_{\Delta v}(\Delta v)$ of the frequency shift to the central frequency $\Delta v = v - v_0$ (Hz) due to FTF under different ambient temperatures 300K, 77K, and 4K for N-750. The 3-dB are 10.0GHz, 2.57GHz, and 0.13GHz, that correspond to linewidth broadenings of 0.16nm, 0.04nm, and 2pm under 300K, 77K, and 4K, respectively.

4.3.2 Dependence on ambient temperature

Other than nanolaser's dimension, the ambient temperature is also a crucial factor in determining the finite linewidth generated by FTF. Figure **4.5** shows the trend of the linewidth increasing temperature for N-250 and N-750. Discrete ambient temperatures are chosen for revealing the trend, as metal-clad nanolasers are reported to show lasing action under these temperatures [29, 30, 37, 41, 126]. An almost linear relation between linewidth broadening caused by FTF and ambient temperature can be seen for both N-250 and N-750. A linear fitting for N-250 shows $\Delta v(GHz) = 0.4511 \times T(K) + 0.1578$. Similarly, for N-750 the curve can be fitted into $\Delta v(GHz) = 0.06525 \times T(K) + 0.1488$. For the purpose of practical implementation, the fitting curves provide a good estimation for the finite linewidths generated due to FTF at any other temperature.

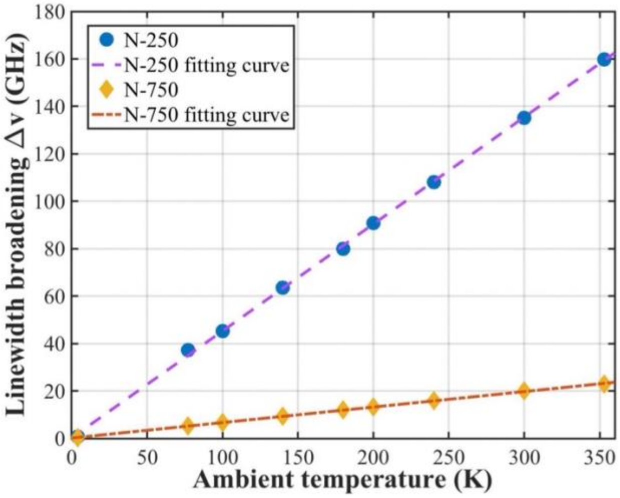

Figure 4.5 Linewidth broadening of N-250 and N-750 caused by FTF at ambient temperatures of 4K, 77K, 100K, 140K, 180K, 200K, 240K, 300K, as reported in previous studies, and 353K, as estimated by [125]. For N-250, the fitting curve is $\Delta v(GHz)=0.4511\times T(K)+0.1578$, with a coefficient of determination $R^2 = 0.9995$. For N-750, $\Delta v(GHz)=0.06525\times T(K)+0.1488$, with $R^2 = 0.9993$.

4.3.3 Dependence on nanolaser structure

Table 4.3 Linewidth Broadening under Room Temperature with Varying Radius of Gain Region and a Fixed Outer Radius

$R_2 = 350nm$			
$R_1(nm)$	225	250	275
$\Delta v(GHz)$	137.2	135.1	134.2
$\Delta\lambda(nm)$	1.06	1.14	1.22
$R_2 = 900nm$			
$R_1(nm)$	750	775	800
$\Delta v(GHz)$	20	19.2	18.3
$\Delta\lambda(nm)$	0.16	0.16	0.15

We further study how the linewidth broadening from thermal fluctuations depends on a nanolaser's geometry, given that the electric field distribution of a nanolaser and the Green's function solutions are both geometry-dependent. We show that given a fixed outer radius R_2, the linewidth broadening Δv (in Hz) due to FTF also shows a slight dependence on the radius of the active region R_1. Table **4.3** presents the linewidth broadening under room temperature as R_1 varies around its optimal thickness [38], i.e. lowest lasing threshold. As shown for both $R_2 = 350nm$ and $R_2 = 900nm$, a larger gain radius R_1 induces a smaller finite linewidth Δv. However, the variation of Δv caused by the radius change is only ~ 1% of Δv. Therefore, the linewidth broadening shows trivial dependence on the radius of R_1 with a fixed R_2, on the premise that R_1 varies within its optimal region.

Although the work presented here is based purely on numerical analysis, a comparison with experimental results found in literature can still be made. The N-750 device studied in this work is very similar to a device, whose lasing characterization has already been reported in [29], in terms of both physical dimension and material composition. The only difference is that instead of InGaAsP, InGaAs is utilized as the gain material. However, the optical and thermal properties of InGaAs and InGaAsP are very similar. This qualifies our calculation for N-750 as a good estimation of the FTF generated in the reported device. At 77K, in comparison to the simulation result of 0.04 nm found in this study, the empirical linewidth is 0.9nm in [29]. This indicates that FTF is not a negligible noise source for nanolaser linewidth at this temperature. The discrepancy can be explained by three factors: 1) The interior temperature of the device can be much higher than the ambient temperature while being pumped. For example, [125] shows that the internal lattice temperature of a device can be 53K higher than the ambient temperature during experiment.

Therefore, a broader linewidth is expected for a higher temperature. 2) Pump fluctuations also contribute to the thermal fluctuations in a nanolaser through thermal impedance [127]. 3) The empirical linewidth reported in [29] is limited by the resolution of the spectrometer. The actual linewidth, in principle, can be much smaller than 0.9nm, Therefore, it can be inferred that FTF can be a pronounced contribution to the linewidth broadening in metallo-dielectric nanolasers.

4.4 Photon and carrier fluctuations

In reality, other than thermal fluctuation, photon and carrier fluctuation, that are caused by the random recombination of photons and carriers, can also cause linewidth broadening even when no external current modulation is applied. The photon and carrier fluctuation causes variations in the output power and wavelength, which creates the finite linewidth. In semiconductor lasers, the non-zero amplitude and phase coupling further complicates this effect. In this section, the relative intensity noise induced by these effects will be studied.

4.4.1 Relative intensity noise

The laser output in the frequency domain can be expressed as: $S(f) = \bar{S} + \delta S(f)$, where $\bar{S}$ is the steady state photon density, and $\delta S(f)$ is the relative fluctuations. The relative intensity noise (RIN) is then defined as:

$$RIN(f) = \frac{\langle \delta S(f) \delta S^*(f) \rangle}{\bar{S}^2} \tag{4.14}$$

Due to the coupling between photon and carrier, RIN provides the information of not only photon noise but also carrier noise. To determine the laser RIN and carrier noise, we must find the spectral density of the output power and carrier noise fluctuations. For this purpose, Langevin noise source F_S and F_N are added to the coupled laser rate equations of photon and carrier density:

$$\frac{dS(t)}{dt} = \Gamma g_0(N - N_0)S - \gamma_p S + \Gamma\beta N\gamma_c + F_S \tag{4.15a}$$

$$\frac{dN(t)}{dt} = P - \beta N\gamma_c - g_0(N - N_0)S + F_N \tag{4.15b}$$

We can use small signal analysis to arrive at the rate equations for only the small perturbations, i.e., replace the photon and carrier density with $S(t) = \bar{S} + \delta S(t)$ and $N(t) = \bar{N} + \delta N(t)$, set the steady state terms to zero, and leave only the equations for $\delta S(t)$ and $\delta N(t)$.

$$\frac{d\delta S(t)}{dt} = -\gamma_{SS}\delta S(t) + \gamma_{SN}\delta N(t) + F_S(t) \tag{4.16a}$$

$$\frac{d\delta N(t)}{dt} = -\gamma_{NN}\delta N(t) + \gamma_{NS}\delta S(t) + F_N(t) \tag{4.16b}$$

where $\gamma_{SS} = -\Gamma g_0(\bar{N} - N_0) + \gamma_p, \gamma_{SN} = \Gamma(g_0\bar{S} + \gamma_c\beta), \gamma_{NN} = \gamma_c + g_0\bar{S}, \gamma_{NS} = g_0(\bar{N} - N_0)$. To solve for the spectral linewidth, we will conduct the analysis in frequency domain by performing a Fourier transform to equation (4.16). The photon and carrier fluctuations in the frequency domain can be seen to be the sum of two Langevin noise sources each goes through a transfer function:

$$\delta\tilde{S}(w) = H_{SN}(w)\tilde{F}_N(w) + H_{SS}(w)\tilde{F}_S(w) \tag{4.17a}$$

$$\delta\widetilde{N}(w) = H_{NS}(w)\tilde{F}_S(w) + H_{NN}(w)\tilde{F}_N(w) \tag{4.17a}$$

where $H_{SN}(w) = \frac{\gamma_{SN}H(w)}{w_R^2}, H_{SS}(w) = \frac{(\gamma_{NN}+iw)H(w)}{w_R^2}, H_{NS}(w) = \frac{\gamma_{NS}H(w)}{w_R^2}, H_{NN}(w) = \frac{(\gamma_{SS}+iw)H(w)}{w_R^2}$, $H(w) = \frac{w_R^2}{w_R^2 - w^2 + iw\gamma}, w_R^2 = \gamma_{NN}\gamma_{SS} + \gamma_{SN}\gamma_{NS}$ is the resonance frequency, and $\gamma = \gamma_{NN} + \gamma_{SS}$ is the damping rate. RIN can then be expressed in the following form:

$$RIN(w) = \frac{|H(w)|^2}{\bar{S}^2 w_R^4}[r_{SN}^2\langle F_N F_N^*\rangle + 2\gamma_{SN}\gamma_{NN}\langle F_N F_S^*\rangle + (w^2 + \gamma_{NN}^2)\langle F_S F_S^*\rangle] \tag{4.18a}$$

$$\left\langle\delta\widetilde{N}(w)\delta\widetilde{N}^*(w')\right\rangle = \frac{|H(w)|^2}{w_R^4}[r_{NS}^2\langle F_S F_S^*\rangle - 2\gamma_{NS}\gamma_{SS}\langle F_S F_N^*\rangle + (w^2 + \gamma_{SS}^2)\langle F_N F_N^*\rangle] \tag{4.18b}$$

The correlation between the Langevin sources is defined as following [34]:

$$\langle F_i F_i^* \rangle = \text{the rates of particles flow into and out of their reservoirs}$$

$$\langle F_i F_j^* \rangle = -\text{ the rates of particles flow between two reservoirs}$$

Figure **4.6** shows the exchange of particles between carrier and photon. Accordingly, the autocorrelation and cross-correlation between F_S and F_N that leads to RIN can be defined as:

- $\langle F_S F_S^* \rangle \propto$ stimulated emission rate + stimulated absorption rate + photon decay rate + effective spontaneous emission rate
- $\langle F_S F_N^* \rangle = \langle F_N F_S^* \rangle \propto -$ (stimulated emission rate + stimulated absorption rate + spontaneous emission rate)
- $\langle F_N F_N^* \rangle \propto$ pump rate + carrier decay rate + stimulated emission rate + stimulated absorption rate

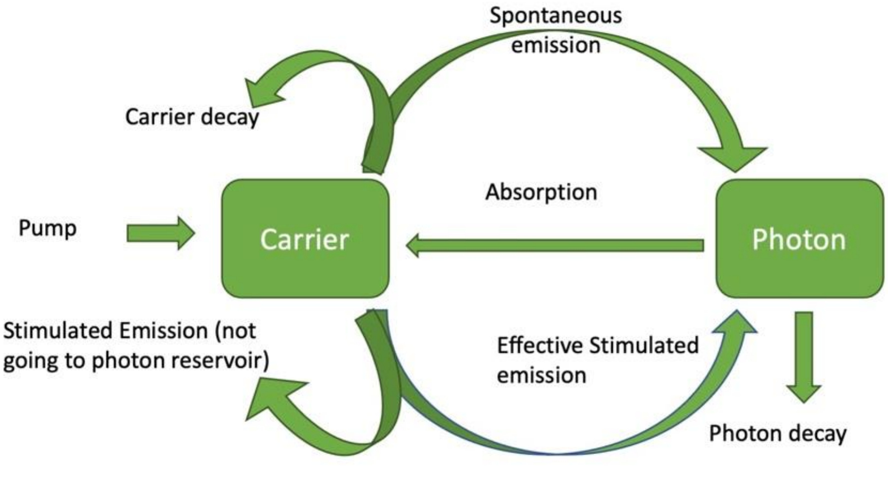

Figure 4.6 The flow of the exchange of carrier and photon reservoirs, and the particles flow into and out of reservoirs.

The dependence of RIN on spontaneous emission rate and pump rate is studied next, as shown in Figure **4.7**(a) and (b), respectively. As pump rate is kept constant, RIN slightly decreases with increasing spontaneous emission factor β. This is because when β increases, the light emission above threshold is slightly higher as RIN is inversely proportional to $\bar{S}^2$, as shown in equation (4.14). The resonance peak is around 20GHz, which comes from the competition between effective carrier lifetime and effective photon lifetime in class-B lasers.

Similarly, when the pumping rate is increased, RIN is decreasing as the steady state photon density is decreasing. The onset of a laser can be read out from the RIN spectrum. When the pump rate approaches the threshold pump rate, the plateau regions of the RIN drop below 140dB/Hz. The relaxation resonance peaks also achieve its climax. When the pump rate is further increased above threshold, RIN further drops, due to the increasing steady-state photon density.

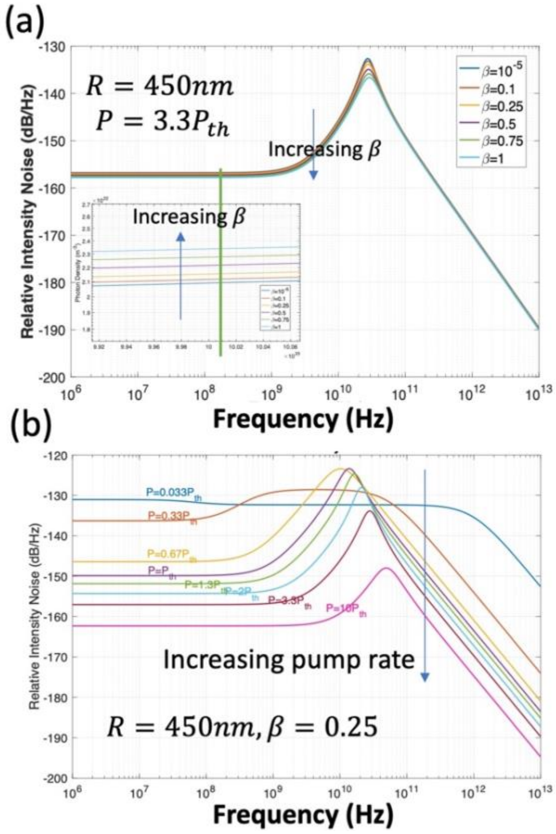

Figure 4.7 Relative intensity noise versus (a) spontaneous emission factor β when the pump rate $P = 3.3P_{th}$ and (b) increasing pump rate when $\beta = 0.25$.

RIN also depends on the physical dimension of a nanolaser. Although the laser rate equations describe only the photon and carrier density, the correlation of the Langevin noise sources depends on both the volume of the active region and the optical mode. The confinement factor Γ also plays an important role in the rate equations. The confinement factor Γ for nanolasers with different radii can be obtained by performing an FEM simulation in COMSOL, that are shown in Figure **4.8**(a)-(e). The RIN for lasers with radii varying from 250nm to 750nm is also presented by Figure **4.8**(f). A decreasing trend of the RIN with increasing radius can be observed.

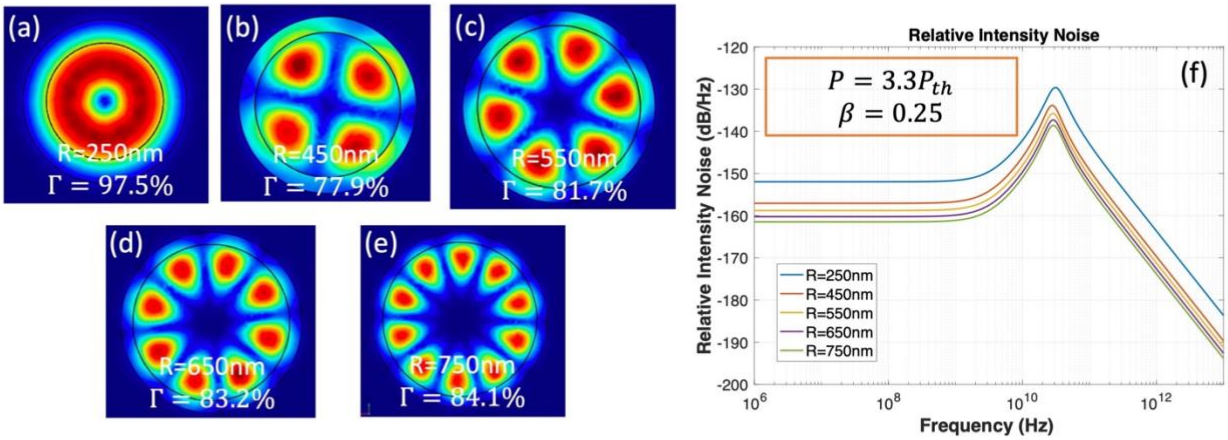

Figure 4.8 (a)-(e) Optical mode profiles and confinement factors of nanolasers with radii 250nm, 450nm, 550nm, 650nm and 750nm, respectively. (f) RIN of nanolasers with increasing radii.

4.4.2 Frequency noise and linewidth broadening

The linewidth broadening effect generated by the relative intensity noise can be calculated by Langevin approach again. Recall that the carrier fluctuation can cause both the real part and the imaginary part to fluctuate and cause the resonance frequency to shift. Other than the carrier fluctuation, phase fluctuation originated from the photons that spontaneously emitted into the lasing mode can also cause the fluctuation of the resonance frequency. This contribution can be considered by adding another Langevin source F_ϕ. We assume F_ϕ is uncorrelated to both carrier noise and photon noise sources. Equation (4.19) is added to the coupled rate equations in equation (4.15) to consider this frequency deviation:

$$\frac{\delta\phi(t)}{dt} = 2\pi\delta v(t) = \frac{\alpha}{2}\Gamma v_g g_0 \delta N(t) + F_\phi(t) \tag{4.19}$$

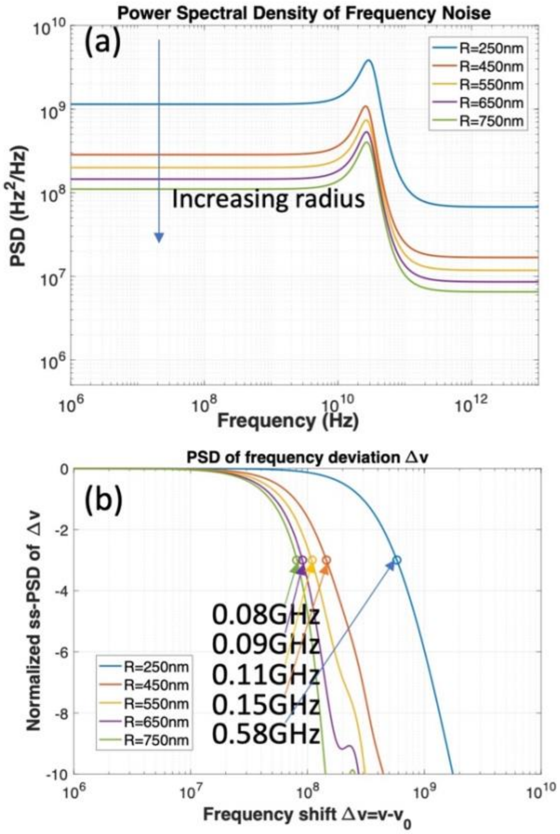

Figure 4.9 (a) PSD of the frequency noise with radii of 250nm, 450nm, 550nm, 650nm and 750nm. (b) PSD of the frequency deviation Δv with increasing radii.

The power spectral density (PSD) for the frequency noise can then be expressed as the sum of the PSD of carrier density fluctuations, which is expressed in equation (4.18b) and the white noise due to the spontaneously emitted photons:

$$S_f(f) = \left(\frac{\alpha}{4\pi}\Gamma v_g g_0\right)^2 \left\langle \delta\widetilde{N}(w)\delta\widetilde{N}^*(w')\right\rangle + \left(\frac{1}{2\pi}\right)^2 \langle \widetilde{F_\phi}\widetilde{F_\phi^*}\rangle \tag{4.20}$$

where $\langle \widetilde{F_\phi}\widetilde{F_\phi^*}\rangle = \langle F_S F_S^*\rangle$. Following the same approach that is applied to calculate the thermal noise induced frequency noise, linewidth broadening caused by the photon and carrier fluctuations can be obtained. Figure **4.9**(a) shows the PSD of the frequency noise with increasing radii. Decreasing frequency noise is seen with increasing radii. The resonance peak comes from the resonance of carrier fluctuations, while the noise floor at high frequencies is obtained due to the white noise.

The corresponding linewidth broadening is shown in Figure **4.9**(b) in a log-log scale. As radius increases from 250nm to 750nm, the linewidth shrinks from twice of 0.58GHz to 80MHz.

4.5 Comparison between thermal and intensity noise

Table 4.4 Linewidth broadening generated by carrier and photon noise

Radius (nm)	250	450	550	650	750
Linewidth (pm)	9.82	2.58	1.78	1.41	1.22

Table 4.5 Linewidth broadening generated by thermal noise

Radius(nm)	250			750		
Temperature (K)	300	77	4	300	77	4
Linewidth (nm)	1.14	0.31	0.0054	0.16	0.04	0.002

The broaden linewidths generated by the thermal and intensity noise are summarized in Table **4.4** and Table **4.5**, respectively. As the radius increases from 250nm to 750nm, the linewidth generated by carrier and photon noise decreases from 9.8pm to 1.22pm while that generated by the thermal noise decreases from 1.14nm to 0.16nm at room temperature.

The more significant finding is that, compared to thermal fundamental thermal fluctuations, the photon and carrier fluctuations can be neglected when evaluating the linewidth broadening in metallo-dielectric nanolasers operating under room temperature.

4.6 Summary

In this chapter, we analytically and numerically investigate the linewidth broadening for a nanolaser caused by the FTF. We adopted a 2-D heat transport model to facilitate solving the stochastic thermal diffusion equation, aiming at finding the solution for the spatially and temporally dependent FTF. For better understanding the implications of the decrease of the mode volume, we derived the frequency noise for two nanolasers with different radii. We observed a higher noise floor and a larger 3-dB thermal noise modulation bandwidth for the nanolaser with smaller radius. We also deduced the thermal linewidth broadening due to FTF and arrived at 1.14nm, 0.31nm and 5.4pm for N-250 and 0.16nm, 0.04nm and 2pm for N-750, both under 300K, 77K and 4K, respectively. This observation corroborates that the ultra-small mode volume of a nanolaser could be detrimental to its spectral properties as it is more prone to fundamental thermal fluctuations. A linear dependence of linewidth broadening on the ambient temperature could be observed for both N-250 and N-750. In this manuscript, we specifically choose a metallo-dielectric nanolaser for calculation. From the comparison between two devices that have different mode volumes, it is reasonable to assume that nanolasers in general will exhibit larger finite linewidths than conventional lasers with larger mode volumes, due to the pronounced FTF in nano-resonaters.

4.7 Acknowledgement

Chapter 4, in part, is a reprint of the material as it appears in S. Jiang, S. H. Pan, S. S. Deka, C.-Y. Fang, Z. Chen, Y. Fainman and A. El Amili, “Impact of Fundamental Temperature Fluctuations on the Frequency Stability of Metallo-Dielectric Nanolasers”, IEEE Journal of Quantum Electronics, vol. 55, no. 5, Oct. 2019. The dissertation author was the primary investigator and author of the publications. Chapter 4 also contains unpublished materials. The dissertation author was the primary author of this part.

Chapter 5 Application-driven dense integration of nanolaser arrays

5.1 Introduction

In most practical applications, a single nanolaser would never operate in isolation but rather in tandem with multiple such devices. Doing so can enable novel applications that would otherwise be infeasible to achieve using an isolated laser. Therefore, the next logical step in the evolution of nanolaser technology is to realize large-scale, dense arrays of nanolasers by leveraging the knowledge gained so far from the plethora of studies on single such emitters.

5.2 Interaction between two nanolasers

Perusing the recent literature on array architectures of nanolasers reveals that based on array size, most studies can be segmented into two categories, i.e., dual nanolasers and nanolaser arrays. The former one can be regarded as a type of unit-cell or building block that can help explain the behaviors observed in larger lattices.

5.2.1 Creation of supermodes

The coupling between two lasers can be introduced in various near-field and far-field manners including evanescent coupling [39, 56, 86, 100, 128-132], leaky wave coupling [63], and mutual injection [133]. With advances in fabrication technology, evanescent coupling can be observed in nanoscale, for example, the dual metallo-dielectric nanocavities shown in the schematic in Figure **5.1**(a) reported by Deka et al [39]. In their design, the distance between the two resonators, represented by d in the schematic, is varied while the modes supported by the system are recorded. For small distance, the increased evanescent coupling between the cavities leads to the formation of two new modes – the anti-bonding supermode (Figure **5.1**(b), middle) and the bonding supermode (Figure **5.1**(b), right). Furthermore, by varying d in discrete steps, split in the eigenmode wavelength (λ), quality factor (Q) and the corresponding lasing threshold (g_{th}) of the supermodes is reported as shown in Figure 5.1(c). The creation of these dissimilar supermodes due to evanescent coupling has also been reported in other material systems such as photonic crystals as depicted in Figure **5.1**(d) reported by Hamel et al [56]. When pumped equally, their system supports bonding and anti-bonding supermodes with the latter becoming the dominant lasing mode at higher pump powers (Figure **5.1**(e)). Therefore, the formation of bonding and anti-bonding supermodes is one of the most basic phenomena to occur due to increased evanescent coupling between nanolasers.

Parto et al. demonstrate the existence of either ferromagnetic (FM) or anti-ferromagnetic (AF) coupling between the constituent elements of the lattice that depending on the size of the metallic nanodisks [134]. These FM and AF couplings arise due to the interaction between the vectorial electromagnetic modes supported by the nanocavities which exchange spin Hamiltonians like in magnetic materials [134, 135]. These recent results can help pave the path towards achieving ultracompact, on-chip photonic platforms that implement spin Hamiltonians for solving complex optimization problems [135].

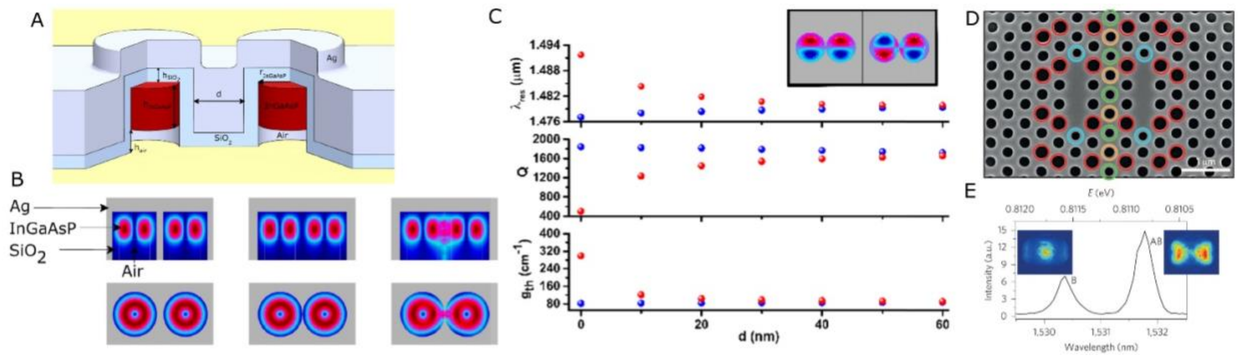

Figure 5.1 Supermode creation in dual nanolaser systems. (a) Two coupled metallo-dielectric nanolasers where the distance between cavities is represented by *d*. (b) Electric field intensity profiles across the side (top row) and top (bottom row) cross-sections of the nanolaser system shown in (A) for two independent modes (left), (middle) and bonding supermodes (right). (c) Eigenmode wavelengths (λ), quality-factors (Q) and gain thresholds (g_{th}) for the two modes supported by the dual nanolaser system at varying *d*. Inset: electric field distributions of the anti-bonding (left) and bonding (right) supermodes. (a),(b) and (c) reprinted from [39]. (d) Two coupled photonic crystal nanolasers and (e) the bonding (B, left peak) and anti-bonding (AB, right peak) modes supported in this design. (d) and (e) adapted and reprinted from [56].

5.2.2 Analysis of nonlinear dynamics

Besides supermodes creation, the coupling between two lasers can also produce rich nonlinear dynamics. Specifically, just as mentioned in Chapter 2, for the case of coupled nanolasers, a multitude of dynamical regimes including stable phase locking, periodic intensity oscillations, as well as chaotic fluctuations can be achieved that can help enable a wide variety of applications. Besides the examples that utilize stable phase-locking given in Chapter 2, the high frequency periodic oscillations exhibited by a dual nanolaser system are also of interest for any applications requiring high speeds. Adams et al. theoretically predict such periodic oscillations to occur outside the stability region for two laterally coupled nanowire lasers [59]. The frequency of these oscillations as a function of both the separation between the nanolasers and the pumping rate is shown in Figure **5.2**. It can be clearly observed from the plot that ultra-high frequencies on the order of at least 100 GHz can be reached when the separation is reduced to ~300 nm or so. Moreover, the oscillation frequency increases for larger pumping rates.

Above-mentioned studies highlight the importance of investigating the dynamics of coupled nanolasers. Identifying the stable, oscillatory, and chaotic regimes as a function of varying control parameters allows the coupled system to exhibit the desired behavior for the application demanded. Theoretical analyses can also shed light on bifurcations that can arise due to coupling. Such bifurcations are especially significant as they can lead to switching of optical modes as elaborated on in the next section.

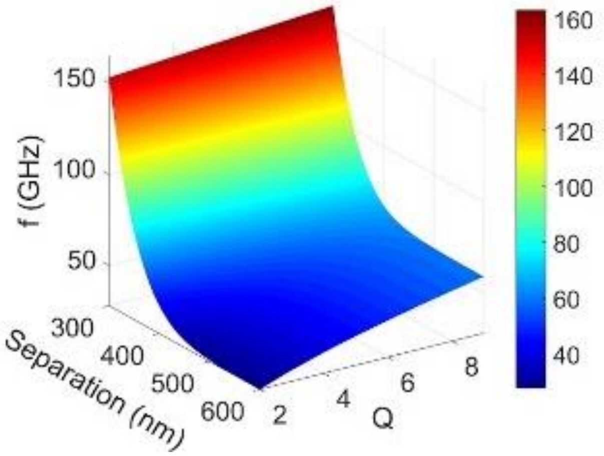

Figure 5.2 Periodic oscillations for two evanescently coupled nanowires as a function of separation between lasers and pumping rate (Q). Oscillations can reach over 100 GHz. Reprinted from [59].

5.2.3 Mode-selection and switching

What is especially advantageous for nanoscale systems compared to their micron-sized counterparts, is their increased sensitivity to small perturbations induced by nuanced changes in the geometry or in the pumping scheme. Haddadi et al. show in their study how varying the size of the middle row of holes in their coupled photonic crystal nanolaser structure can enable them to control the coupling behavior [57]. In other words, by engineering the barrier between the two cavities (Figure **5.3**(a)), both the amount of wavelength splitting as well as the excited state mode can be selected, as shown in Figure **5.3**(b). Additionally, the authors report that the branches on either side of the dip in $|\Delta\lambda|$ correspond to a flip in the parity of the bonding mode. To be more accurate, to the left of the dip, the bonding mode becomes the excited state whereas to the right, it remains the ground state mode [57]. Finally, increasing the size of the cavity results in a monotonic shift of the point where the parity flip of the bonding mode occurs. Efforts to select the ground state mode have also been reported in other studies, albeit with microcavities [136, 137].

In a later work based on the same platform, Marconi et al. demonstrate a mode switching behavior from the blue-detuned bonding mode to the red-detuned anti-bonding mode as they increase the optical pumping to their coupled photonic crystal nanolaser system [58], as depicted in Figure **5.3**(c). The mechanism behind the switching is attributed to the asymmetric stimulated light scattering induced by carrier oscillations which manifests itself through a Hopf bifurcation.

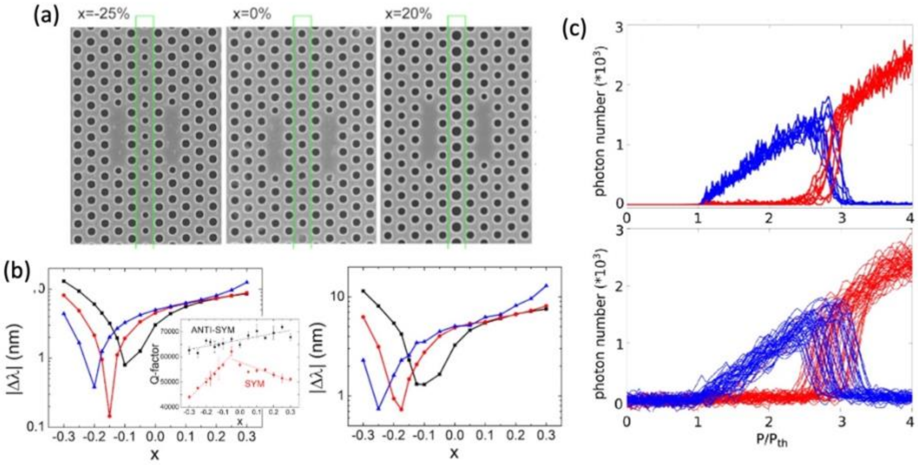

Figure 5.3 (A) Barrier engineering in photonic crystal nanolasers by changing size of the middle row of holes. (B) Absolute value of wavelength difference between B and AB modes - $|\Delta\lambda|$ -- vs. size of the middle row of holes. Simulations (left) and experiment (right). Adapted from [57]. (C) Simulated (top) and experimental (bottom) results showing switching from B (blue) to AB (red) mode due to increased pump powers in two coupled photonic crystal nanolasers. Adapted from [58].

As evident from these results, the ability to engineer coupled modes as well as switch between them is of interest not only for the underlying physics involved but also for the potential applications. For instance, measuring the second order correlation function at zero delay - $g^2(0)$ - yields a value greater than 2 for a bonding supermode indicating the superthermal nature of light emitted from this mode [138]. Therefore, systems where the mode selection is enabled are ideal testbeds for important studies concerning quantum and nonlinear optics, out-of-equilibrium thermodynamics, quantum correlation devices and engineering of superthermal sources [56, 58, 138]. Mode switching devices with the ability to affect the transition between optical modes depending on the current state, as was explained for the broken parity states, can be said to exhibit memory and can therefore, be potentially used as ultracompact logic gates or optical flip flops [56].

5.2.4 Crosstalk isolation

Although coupling between two nanolasers can yield complex dynamical phenomena rich in physics, certain applications might require the independent functioning of the emitters even when placed in close proximity. Biological sensing and imaging are two such areas where maintaining isolation between the emission of the two cavities is imperative. This implies that each nanocavity can be pumped and modulated without influencing the behavior of its neighbor. In cavities that share a common cladding, the conventional techniques to prevent coupling are difficult to implement since any alterations made to one cavity will be transmitted to its neighbor via the shared cladding, which is the case for metallo-dielectric nanolasers. In such a scenario, a viable way to curb the evanescent interaction of the electromagnetic fields is to introduce a resonance mismatch by designing one cavity to be slightly larger than its neighbor. By doing so, Deka et al. demonstrated that by altering the radius of one cavity to be 5% larger than its neighbor, the degree of splitting in the eigenmode frequency and optical loss - a characteristic signature of coupling - can be minimized [39], as shown in Figure **5.4**(a).

Another geometry-based technique that can be implemented to mitigate coupling in metallo-dielectric nanolasers is to increase the cavity radii in order to exploit the higher-order cavity modes with stronger optical confinement and reduced evanescent interaction. Pan et al. [40] demonstrate this behavior for the same dual metallo-dielectric nanolaser system first presented in [39]. As shown in Figure **5.4**(b), as the radii of the nanocavities are increased, the split in their losses diminishes due to reduced coupling.

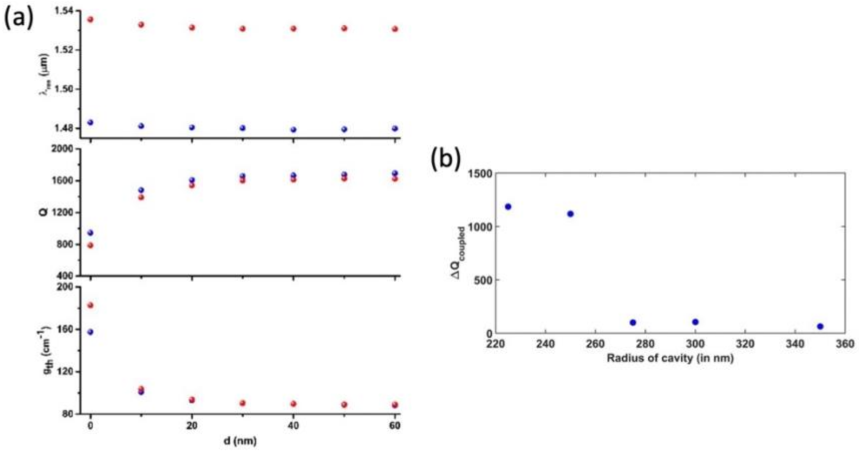

Figure 5.4 Crosstalk isolation techniques. (A) Eigenmode wavelengths (λ), quality-factors (Q) and gain thresholds (g_{th}) for the two modes supported in two unequal sized metallo-dielectric cavities where one is 5% larger in radius. Adapted from [39]. (B) Difference in Q for the coupled mode – $\Delta Q_{coupled}$ as a function of radii of the cavities. Reprinted from [40].

5.3 Nanolaser arrays

Scaling up design to allow individual light sources to work in conjunction in an array format falls into the natural roadmap of the nanolaser technology [2, 139]. It is important to emphasize here, however, that not all nanolaser arrays rely on the same operating principles. The main distinction to be made is between uncoupled and coupled arrays. Uncoupled arrays comprise of individual nanolasers that function independently and do not interact with their nearest neighbors. In direct contrast, coupled arrays, as the name suggests, rely on coupling of some form involving the constituent resonators comprising the system. This may be exhibited either in terms of evanescent coupling between the nanocavities or excitonic state-plasmonic surface lattice resonance coupling. Owing to their clear disparity, coupled and uncoupled arrays are each appropriate for different types of applications.

5.3.1 Uncoupled arrays

A majority of sensing and imaging applications fall into this category as they rely on recording the wavelength shift of each nanolaser due to changes in the refractive index environment.

One such study authored by Hachuda et al. demonstrates the detection of protein in the form of streptavidin (SA) by using a 16-element 2-D photonic crystal nanolaser array as shown in Figure **5.5**(a) [51]. The independence is maintained by optically pumping each one separately to record the red-shift in emission wavelength - $\Delta\lambda$ – caused by the adsorption of protein in each individual nanolaser. The overall wavelength alterations for all 16 devices are then statistically evaluated using averaging and confidence intervals. Figure **5.5**(b) portrays the results for $\Delta\lambda$ for each element in the array when impure solutions containing the protein SA are exposed to the nanolaser array. With water serving as the control (blue), it can be clearly observed that the array can distinguish between a sample containing SA (red) and those without it (black) based on the shift in emission wavelengths. Based on the same principle of using $\Delta\lambda$ from individual lasers, Abe et al. demonstrate imaging of living cells using uncoupled arrays comprising of 21x21 = 441 photonic crystal nanolasers [52]. In their study, the crosstalk isolation between individual array constituents is ensured by designing an offset in radii for all neighboring lasers.

Besides sensing and imaging, uncoupled lasing arrays can also be purposed to demonstrate cryptography. By creating organic molecule-based laser arrays with random sizes as depicted in Figure **5.5**(c) and using them in conjunction with distinct organic solutions, Feng et al. demonstrate the possibility of creating non-deterministic cryptographic primitives [54]. The molecules exhibit dual wavelength lasing at either 660 nm or 720 nm or both depending on the length of the cavity, that represents the quaternary bits. The cryptographic sequence from the arrays is obtained by pumping each nanolaser separately and then scanning the array to get the emission spectra from all devices, as depicted in Figure **5.5**(d). Encoding as double binary bits makes it possible to generate up to 2048 binary bits.

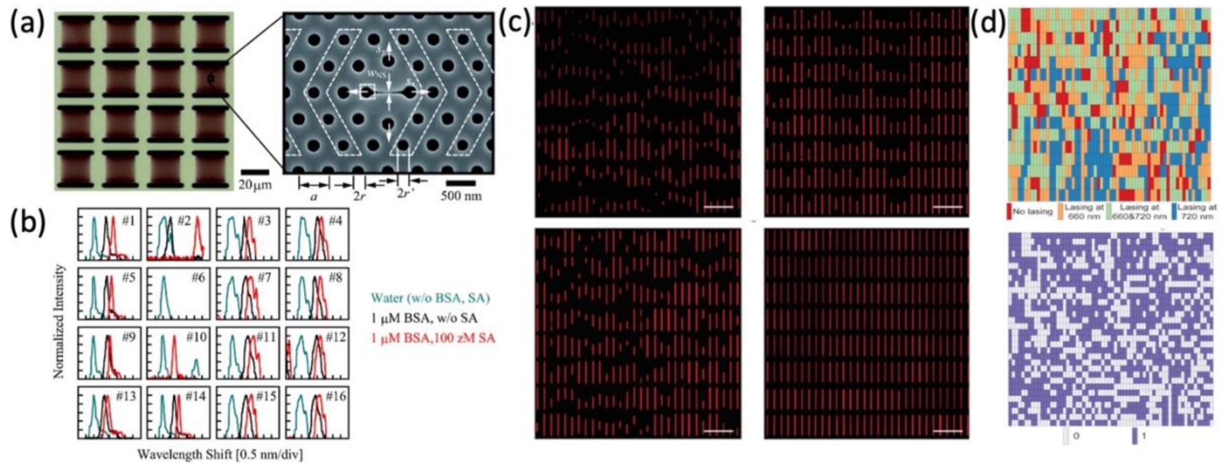

Figure 5.5 Biological sensing of proteins. (a) Schematic of 16-element photonic crystal uncoupled array (left) and SEM image of nanoslot-incorporated single laser (right). (b) Normalized intensity showing wavelength shift for all 16 elements under varying solutions. Water serves as the control. Adapted and reprinted from [51]. (c) Organic nanolaser arrays with stochastic size distribution dependent on the organic solution used during fabrication. Scale bar: 100 μm. (d) Cryptographic sequence generated by treating emission states as quaternary bits (left) and double binary bits (right). Adapted and reprinted from [54].

The studies elaborated on above are only a fraction of the multiple works demonstrating how uncoupled arrays can achieve unique applications. Whether used for refractive index sensing, imaging or developing next generation, all-photonic cryptographic primitives, maintaining the independence of each nanolaser in the array is of vital importance for these applications [52, 54, 105]. Additionally, nanolaser arrays offer distinct advantages for some of these applications such as higher sensitivity compared to Raman-based sensors as well as a label-free imaging method. The use of such arrays can also be extended to telecommunications, lab-on-a-chip applications, spectroscopy, and parallel detection [140-142].

5.3.2 Coupled arrays

Contrary to independent nanolaser operation in uncoupled arrays, coupling can give rise to different types of nonlinear dynamics and in general, increases the complexity of the physical mechanisms involved in the process, which is worth investigating effort. Coupling in arrays has been demonstrated in a variety of manners including bound state in-continuum (BIC) mode coupling [143, 144], interferential coupling [145], transverse-mode coupling [146], surface plasmon-based coupling [147-154] and evanescent coupling [36, 134, 155-158]. We will focus this review mainly on the latter two forms since a majority of the literature on nanolaser arrays was found to rely primarily on these two mechanisms.

It is important to note here that plasmon-based coupling is usually reported to affect properties of the emission such as directionality and wavelength. For most implementations of coupled arrays based on this physics, a lattice of metal nanoparticles creates the localized surface plasmon (LSP) resonance while some form of liquid dye medium, in which the lattice is immersed, serves as the gain or exciton states (ES). This type of hybrid resonance is referred to as the ES-LSP. Though some aspects of the lasing phenomena are yet to be fully understood, the general consensus is that it occurs due to the excited-state molecules being stimulated to transfer energy to the lattice plasmons of the same frequency, phase and polarization [149, 159]. In other words, the localized near-field of the plasmonic particles comprising the array can stimulate the gain regions surrounding the particles to emit stimulated light at a wavelength that matches that of the lattice plasmon mode. With stimulated emission from the dye-gain and a cavity-like resonance provided by the lattice plasmon, lasing action can thus be obtained. It is important to note here that the reason for the tight confinement of light in these 2D metallic nanoparticle arrays is due to the strong interaction between the LSP resonances of individual particles and the far-field diffractive modes that satisfy the Bragg conditions of the array [160].

In comparison, evanescently coupled arrays can yield high powers and even generate states with orbital angular momentum (OAM) through the interplay between the lattice geometry and the modes of the individual lasers. Unlike for ES-LSP coupling where the resonance structure and gain are disparate media, for evanescent interactions, the active medium (usually comprised of III-V semiconductors) is not external to the resonant structure; instead, it is a part of the cavity that supports the electromagnetic mode.

5.3.2.1 Beam directionality

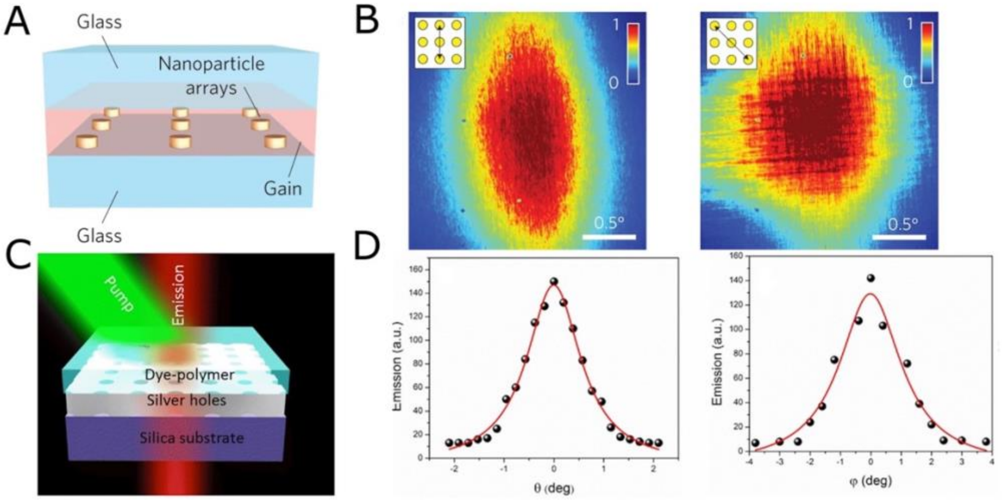

Figure 5.6 Directional emission. (a) Schematic of metal nanoparticles embedded in dye-gain and sandwiched between two glass slides. (b) Far-field emission patterns of the nanolaser array in (A) for pump incidence angle parallel to (left) and 45° (right) to the lattice direction. Adapted and reprinted from [149]. (c) Schematic of Ag film with nanoholes immersed in dye-polymer gain. (d) Emission intensity from the coupled nanolaser array in (C) as the detector angle is varied along the horizontal (left) and vertical (right) directions. Adapted and reprinted from [150].

Ability to control the direction of emission is of notable significance for wireless communications and nanoscale biosensors among other applications. Zhou et al. has demonstrated the modification of laser emission angle by altering the angle and/or polarization of the input optical pump [149]. When the authors tune the pump angle to either be parallel to or 45° to the lattice direction (shown in Figure **5.6**(a)), certain nanoparticles exhibit increased localizations of the electromagnetic mode, which in turn, affects the overall direction of the beam emitted from the array, as shown in Figure **5.6**(b).

Similarly, Meng et al. also demonstrate highly directional lasing from their coupled spaser array [150], consisted of an Ag film with nanometer-sized holes covered with an organic dye-polymer gain as shown in Figure **5.6**(c). Instead of altering the pump incidence angle, however, the detector itself is rotated to measure the directionality of the array output emission, yielding the results in Figure **5.6**(d).

5.3.2.2 Tunable emission wavelength

Control over the emission wavelength of nanoscale light sources is desirable for dense wavelength division multiplexing (WDM) applications at a chip-scale level [161], as well as in lidar and imaging/sensing systems. Incidence angle and polarization of the pump can play a determining role in this respect as well. In one study, Knudson et al. create a rhombohedral Al nanoparticle array immersed in dye-gain [151]. Depending on the in-plane pump polarization, the ES-LSP based mechanism leads to the array emitting at either 513 nm, 570 nm or both. This tuning of the output light from the array is described via Figure **5.7**(a), which show the experimental streak camera images and numerically simulated spectra of the structure used in the study, respectively

Besides angle-resolved experiments to select the peak emission wavelength, altering the temperature is another technique that can be leveraged to attain the same goal. This may be accomplished via two main mechanisms: 1) modifying the stoichiometry of the gain material based on thermal annealing, and 2) temperature-induced red-shift of the bandgap commonly referred to as the Varshni shift [162]. Huang et al. demonstrate a wavelength-tunable device based on the former principle by combining an Au/SiO_2 grating resonance with lead halide perovskite gain material [154]. By thermally annealing their structure in a CH_3NH_3Br environment, the hybrid plasmonic mode in which the coupled nanolaser array operates in is observed to be blue-shifted in emission wavelength as shown in Figure **5.7**(b).

The Varshni-shift method does not require any specific chemical environment to be implemented and the alteration in the emission wavelength is always a red-shift irrespective of the material. The pseudowedge plasmonic nanolaser array based on ZnO nanowire placed on an Ag grating presented by Chou et al. exhibits such a red shift in the emission wavelength by increasing the operating temperature from 77 K to 220 K, as shown in Figure **5.7**(b) [155].

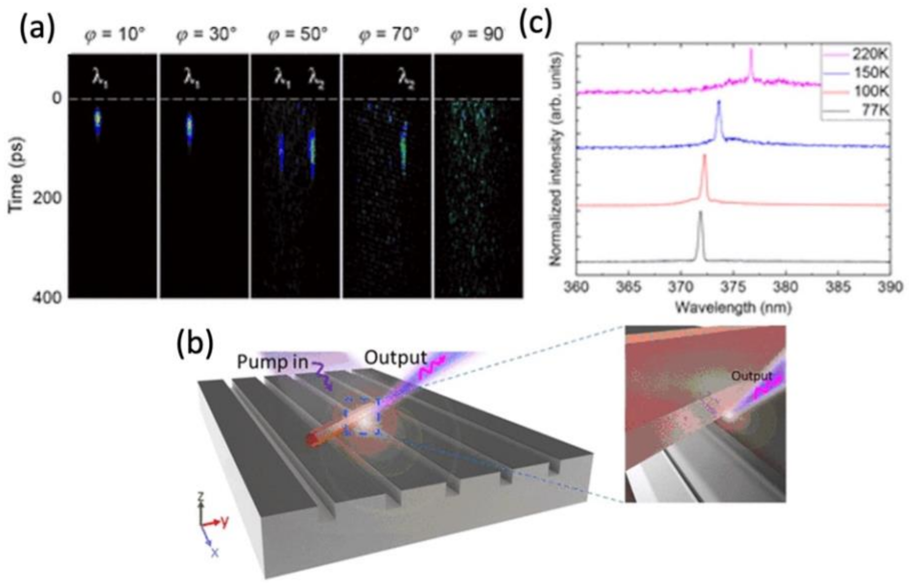

Figure 5.7 Tuning peak wavelength of emission. (a) Experimental streak camera images of nanolaser array as the in-plane pump polarization is altered. Reprinted from [151]. (b) Schematic of pseudowedge nanolaser array with ZnO nanowire placed on top of Ag grating. (c) Varshni red-shift of emission wavelength as ambient temperature is increased. (b) and (c) adapted and reprinted from [155].

5.3.2.3 Single and multimode switching

The studies on coupled arrays mentioned thus far portray instances of single-mode lasing. However, some specific cases such as multimode fiber-based WDM sources and on-chip multiplexing in photonic devices may also benefit from multimodal operation instead [163]. Wang et al. [147] have demonstrated switching between single- and multi-modes based on ES-LSP nanolaser arrays with two distinct types of lattices – a single lattice where the individual nanoparticles collectively contribute to the resonance and a superlattice where several single lattices combine to give rise to multiple band-edge states (Figure **5.8**(a)). The new altered superlattice as illustrated in Figure **5.8**(b) combines the functionality of the two lattices and leads to single and multi-mode emission based on the polarization and direction of the pump beam.

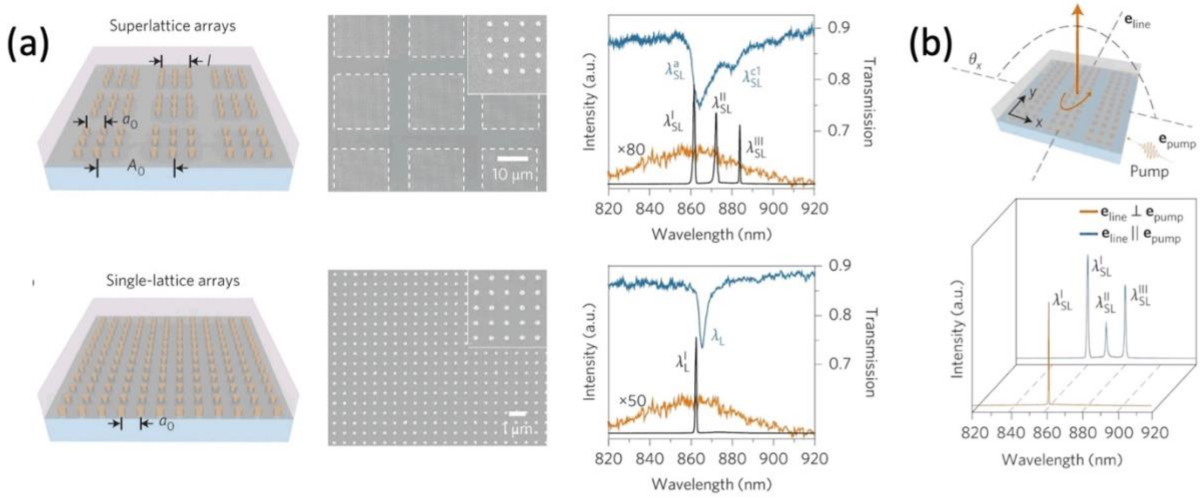

Figure 5.8 Switching between single and multi-modal operation. (A) Schematic of superlattice and single lattice arrays (left), their SEM images (middle) and their corresponding spectra (right). The superlattice exhibits multi-modal lasing (top, right) whereas the single lattice demonstrates single mode lasing (bottom, left) as evidenced by the lasing spectra shown as black solid curves in both figures. (B) Schematic of altered superlattice (top) and its output lasing spectra (bottom). If the pump direction is perpendicular to the lattice, the array operates in single mode lasing regime whereas when the pump is parallel to the lattice direction, multi-modal lasing is observed. Adapted and reprinted from [147].

5.3.2.4 Higher output power

Owing to their compact size, nanolasers inherently possess low output power [164]. However, if the lasers are designed and placed in close proximity such that the emission of a multitude of such lasers is coherently combined, a significantly higher output power can be obtained, which can be employed in far-field applications, such as optical interconnects [2] and beam synthesis [109].

In their study based on a N=81 element evanescently coupled photonic crystal nanolaser array, shown in Figure **5.9**(a), Altug et al. are able to observe a ~100 times higher output power and a ~20-fold increase in the differential quantum efficiency (DQE) with their coupled array than with a single emitter [36]. The DQE here refers to the slope of the LL curve above threshold and is extracted from the experimental results depicted in Figure **5.9**(b).

Similarly, increased output power has also been reported by Hayenga et al [156], where the overall power emitted by a 7-element metallic nanodisk array arranged in a hexagonal pattern (Figure **5.9**(c)) shows a 35-fold increase in the output power and a 5-times slop efficiency compared to a single nanolaser, as shown in Figure **5.9**(d). These results emphasize the ability to coherently combine the emission of multiple nanolasers to yield higher powers.

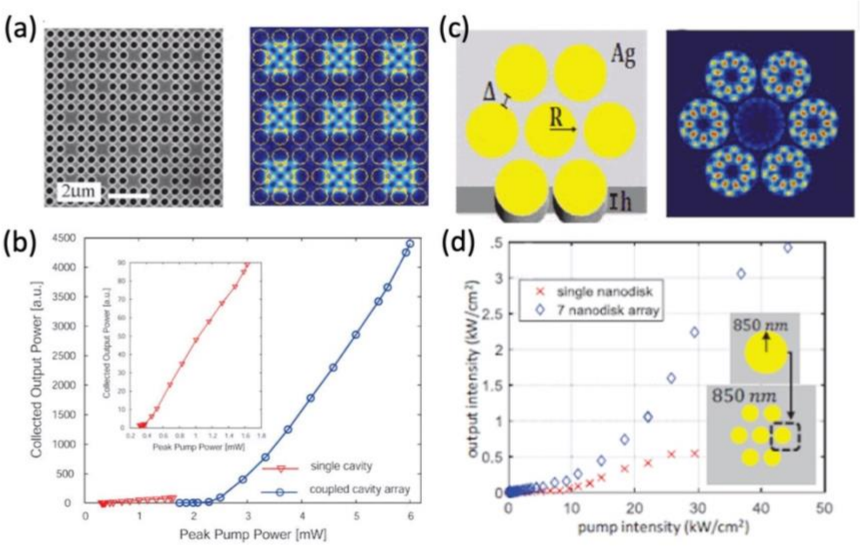

Figure 5.9 Higher output power. (a) SEM image of photonic crystal nanolaser array (left) and simulation of the modes supported by the system (right). (b) Output power of coupled cavity array shown in (a) compared to that of a single cavity. Inset: Magnified version of curve for single cavity. Adapted and reprinted from [36]. (c) Schematic of 7 hexagonally designed metal-coated nanodisk lasers (left) and simulation of the mode structure supported (right). (d) Output intensity of one nanodisk vs. array as pump intensity is increased. Reprinted from [156].

5.4 Summary

To conclude, recent progress on the development of array architectures of nanolasers is reviewed in this article. The focus was on valuable attributes realized due to unique array designs and the underlying physics that may help enable real-world applications such as biological sensing, imaging and on-chip communications. A distinction was made between an array size of just two nanolasers and larger arrays. The former can not only serve as a testbed to understand the fundamental physics and enable interesting applications (for example optical flip flops), but also as a building block that can aid in comprehension of larger-lattice behavior. Larger arrays themselves can also be distinguished depending on whether their constituent elements function independently from one another or demonstrate coupling of some form. Uncoupled arrays are more intuitive to understand and suitable for applications such as imaging, biosensing and even cryptography. On the other hand, although coupling in nanolaser arrays can create complex dynamics, control over many aspects of the emission behavior such as beam directionality and mode switching are afforded.

5.5 Acknowledgement

Chapter 5, in part, is a reprint of the material as it appears in S. S. Deka, S. Jiang, S. H. Pan and Y. Fainman, “Nanolaser arrays: toward application-driven dense integration”, *Nanophotonics*, vol. 10, no. 1, Jan. 2021. The dissertation author contributed towards the literature review and manuscript writing of this work.

Chapter 6 Conclusion and outlook

In summary, this dissertation focused on the investigation of phase-locking stability of dual coupled nanolasers and the intrinsic noise on the linewidth broadening effect of individual nanolasers. We also show experimental demonstration of mode selection in coupled lasers based on the theoretical stability analysis. These results show significance in extending the research of dual nanolasers to large size nanolaser arrays. Next, we will elaborate on the results of this dissertation and provide some future directions for nanolaser research.

6.1 Summary of the work

In Chapter 2, we investigated the stability of phase-locking in laterally coupled semiconductor lasers with respect to the change of multiple control parameters. We employed the bifurcation analysis and applied it onto coupled laser rate equations that govern the electric field, carrier density and phase difference of two coupled lasers. The coupling between the two elements is phenomenologically introduced into the equations through a complex value $i\kappa + \gamma$. We attained different dynamical regimes, including stable phase-locking, periodic oscillations, period doubling, and chaos by varying the coupling coefficients. Previous studies overlooked the spontaneous emission factor β, as β is negligible in conventional semiconductor lasers. In nanolasers, however,

β can be larger than 0.01, or even approach 1. Therefore, in this chapter, we have investigated the dependence of phase-locking stability on β factor. We have considered multiple realistic scenarios, including purely imaginary coupling coefficient, varying pump rates, non-zero resonance frequency detuning, and complex coupling coefficients. In all case studied, we have observed that an increasing β leads to enhanced phase-locking stability. Such results imply that nanolasers with intrinsic high β factor are ideal candidates to be applied in phase-locked laser arrays for various applications such as high-power generation.

In Chapter 3, we have demonstrated coupled metallo-dielectric nanolasers that can operate in either the in-phase or out-of-phase mode by varying the geometry of the coupling bridge in between the two lasers. For application requires high power, in-phase locking between adjacent lasers is highly desirable. Although evanescently coupled nanolasers are easier to fabricate and can be densely integrated on a chip, they have coupling coefficients that lead to the two cavities always operate in the out-of-phase mode. In photonic crystal lasers, this limitation can be broken by the barrier engineering, where the change of the radii of center row of holes leads to desirable mode selection. Similarly, in this work, we have incorporated a coupling bridge in between the two lasers. By changing the geometry of the bridge, the coupling coefficients can be modified such that a target mode can be supported by the structure. We have fabricated devices with different bridge lengths. The first step is to confirm the lasing action of these devices by measuring the L-L curves, where the kinks in these curves are clear indications of the onset of lasing. Next, we have identified the in-phase and out-of-phase operating modes by measuring both the near-field and far-field of these devices. The successful demonstration of mode selection in nanoscale paves the way for building nanolaser arrays for beam forming applications, as the dual nanolasers serve as building blocks for the dense arrays.

In Chapter 4, we have theoretically investigated the linewidth broadening effect caused by the intrinsic thermal fluctuation and intensity noise. Broad linewidths on the order of 1nm have been observed in nanolasers with various designs. To explain this experimental observation, we have looked into multiple noise terms, including thermal noise, intensity noise, and phase noise. Specifically, the thermal fluctuation is very pronounced for small optical cavities, which can cause the change in the refractive index of the nanocavities due to thermo-refractive effect. This effect results in the fluctuation of the optical path length and leads to the resonance frequency to shift around and generate a finite linewidth. In this work, we have employed Langevin method to rigorously calculate the effect of thermal fluctuations on the finite linewidth and considered two devices with different radii. We have observed that the decrease in the nanolaser radius and the increase in the ambient temperature are the two main factors that leads to linewidth broadening effect. Specifically, for a metallo-dielectric nanolaser with a radius of 250nm, the linewidth generated by thermal fluctuations at room temperature is 1.14nm, on the same order as the experimental results reported in literatures. We have also studied linewidth generated by intensity noise and phase noise, which is much smaller than that generated by thermal fluctuations.

In Chapter 5, we have reviewed some of the research of nanolasers towards the dense integration driven by various applications ranging from telecommunication to bioimaging/biosensing. We have started with work on dual nanolasers, which are the building block on nanolaser arrays, with various functionalities, including supermodes generation, nonlinear dynamics, mode selection and switching and crosstalk isolation. Next, we summarized research effort in nanolaser arrays and categorized them into two kinds: uncoupled and coupled arrays. For the uncoupled arrays, the functionality is achieved by assuring the independence between adjacent elements. They have found applications in biological sensing, live-cell imaging, and optical cryptography. Coupled arrays that employ either surface plasmon coupling or evanescent coupling have shown control of beam directionality, tunable emission wavelength, single and multimode switching, high-power generation, and orbital angular momentum generation.

In conclusion, the stability of coupled semiconductor nanolaser has been theoretically investigated, and enhanced performance with increasing β has been observed. This, in together with the demonstration of mode selection in bridge-coupled nanolasers truly states the advantages and possibility of building nanolaser arrays with ultra-dense integration and low power consumption for future applications in Lidar, sensing, and telecommunication systems. However, to successfully build nanolaser arrays with desired functionalities, some major breakthroughs are needed, that will be discussed in the next section.

6.2 Future directions

One of the most important research goals of nanolasers to further improve the device-level performance, including their linewidths, output power, wavelength tunability, and modulation bandwidth, that are valuable merits for on-chip high-resolution sensing/imaging and communication applications. Specifically, the narrow linewidth, broadband tunable wavelengths and fast modulation of laser sources enable large amount of data to be coded in the wavelength division multiplexing (WDM) systems for the growing demand of data transmission. While the leading commercial semiconductors such as external cavity lasers and distributed feedback (DFB) lasers can achieve below-KHz linewidths [165-167], nanolasers still have broad linewidths on the order of 1GHz to 100GHz [13, 14, 23-25, 27-29, 36]. Theoretically, the linewidth can be significantly reduced if the lasers are pumped far above threshold. However, this method is constrained in nanolasers as the heating issue with increasing pumping is more prominent in nanoscale cavities [125]. Kim et al. has demonstrated a buried-heterostructure photonic crystal nanolaser with a linewidth of 143.5MHz, which is far narrower than most of the nanolasers reported so far [168]. The narrow linewidth is obtained by using InGaAs/InGaAsP MQWs on InP slab structure, where the InP slab serves as an efficient heat sink to alleviate the heating issue, and the strong confinement in the gain region can lead to an extremely low lasing threshold below $10\mu W$. Therefore, the photonic crystal nanolaser can operate far above the threshold with reduced heating problems, which is suitable for use as integrated narrow-linewidth lasers. This work suggests that proper heat dissipation design can significantly improve the linewidth performance of nanolasers. More research effort in designing nanolasers with less heat generation at first place other than the incorporation of tunnel junction is also essential [125]. The study on linewidth broadening induced by the thermal noise also suggests that by designing nanocavities with materials that have better heat capacity and lower junction temperature, the finite linewidth of the nanolaser can be effectively reduced for application requires better resolution or more wavelength channels.

Lasers sources with wavelength tunability are crucial for many applications such as Lidar systems, optical coherence tomography (OCT), and beam steering [169]. Static wavelength tuning can be easily obtained by changing the bandgap of the materials or by modifying the geometry of the nano-resonators [170-176]. For many applications, dynamic tuning of the wavelength is desired, which can be tuned by the operating environment including voltages, temperature, pressure and strain [98, 162, 177, 178]. For conventional semiconductor lasers, such real-time tunability has been achieved based on the Vernier effect, where the effective refractive indexes of the two Bragg grating reflectors or ring resonators can be tuned by thermal-refractive effect [179]. However, such method is limited in nanolasers due to their ultra-compact mode volume and their sensitivity to fabrication imperfections. While the tunable metallo-dielectric nanolasers have been demonstrated by applying voltages across the multiple quantum wells based on the quantum confined stark effect [44], the simultaneous result in intensity drop will increase the pumping complexity if a large number of nanolasers are to be employed. Besides, the wavelength tuning range of 8.35nm is insufficient for many applications. Further research on demonstrating nanolasers with larger wavelength tuning range with no effect on intensity is required for next-generation on-chip compact and efficient optical communications systems.

To make nanolasers fully functional as on-chip light sources, their integration with the other photonic devices, such as waveguides, modulators and photodetectors on the PIC is required. The output beam of the nanolasers needs to be efficiency extracted and coupled into either a Si waveguide in a silicon-on-insulator platform [180] or a InP waveguide in III-V materials [181] for telecommunication applications. While the integration of III-V active components on Si chips remains an on-going academic and industrial research, the utilization of nanolasers further complicates this issue due to the low output power of nanolasers and the current nanofabrication limitations.

One possible solution is to use the monolithically grown III-V lasers on Si [182], but the high defect density in the heteroepitaxial material originated from the large lattice mismatch of III-V and Si materials. This threading delocalization significantly reduces the laser lifetime, increases the threshold current injection, and degrades the performance of the devices. While most of the research effort focuses on reducing the delocalization in the heteroepitaxial layers, Li et al suggests that if the laser dimension is reduced below the average spacing between two adjacent defects, the device can be made defect free with a higher possibility [183]. In their work, they report a plasmonic laser based on GaAs MQWs with sub-diffraction limited dimensions, optical power on the milliwatt range, and ~100GHz modulation bandwidth above threshold injection currents, that are sufficient for optical transceivers and receivers. The devices show efficient waveguide coupling to the Si optical waveguide and are fully CMOS compatible.

The other solution utilizes the heterogeneous integration of III-V on Si. The fruitful results of microscale lasers integrated on SOI reported by John Bower's group in UC Santa Barbara [184-187] have set a steppingstone for the development of nanolasers on Si. For this method, the challenge lines in the efficient coupling of a III-V nanolaser to the SOI chip. Kim et al has presented that by controlling the SiO_2 cladding thickness in the both x- and y-directions, the effective refractive index and the field distribution of the cavity mode can be engineered. Moreover, a quality factor as high as 1700 can be obtained for a metal-clad nanolaser with a mode volume of $0.28(\lambda/n)^3$ [188]. The coupling efficiency can achieve >75% by using asymmetric cladding thickness. Experimental demonstration of a CW electrically pumped 1D photonic crystal nanolaser wafer-bonded to a Si waveguide has been reported by Crosnier et al [91]. The hybrid structure has a footprint of $100\mu m^2$, a record wall-plug efficiency of 14%, a differential efficiency of 35%, and output power as high as $95\mu W$. Although the threshold hold current appears to be 20 times larger than that of the best photonic crystal lasers reported, this work paves the way for hybrid lasers in the construction of next-generation optical interconnects. For electrically pumped metallo-dielectric nanolasers, their integration with SOI wafer falls naturally in the roadmap, with the challenge in coupling sufficient optical power for the other on-chip photonic assemblies.

Appendix A Normalization and the linear analysis of coupled rate equations

Before we perform the small signal analysis, the different bifurcation points need to be introduced and identified. The saddle-node bifurcation indicates the collision and disappearance of two equilibria. A pitchfork bifurcation occurs when the system transitions from one fixed point to three fixed points. In both these types of bifurcation points, the Jacobian matrix of the dynamical systems has one zero eigenvalue. In contrast, at the Hopf bifurcation points, the solution switches from being stable to exhibiting periodicity, i.e. instability. For the supercritical Hopf bifurcation, one fixed point diverges into periodic oscillations, while the reverse holds true for the subcritical Hopf bifurcation. The occurrence of this Hopf point corresponds to a pair of purely imaginary eigenvalues.

We use a linear gain model for $G(N_{1,2})$ with $G(N_{1,2}) = G_N(N_{1,2} - N_0)$, where G_N is the differential gain and N_0 is the carrier density at transparency. The rate equations in equation (2.1) can be normalized using $X_{1,2} = |E_{1,2}|\sqrt{G_N \tau_{nr}}$, $Y_{1,2} = (N_{1,2} - N_0)\Gamma \tau_p G_N$ and a dimensionless time that is normalized to the photon lifetime as $t = \tau/\tau_p$. We can then write the normalized equation as:

$$\frac{dX_{1,2}}{dt} = \frac{1}{2}(Y_{1,2} - 1)X_{1,2} + \frac{\tau_{nr}}{\tau_{rad}} \frac{F_p \beta}{2} \frac{(Y_{1,2} + N_{o_{norm}})}{|X_{1,2}|^2} |X_{1,2}| \mp \kappa \tau_p \, sin(\Delta\Phi) X_{2,1} + \gamma \tau_p \, cos(\Delta\Phi) \, X_{2,1} \qquad (A.1a)$$

$$\frac{dY_{1,2}}{dt} = T_{norm}\left[P_{norm} - \gamma_c \left(Y_{1,2} + N_{0_{norm}}\right) - Y_{1,2} X_{1,2}^2\right] \qquad (A.1b)$$

$$\frac{d\Delta\Phi}{dt} = \frac{\alpha}{2}(Y_2 - Y_1) + \Delta w \tau_p + \kappa \tau_p \left(\frac{X_1}{X_2} - \frac{X_2}{X_1}\right) cos(\Delta\Phi) - \gamma \tau_p \left(\frac{X_1}{X_2} + \frac{X_2}{X_1}\right) sin(\Delta\Phi) \qquad (A.1c)$$

where $T_{norm} = \tau_p/\tau_{nr}$, $N_{o_{norm}} = N_0\Gamma\tau_p G_N$, $\gamma_c = \frac{\tau_{nr}}{\tau_{rad}}\left(F_p\beta + 1 - \beta\right) + 1$, and $P_{norm} = P_{norm}\Gamma\tau_p G_N/\tau_{nr}$ is the normalized pump rate.

We then perform small signal analysis like in [63] and assume:

$$\begin{gathered} X_{1,2} = \bar{X}_{1,2} + x_{1,2}e^{\lambda t}, Y_{1,2} = \bar{Y}_{1,2} + y_{1,2}e^{\lambda t} \\ \Delta\Phi = \Delta\bar{\Phi} + \delta\phi e^{\lambda t} \end{gathered} \tag{A.2}$$

Substituting $(A.2)$ into $(A.1)$, neglecting higher order terms and assuming $\overline{X_1} \approx \overline{X_2}$, results in:

$$\begin{gathered} x_1\lambda = \frac{1}{2}(\overline{Y_1} - 1)x_1 - \frac{\tau_{nr}}{\tau_{rad}}\frac{F_p\beta}{2}\frac{\left(Y_1 + N_{o_{norm}}\right)}{|\bar{X}_1|^2}x_1 + \left(\frac{1}{2}\bar{X}_1 + \frac{\tau_{nr}}{\tau_{rad}}\frac{F_p\beta}{2}\frac{1}{\bar{X}_1}\right)y_1 \\ +\left[\gamma\tau_p\, cos(\Delta\bar{\Phi}) - \kappa\tau_p sin(\Delta\bar{\Phi})\right]x_2 - \left[\gamma\tau_p\, sin(\Delta\bar{\Phi}) + \kappa\tau_p\, cos(\Delta\bar{\Phi})\right]\bar{X}_2\delta\phi \end{gathered} \tag{A.3a}$$

$$\begin{gathered} x_2\lambda = \frac{1}{2}(\overline{Y_2} - 1)x_2 - \frac{\tau_{nr}}{\tau_{rad}}\frac{F_p\beta}{2}\frac{\left(Y_2 + N_{o_{norm}}\right)}{|\bar{X}_2|^2}x_2 + \left(\frac{1}{2}\bar{X}_2 + \frac{\tau_{nr}}{\tau_{rad}}\frac{F_p\beta}{2}\frac{1}{\bar{X}_2}\right) \\ +\left[\gamma\tau_p\, cos(\Delta\bar{\Phi})\,\_ + \tau_p sin(\Delta\bar{\Phi})\right]x_1 - \left[\gamma\tau_p\, sin(\Delta\bar{\Phi}) - \kappa\tau_p\, cos(\Delta\bar{\Phi})\right]\bar{X}_1\delta\phi \end{gathered} \tag{A.3b}$$

$$y_1\lambda = T_{norm}\left(-\gamma_c y_1 - 2\bar{X}_1\bar{Y}_1 x_1 - \overline{X_1}^2 y_1\right) \tag{A.3c}$$

$$y_2\lambda = T_{norm}\left(-\gamma_c y_2 - 2\bar{X}_2\bar{Y}_2 x_2 - \overline{X_2}^2 y_2\right) \tag{A.3d}$$

$$\begin{gathered} \delta\phi\lambda = \frac{\alpha}{2}(y_2 - y_1) + 2\kappa\tau_p\, cos(\Delta\bar{\Phi})\frac{x_1 - x_2}{\overline{X_1}} \\ -2\gamma\tau_p\, sin(\Delta\bar{\Phi})\frac{x_1 + x_2}{\bar{X}_1} - 2\gamma\tau_p\, cos(\Delta\bar{\Phi})\delta\phi \end{gathered} \tag{A.3e}$$

By considering equal pumping and neglecting the dissipative coupling by setting $\gamma = 0$, the above equations can be further simplified. We then add $(A.3a)$ and $(A.3b)$, as well as $(A.3c)$ and $(A.3d)$ and arrive at:

$$\begin{gathered} (x_1 + x_2)\left[\lambda - \frac{1}{2}(\overline{Y_1} - 1) + \frac{\tau_{nr}}{\tau_{rad}}\frac{F_p\beta}{2}\frac{\left(Y_1 + N_{o_{norm}}\right)}{|\bar{X}_1|^2}\right] \\ = \left(\frac{1}{2}\bar{X}_1 + \frac{\tau_{nr}}{\tau_{rad}}\frac{F_p\beta}{2}\frac{1}{\bar{X}_1}\right)(y_1 + y_2) \end{gathered} \tag{A.4a}$$

$$(x_1 + x_2)(-2T_{norm}\bar{X}_1\bar{Y}_1) = [\lambda + T_{norm}(\gamma_c + \bar{X}_1^2)](y_1 + y_2) \tag{A.4b}$$

Combining $(A.4a)$ and $(A.4b)$, we have: $\lambda^2 + A_1\lambda + A_2 = 0$, where $A_1 = T_{norm}(\gamma_c + \bar{X}_1^2) - \frac{1}{2}(\bar{Y}_1 - 1) + \frac{\tau_{nr}}{\tau_{rad}}\frac{F_p\beta}{2}\frac{(Y_1 + N_{o_{norm}})}{|\bar{X}_1|^2}$.

Recall that $\frac{\tau_{nr}}{\tau_{rad}}\frac{F_p\beta}{2}\frac{(Y_1 + N_{o_{norm}})}{|\bar{X}_1|^2} = -\frac{1}{2}(\bar{Y}_1 - 1)$ and $A_1 = T_{norm}(\gamma_c + \bar{X}_1^2) - (Y_1 - 1)$. In order for the small perturbations to approach zero as time evolves, the real part of λ must be negative. This requires $A_1 = 2Re(\lambda) > 0$. For the expression of A_1, the first term on the RHS signifies the radiative recombination of carriers by all means, and the second term denotes recombination involving only spontaneous emission. Therefore, $A_1 > 0$ always hold true.

We then subtract $(A3b)$ from $(A3a)$, as well as $(A3d)$ from $(A3c)$ and arrive at:

$$\begin{aligned}(x_1 - x_2)\left[\lambda - \frac{1}{2}(\bar{Y}_1 - 1) + \frac{\tau_{nr}}{\tau_{rad}}\frac{F_p\beta}{2}\frac{(Y_1 + N_{o_{norm}})}{|\bar{X}_1|^2}\right] \\ = \left(\frac{1}{2}\bar{X}_1 + \frac{\tau_{nr}}{\tau_{rad}}\frac{F_p\beta}{2}\frac{1}{\bar{X}_1}\right)(y_1 - y_2) - 2\kappa\tau_p\, cos(\Delta\bar{\Phi})\bar{X}_1\delta\phi\end{aligned} \tag{A.5a}$$

$$(x_1 - x_2)(-2T_{norm}\bar{X}_1\bar{Y}_1) = [\lambda + T_{norm}(\gamma_c + \bar{X}_1^2)](y_1 - y_2) \tag{A.5b}$$

Substituting $(A.3e)$ into $(A.5a)$ results in:

$$\lambda^3 + B_1\lambda^2 + B_2\lambda + B_3 = 0 \tag{A.6}$$

where

$$B_1 = T_{norm}(\gamma_c + \bar{X}_1^2) - (\bar{Y}_1 - 1) \tag{A.7a}$$

$$B_2 = T_{norm}\bar{X}_1\bar{Y}_1\left(\bar{X}_1 + \frac{\tau_{nr}}{\tau_{rad}}F_p\beta\frac{1}{\bar{X}_1}\right) - T_{norm}(\gamma_c + \bar{X}_1^2)(\bar{Y}_1 - 1) + 4\kappa^2\tau_p^2\, cos^2(\Delta\bar{\Phi}) \tag{A.7b}$$

$$B_3 = 4\kappa^2\tau_p^2\, cos^2(\Delta\Phi)\, T_{norm}(\gamma_c + \bar{X}_1^2) + 2\alpha\kappa\tau_p T_{norm}\bar{X}_1^2\bar{Y}_1\cos(\Delta\bar{\Phi}) \tag{A.7c}$$

The solutions to $(A.6)$ are one real value and two conjugate complex values. The real solution gives the saddle-node bifurcations or pitchfork bifurcations while the complex solutions gives the Hopf bifurcations.

For very weak coupling, B_3 in equation $(A.7c)$ is approximately 0 and equation (A.6) can be simplified to be quadratic. Consequentially, the solution of λ can then be approximated to be that of the relaxation oscillations (RO), where $Re(\lambda)$ is the damping rate and $Im(\lambda)$ is the RO frequency, which is $T_{norm}(\gamma_c + \bar{X}_1^2) + \frac{\tau_{nr}}{\tau_{rad}} F_p \beta \frac{(Y_1 + N_{o_{norm}})}{|\bar{X}_1|^2}$. In this case, a larger β always results in faster damping, therefore, enhancing the stability in the weak coupling region. The pump rate can also increase the damping rate for small β. For large β, the scenario becomes more complex and requires more detailed examination. However, since the damping rate can be approximated to be that of the RO as $T_{norm}(\gamma_c + \bar{X}_1^2) + \frac{\tau_{nr}}{\tau_{rad}} F_p \beta \frac{(Y_1 + N_{o_{norm}})}{|\bar{X}_1|^2}$, for very small β, the second term can be neglected. This means that as pump rate increases, a larger $\bar{X}_1^2$ gives a faster damping, i.e. better stability. While for larger β, the second term can not be neglected. Since $\bar{X}_1^2$ is now in the denominator, a larger $\bar{X}_1^2$ gives a slower damping rate, i.e. a worse stability.

To have the real parts of the solutions to λ be negative, and thus have stable phase locking, the following conditions must hold,

$$B_1 > 0, B_3 > 0, B_1 B_2 - B_3 > 0 \qquad (A.8)$$

Since $B_1 = A_1 > 0$ has already been proven to be true, we focus on the second and the third conditions.

The condition $B_3 > 0$ makes the real solution negative, and thus yields,

$$4\kappa^2 \tau_p^2 \cos^2(\Delta\bar{\Phi})\, T_{norm}(\gamma_c + \bar{X}_1^2) > -2\alpha\kappa\tau_p T_{norm} \bar{X}_1^2 \bar{Y}_1 \cos(\Delta\bar{\Phi}) \qquad (A.9)$$

In the case of zero detuning, this can be simplified to:

$$\kappa\tau_p > -\frac{\alpha T_{norm} \bar{X}_1^2 \bar{Y}_1}{2T_{norm}(\gamma_c + \bar{X}_1^2)}, \text{when } \Delta\bar{\Phi} = 0, \qquad (A.10a)$$

And

$$\kappa\tau_p > \frac{\alpha T_{norm}\bar{X}_1^2\bar{Y}_1}{2T_{norm}(\gamma_c + \bar{X}_1^2)}, \text{when } \Delta\bar{\Phi} = \pi \qquad (A.10b)$$

For the condition $B_1B_2 - B_3 > 0$ to hold true, the real part of the complex solutions to λ must be negative. Consequentially, this yields a second order equation for κ,

$$C_1\kappa^2 + C_2\kappa + C_3 > 0 \qquad (A.11)$$

where

$$C_1 = -4\, cos^2(\Delta\bar{\Phi})\,(\bar{Y}_1 - 1) \qquad (A.12a)$$

$$C_2 = -2\alpha T_{norm}\, cos(\Delta\bar{\Phi})\,\bar{X}_1^2\bar{Y}_1 \qquad (A.12b)$$

$$C_3 = T_{norm}[T_{norm}(\gamma_c + \bar{X}_1^2) - (\bar{Y}_1 - 1)]\left(\frac{\beta\tau_{nr}}{\tau_{rad}}\bar{Y}_1 - \gamma_c\bar{Y}_1 + \gamma_c + \bar{X}_1^2\right) \qquad (A.12c)$$

An explicit expression describing the stable phase-locking conditions is challenging to obtain. Nevertheless, we can plot out and observe that the Hopf bifurcation boundary with $C_1\kappa^2 + C_2\kappa + C_3 = 0$, is a parabolic function, whose center and width vary with β and P. Each set of parameters generates a different parabolic function, and generates either zero, one or two roots, as shown in Figure **2.3**.

Appendix B Fabrication of bridge-coupled metallo-dielectric nanolasers

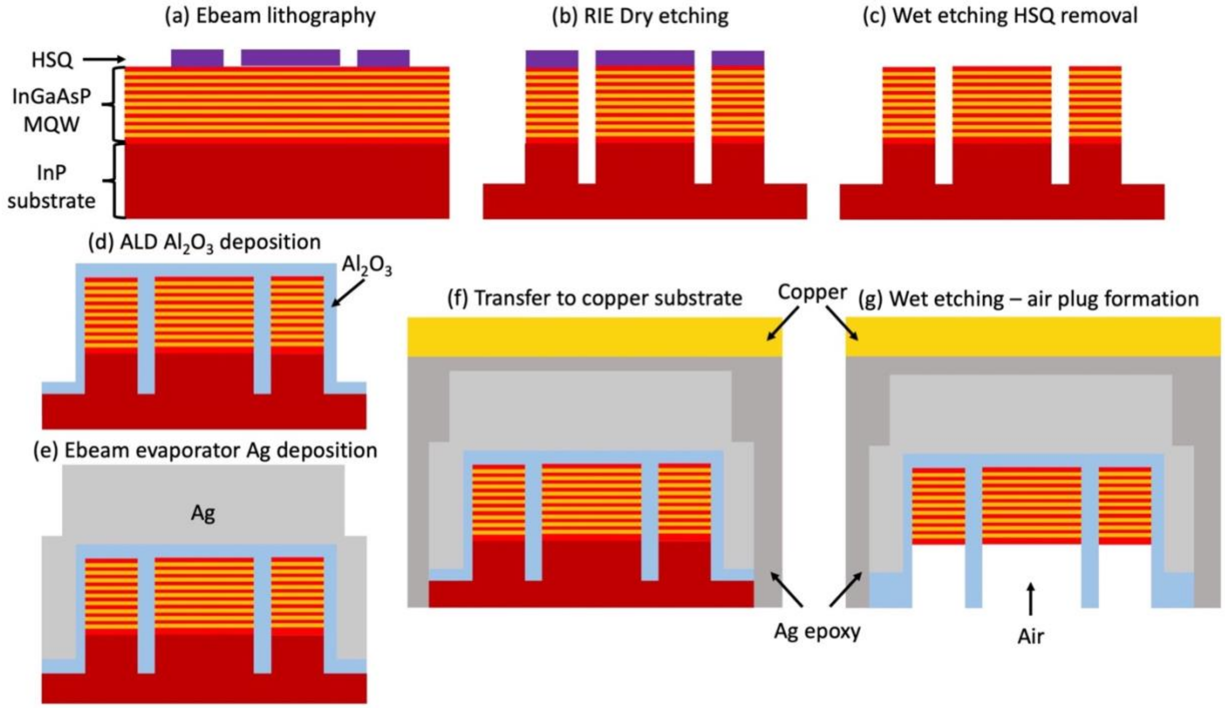

Figure B.1 Fabrication steps of the bridge-coupled metallo-dielectric nanolasers. (a) Ebeam lithography to define the geometries; (b) RIE dry etching to define the pillars; (c) Wet etching for photoresist removal; (d) ALD Al_2O_3 deposition; (e) Ag deposition using Ebeam evaporator; (f) Transfer to copper substrate with Ag epoxy; (g) wet etching of InP to form air plug for optical pumping.

Appendix C Coefficients in the solutions for electric field distribution and Green's functions

$$k_i = \sqrt{\left(\frac{2\pi\sqrt{\epsilon_i}}{\lambda}\right)^2 - \left(\frac{\pi}{1.1}H\right)^2} \qquad (C.1)$$

where $\epsilon_i = 11.56$ for InGaAsP, 2.14 for SiO_2 and $130 - 3i$ for Silver at room temperature [28]. Here, we are given the discrete value from 3-D FEM simulation, and we use E_D to represent the data set. We let $E_{D_0} = E_D / max\,(E_D)$ to denote the data set that gives the normalized field distribution. R denotes the data set of the radial coordinate of all the values. We then have the normalization coefficient *n* as:

$$n = \frac{1}{\sqrt{2\pi \int_V \ r \mid E_{E_0} \mid^2 dr}} \qquad (C.2)$$

Let $E_{R_1} = E_{D_0}(R = R_1)$ and $E_{R_2} = E_{D_0}(R = R_2)$, we have:

$$A_1 = n * max\left(J_1(k_1 R)\right) \qquad (C.3a)$$

$$A_2 = n * \frac{E_{R_2}}{J_1(k_2 R_2) + B_2 Y_1(k_2 R_2)} \qquad (C.3b)$$

$$B_2 = n * \frac{J_1(k_2 R_2) * E_{R_1} - J_1(k_2 R_1) * E_{R_2}}{Y_1(k_2 R_1) * E_{R_2} - Y_1(k_2 R_2) * E_{R_1}} \qquad (C.3c)$$

$$B_3 = n * \frac{E_{R_2}}{K_1(k_3 R_2)} \qquad (C.3d)$$

$$B_1 = A_3 = 0 \qquad (C.3e)$$

While for a_i and b_i:

$$a_i(or\ b_i) = \frac{1}{n}\frac{max(E_D)}{max\left(J_1(k_1 R)\right)} A_i(or\ B_i) \qquad (C.4)$$

Define:

$$J_{ijk} = J_i\left(k_{\rho j} r_k\right)$$

For instance:

$$J_{011} = J_0\left(k_{\rho 1} r_1\right) \qquad (C.5)$$

Similarly, we define $Y_{ijk} = Y_i(k_{\rho j} r_k)$.

We also define Hankel functions as:

$$H_{0111} = H_0^{(1)}\left(k_{\rho 1} r_1\right) \qquad (C.6a)$$

$$H_{1111} = H_1^{(1)}\left(k_{\rho 1} r_1\right) \qquad (C.6b)$$

$$J_{01r} = J_0\left(k_{\rho 1} r'\right) \qquad (C.6c)$$

$$J_{11r} = J_0\left(k_{\rho 1} r'\right) \qquad (C.6d)$$

$$H_{011r} = H_0^{(1)}\left(k_{\rho 1} r'\right) \qquad (C.6e)$$

$$H_{111r} = H_1^{(1)}\left(k_{\rho 1} r'\right) \qquad (C.6f)$$

Define a coefficient to help simplify the expressions:

$$\Lambda = \frac{\eta_1 k_{\rho 1}}{\eta_2 k_{\rho 2}} \times \frac{J_{021} Y_{022} - J_{022} Y_{021}}{J_{121} Y_{022} - J_{022} Y_{121}} \qquad (C.7a)$$

$$g_1 = \frac{g_2 J_{01r} + h_2 H_{011r}}{J_{01r}} \qquad (C.7b)$$

$$g_2 = \frac{\Lambda H_{1111} - H_{0111}}{J_{121} - \Lambda J_{111}} h_2 \qquad (C.7c)$$

$$h_2 = \frac{1}{D_1 H k_{\rho 1} r'} \frac{J_{01r}}{J_{01r} H_{111r} - H_{011r} J_{11r}} \qquad (C.7d)$$

$$g_3 = \frac{\eta_1 k_{\rho 1}}{\eta_2 k_{\rho 2}} Y_{022} \times \frac{g_2 J_{111} + h_2 H_{111}}{J_{121} Y_{022} - J_{022} Y_{121}} \qquad (C.7e)$$

$$h_3 = -\frac{J_{022}}{Y_{022}} g_3 \qquad (C.7f)$$

Appendix D Calculation of PSD of the fundamental thermal noise using Langevin approach and Green's function method

The stochastic thermal diffusion equation reads:

$$\frac{\partial \Delta T(\vec{r},t)}{\partial t} - D_T \nabla_{\vec{r}}^2 \Delta T(\vec{r},t) = F(\vec{r},t) \qquad (D.1)$$

The parameters here are the same as defined above. To solve the above equation, boundary conditions are needed. To start with, the silver layer is considered as an effective heat sink due to its large heat conductivity, so no thermal fluctuation happens in the metal-dielectric interface. Moreover, the temperature fluctuation and its flux need to be continuous at the boundaries.

$$\begin{gathered} \Delta T\ |_{R_2} = 0 \\ \Delta T\ |_{R_1-0} = \Delta T\ |_{R_1+0} \\ \eta_1 \frac{\partial \Delta T}{\partial r}\bigg|_{R_1-0} = \eta_2 \frac{\partial \Delta T}{\partial r}\bigg|_{R_1+0} \end{gathered} \qquad (D.2)$$

Because of the random nature of $F(\vec{r},t)$, there is no first order characterization for it, but its second order characterization is known as:

$$< \tilde{F}(r,iw)\tilde{F}^*(r',iw') >= \frac{4\pi D_T A\ k_B T^2}{\rho c V} \nabla_r \nabla_{r'} \delta(r-r')\delta(w-w') \qquad (D.3)$$

This indicates that our heat source is a point source. Since we are investigating the resonance frequency deviation contributed by the whole cavity, thermodynamic fluctuations of the temperature need to be integrated over the entire mode volume:

$$\Delta \bar{T}(t) = \int_V \Delta T(r,t)|E(r)|^2 r dr \qquad (D.4)$$

Due to the stochastic nature of the internal heat source, a Green's function method is applied to derive the analytical solution for the temperature fluctuation, and consequently, the frequency noise in the nanocavity. To analyze the spectrum, a Fourier transform is performed on (D.1) and the corresponding Green's function produces:

$$wG(\vec{r},\vec{r}';iw) - D_T\nabla_{\vec{r}}^2 G(\vec{r},\vec{r}';iw) = \delta(\vec{r}-\vec{r}') \qquad (D.5)$$

From the definition of Green's function:

$$\Delta\tilde{T}(\vec{r},iw) = \int_V G(\vec{r},\vec{r}';iw)\,\tilde{F}(\vec{r},iw)d\vec{r}' \qquad (D.6)$$

Given equations (D. 4) and (D. 6), using the Wiener-Khinchin theorem, the single-sided PSD, $S_{\Delta T}(w)$, of the temperature fluctuation can then be derived as:

$$\begin{gathered}S_{\Delta T}(w) = 2\times\frac{1}{2\pi} < \Delta\,\tilde{T}(w)\Delta\tilde{T}^*(w') \geq \frac{1}{\pi}\int_V\int_V |E(r)|^2|E(r')|^2 rr'drdr' \times \\ \int_V\int_V G(r,r_1;iw)G^*(r',r_2;iw') \times< \tilde{F}(r_1,iw)\tilde{F}^*(r_2,iw') > dr_1dr_2\end{gathered} \qquad (D.7)$$

According to the Van Vliet-Fassett therorem [189], the quadratic Green's function can be transformed to be linear, which gives:

$$\langle\Delta\tilde{T}(r,iw)\Delta\tilde{T}^*(r',iw')\rangle = \frac{4\pi Ak_BT^2}{\rho cV}Re[G(r,r';iw)]\delta(w-w') \qquad (D.8)$$

And (D.7) becomes:

$$S_{\Delta T}(w) = \frac{4\pi Ak_BT^2}{\rho cV}\int_{\mathrm{V}}\int_V Re[G(r,r';iw)] \times |E(r)|^2|E(r')|^2 rr'drdr' \qquad (D.9)$$

For a pure 2D problem we transfer equation (D.5) into cylindrical coordinates:

$$\frac{d^2G(\vec{r},\vec{r}';iw)}{dr^2} + \frac{1}{r}\frac{dG(\vec{r},\vec{r}';iw)}{dr} + k^2G(\vec{r},\vec{r}';iw) = -\frac{1}{D_TL}\delta(r-r')\delta(w-w') \qquad (D.10)$$

where $k^2 = -iw/D_T$. To obtain the analytical solution of the Green's function in equation (D.10), homogeneous boundary conditions at all medium interfaces are applied. At the point heat source, the continuity of the Green's Function and the discontinuity of its derivative add two more boundary conditions, and the latter could be derived by doing an integration of (D.10) from r’-0 to r’+0:

$$
\begin{gathered}
G|_{r'-0} = G|_{r'+0}, \qquad r\frac{\partial G}{\partial r}\bigg|_{r'-0}^{r'+0} = -\frac{1}{D_T L} \\
G|_{R_1-0} = G|_{R_1+0}, \qquad \eta_1 \frac{\partial G}{\partial r}\bigg|_{R_1-0} = \eta_2 \frac{\partial G}{\partial r}\bigg|_{R_1+0}, \qquad G\ |_{R_2} = 0
\end{gathered} \qquad (D.11)
$$

Solutions for Green's function in this radial symmetric problem are Bessel functions:

$0 \le r \le r'$,

$$G_1^{<}(r, r'; iw) = g_1(r')J_0\big(k_{\rho 1}r\big) \qquad (B.12a)$$

$0 \le r \le r'$,

$$G_1^{>}(r, r'; iw) = g_2(r')J_0\big(k_{\rho 1}r\big) + h_2(r')H_0^{(1)}\big(k_{\rho 1}r\big) \qquad (B.12b)$$

$R_1 \le r \le R_2$,

$$G_2(r, r'; iw) = g_3(r')J_0\big(k_{\rho 2}r\big) + h_3(r')Y_0\big(k_{\rho 2}r\big) \qquad (B.12c)$$

Bibliography

[1] E. I. Galanzha, R. Weingold, D. A. Nedosekin, M. Sarimollaoglu, J. Nolan, W. Harrington, A. S. Kuchyanov, R. G. Parkhomenko, F. Watanabe, S. Z. Nima, A. S. Biris, A. I. Pekhanov, M. I. Stockman and V. P. Zharov, "Spaser as a biological probe," *Nature Communication*, vol. 8, p. 15528, 2017.

[2] R. -M. Ma and O. R. F, "Applications of nanolasers," *Nature Nanotechnology*, vol. 14, pp. 12-22, 2019.

[3] J. A. Schuller, E. S. Barnard, W. Cai, Y. C. Jun, J. S. White and M. L. Brongersma, "Plasmonics for extreme light concentration and manipulation," *Nature Materials*, vol. 9, p. 193, 2010.

[4] Y. Nakayama, P. J. Pauzauskie, A. Radenovic, R. M. Onorato, R. J. Saykally, J. Liphardt and P. Yang, "Tunable nanowire nonlinear optical probe," *Nature*, vol. 447, no. 26, pp. 1098-1101, 2007.

[5] M. Loncar, A. Scherer and Y. Qiu, "Photonic crystal laser sources for chemical detection," *Applied Physics Letters*, vol. 82, no. 26, pp. 4648-4650, 2003.

[6] D. Takahashi, S. Hachuda, W. T, Y. Nishijima and T. Baba, "Detection of endotoxin using a photonic crystal nanolaser," *Applied Physics Letters*, vol. 106, no. 13, p. 131112, 2015.

[7] T. Watanabe, Y. Saijo, Y. Hasegawa, K. Watanabe, Y. Nishijima and T. Baba, "Ion-sensitive photonic-crystal nanolaser sensors," *Optics Express*, vol. 25, pp. 24469-24479, 2017.

[8] D. A. B. Miller, "Device requirements for optical interconnects to silicon chips," *Proceedings of IEEE*, vol. 97, p. 1166, 2009.

[9] D. A. B. Miller, "Are optical transistors the logical next step?," *Nature Photonics*, vol. 4, pp. 3-5, 2010.

[10] I. Prieto, J. M. Llorens, L. E. M. noz Camúñez, A. G. Taboada, J. Canet-Ferrer, J. M. Ripalda, C. Robles, G. M. noz Matutano, J. P. Martínez-Pastor and P. A. Postigo, "Near thresholdless laser operation at room temperature," *Optica*, vol. 2, pp. 66-69, 2015.

[11] O. Painter, R. K. Lee, A. Scherer, A. Yariv, J. D. O'Brien, P. D. Dapkus, and I. Kim, "Two-dimensional photonic band-gap defect mode laser," *Science*, vol. 284, no. 5421, pp. 1819–1821, 1999.

[12] S. Strauf, K. Hennessy, M. T. Rakher, Y. -S. Choi, A. Badolato, L. C. Andreani, E. L. Hu, P. M. Petroff and D. Bouwmeester, "Self-tuned quantum dot gain in photonic crystal lasers," *Physics Review Letters*, vol. 96, p. 127404, 2006.

[13] H. -G. Park, S. -H. Kim, S. -H. Kwon, Y. -G. Ju, J. -K. Yang, J. -H. Baek, S. -B. Kim and Y.

-H. Lee, "Electrically driven single-cell photonic crystal laser," *Science*, vol. 305, no. 5689, pp. 1444-1447, 2004.

[14] B. Ellis, M. A. Mayer, G. Shambat, T. Sarmiento, J. Harris, E. E. Haller and J. Vuckovic, "Ultralow-threshold electrically pumped quantum-dot photonic-crystal nanocavity laser," *Nature Photonics*, vol. 5, pp. 297-300, 2011.

[15] R. Hostein, R. Braive, L. L. Gratiet, A. Talneau, G. Beaudoin, I. Robert-Philip, I. Sagnes and A. Beveratos, "Demonstration of coherent emission from high-β photonic crystal nanolasers at room temperature," *Optics Letters*, vol. 35, pp. 1154-1156, 2010.

[16] Y. -J. Lu, J. Kim, H. -Y. Chen, C. Wu, N. Dabidian, C. E. Sanders, C. -Y. Wang, M. -Y. Lu, B. -H. Li, X. Qiu, W. -H. Chang, L. -J. Chen, G. Shvets, C. -K. Shin and S. Gwo, "Plasmonic nanolaser using epitaxially grown silver film," *Science*, vol. 337, no. 6093, pp. 450-453, 2012.

[17] M. A. Noginov, G. Zhu, A. M. Belgrave, R. Bakker, V. M. Shalaev, E. E. Narimanov, S. Stout, E. Herz, T. Suteewong and U. Wiesner, "Demonstration of a spaser-based nanolaser," *Nature*, vol. 460, pp. 1110-1112, 2009.

[18] R. F. Oulton, V. J. Sorger, T. Zentgraf, R. -M. Ma, C. Gladden, L. Dai, G. Bartal and X. Zhang, "Plasmon lasers at deep subwavelength scale," *Nature*, vol. 461, pp. 629-632, 2009.

[19] D. J. Bergman and M. I. Stockman, "Surface plasmon amplification by stimulated emission of radiation: Quantum generation of coherent surface plasmons in nanosystems," *Physics Review Letters*, vol. 90, p. 027402, 2003.

[20] R. -M. Ma, R. F. Oulton, V. J. Sorger, G. Bartal and X. Zhang, "Room-temperature sub-diffraction-limited plasmon laser by total internal reflection," *Nature Materials*, vol. 10, pp. 110-113, 2011.

[21] R. -M. Ma, R. F. Oulton, V. J. Sorger and Z. X, "Plasmon lasers: coherent light source at molecular scales," *Laser & Photonics Reviews*, vol. 7, no. 1, pp. 1-21, 2013.

[22] R. Chen, T. -T. D. Tran, K. W. Ng, W. S. Ko, L. C. Chuang, F. G. Sedgwick and C. Chang-Hasnain, "Nanolasers grown on silicon," *Nature Photonics*, vol. 5, pp. 170-175, 2011.

[23] D. Saxena, S. Mokkapati, P. Parkinson, N. Jiang, Q. Gao, H. H. Tan and C. Jagadish, "Optically pumped room-temperature gas nanowire lasers," *Nature Photonics*, vol. 7, pp. 963-968, 2013.

[24] M. Khajavikhan, A. Simic, M. Katz, J. H. Lee, B. Slutsky, A. Mizrahi, V. Lomakin and Y. Fainman, "Thresholdless nanoscale coaxial lasers," *Nature*, vol. 482, pp. 204-207, 2012.

[25] K. Ding, M. T. Hill, Z. C. Liu, L. J. Yin, P. J. Van Veldhoven and C. Z. Ning, "Record performance of electrical injection sub-wavelength metallic-cavity semiconductor lasers at room temperature," *Optics Express*, vol. 21, pp. 4728-4733, 2013.

[26] K. Yu, A. Lakhani and M. C. Wu, "Subwavelength metal-optic semiconductor nanopatch

lasers," *Optics Express*, vol. 18, pp. 8790-8799, 2010.

[27] M. T. Hill, Y. -S. Oei, B. Smalbrugge, Y. Zhu, T. de Vries, P. J. van Veldhoven, F. W. M. van Otten, T. J. Eijkemans, J. P. Turkiewicz, H. de Waardt, E. J. Geluk, S. -H. Kwon, Y. -H. Lee, R. Nötzel and M. K. Smit, "Lasing in metallic-coated nanocavities," *Nature Photonics*, vol. 1, pp. 589-594, 2007.

[28] M. P. Nezhad, A. Simic, O. Bondarenko, B. Slutsky, A. Mizrahi, L. Feng, V. Lomakin and Y. Fainman, "Room-temperature subwavelength metallo-dielectric lasers," *Nature Photonics*, vol. 4, pp. 395-399, 2010.

[29] J. H. Lee, M. Khajavikhan, A. Simic, Q. Gu, O. Bondarenko, B. Slutsky, M. P. Nezhad and Y. Fainman, "Electrically pumped sub-wavelength metallo-dielectric pedestal pillar lasers," *Optics Express*, vol. 19, pp. 21524-21531, 2011.

[30] K. Ding, L. Yin, M. T. Hill, Z. Liu, P. J. van Veldhoven and C. Z. Ning, "An electrical injection metallic cavity nanolaser with azimuthal polarization," *Applied Physics Letters*, vol. 102, no. 4, p. 041110, 2013.

[31] M. T. Hill, M. Marell, E. S. P. Leong, B. Smalbrugge, Y. Zhu, M. Sun, P. J. van Veldhoven, E. J. Geluk, F. Karouta, Y. -S. Oei, R. Nötzel, C. -Z. Ning and M. K. Smit, "Lasing in metal-insulator-metal sub-wavelength plasmonic waveguides," *Optics Express*, vol. 17, pp. 11107-11112, 2009.

[32] K. Ding, Z. Liu, L. Yin, H. Wang, R. Liu, M. T. Hill, M. J. H. Marell, P. J. van Veld- hoven, R. Nötzel and C. Z. Ning, "Electrical injection, continuous wave operation of subwavelength-metallic-cavity lasers at 260 k," *Applied Physics Letters*, vol. 98, no. 23, p. 231108, 2011.

[33] K. Ding, Z. Liu, L. Yin, H. Wang, M. T. Hill, M. J. H. Marell, P. J. van Veld- hoven, R. Nötzel and C. Z. Ning, "Room-temperature continuous wave lasing in deep-subwavelength metallic cavities under electrical injection," *Physic Review B*, vol. 85, p. 041301, 2012.

[34] L. A. Coldren and S. W. Corzine, Diode Lasers and Photonic Integrated Circuits, New York: New York: John Wiley & Sons, inc., 1995.

[35] D. T. Caassidy, "Spontaneous-emission factor of semiconductor diode lasers," *Journal of the Optical Society of America B*, vol. 8, pp. 747-752, 1991.

[36] H. Altug, D. Englund and J. Vuckovic, "Ultrafast photonic crystal nanocavity laser," *Nature Physics*, vol. 2, pp. 484-488, 2006.

[37] S. H. Pan, Q. Gu, A. El Amili, F. Vallini and Y. Fainman, "Dynamical Hysteresis in a Coherent High-β Nanolaser," *Optica*, vol. 3, no. 11, pp. 1260-1265, 2016.

[38] A. Mizrahi, V. Lomakin, B. A. Slutsky, N. M. P, F. L and Y. Fainman, "Low threshold gain metal coated laser nanoresonators," *Optics Letters*, vol. 33, p. 1261, 2008.

[39] S. S. Deka, S. H. Pan, Q. Gu, Y. Fainman and A. El Amili, "Coupling in a dual metallo-

dielectric nanolaser system," *Optics Letters*, vol. 42, pp. 4760-4763, 2017.

[40] S. H. Pan, S. S. Deka, A. El Amili, Q. Gu and Y. Fainman, "Nanolasers: Second-order intensity correlation, direct modulation and electromagnetic isolation in array architectures," *Progress in Quantum Electronics*, vol. 59, pp. 1-18, 2018.

[41] C. -Y. Fang, S. H. Pan, F. Vallini, A. Tukiainen, J. Lyytikainen, G. Nylund, B. Kante, M. Guina, A. El Amili and Y. Fainman, "Lasing action in low-resistance nanolasers based on tunnel junctions," *Optics Letters*, vol. 44, no. 15, pp. 3669-3672, 2019.

[42] C. -Y. Fang, F. Vallini, A. El Amili, J. S. T. Smalley and Y. Fainman, "Low Resistance Tunnel Junctions for Efficient Electrically Pumped Nanolasers," *IEEE Journal of Selected Topics in Quantum Electronics*, vol. 23, no. 6, p. 1500506, 2017.

[43] Q. Gu, J. Shane, F. Vallini, B. Wingad, J. S. T. Smalley, N. C. Frateschi and Y. Fainman, "Amorphous Al2O3 Shield for Thermal Management in Electrically Pumped Metallo-Dielectric Nanolasers," *IEEE Journal of Quantum Electronics*, vol. 50, no. 7, pp. 499-509, 2014.

[44] S. S. Deka, S. H. Pan, S. Jiang, A. El Amili, F. Vallini, Q. Gu and Y. Fainman, "Real-time dynamic wavelength tuning and intensity modulation of metal-clad nanolasers," *Optics Express*, vol. 28, no. 19, pp. 27346-27357, 2020.

[45] C. Xu, W. E. Hayenga, M. Khajavikhan and P. Likamwa, "Measuring the frequency response of optically pumped metal-clad nanolasers," *Optics Express*, vol. 27, no. 15, pp. 21834-21842, 2019.

[46] E. K. Lau, A. Lakhani, R. S. Tucker and M. C. Wu, "Enhanced modulation bandwidth of nanocavity light emitting devices," *Optics Express*, vol. 17, pp. 7790-7799, 2009.

[47] T. Suhr, N. Gregersen, K. Yvind and J. Mørk, "Modulation response of nanoleds and nanolasers exploiting purcell enhanced spontaneous emission," *Optics Express*, vol. 18, pp. 11230-11241, 2010.

[48] C. -Y. A. Ni and S. L. Chuang, "Theory of high-speed nanolasers and nanoleds," *Optics Express*, vol. 20, pp. 16450-16470, 2012.

[49] K. Ding, J. O. Diaz, D. Bimberg and C. Z. Ning, "Modulation bandwidth and energy efficiency of metallic cavity semiconductor nanolasers with inclusion of noise effects," *Laser & Photonics Reviews*, vol. 9, no. 5, pp. 488-497, 2015.

[50] R. R’oder, T. P. H. Sidiropoulos, C. Tessarek, S. Christiansen, R. F. Oulton and C. Ronning, "Ultrafast dynamics of lasing semiconductor nanowires," *Nano Letters*, vol. 15, no. 7, pp. 4637-4643, 2015.

[51] S. Hachuda, S. Otsuka, S. Kita, T. Isono, M. Narimatsu, K. Watanabe, Y. Goshima and T. Baba, "elective detection of subatto-molar streptavidin in 10^{13}-fold impure sample using photonic crystal nanolaser sensors," *Optics Express*, vol. 21, no. 10, pp. 12815-12821, 2013.

[52] H. Abe, M. Narimatsu, T. Watanabe, T. Furumoto, Y. Yokouchi, Y. Nishijima, S. Kita, A. Tomitaka, S. Ota, Y. Takemura and T. Baba, "Living-cell imaging using a photonic crystal nanolaser array," *Optics Express*, vol. 23, no. 13, pp. 17056-17066, 2015.

[53] C. V. Poulton, A. Yaacobi, D. B. Cole, M. J. Byrd, M. Raval, D. Vermeulen and M. R. Watts, "Coherent solid-state LIDAR with silicon photonic optical phased arrays," *Optics Letters*, vol. 42, no. 20, pp. 4091-4094, 2017.

[54] J. Feng, W. Wen, X. Wei, X. Jiang, M. Cao, X. Wang, X. J. L. Zhang and Y. Wu, "Random organic nanolaser arrays for cryptographic primitives," *Advanced Materials*, vol. 31, no. 36, p. 1807880, 2019.

[55] D. Kedar and S. Arnon, "Urban optical wireless communication networks: The main challenges and possible solutions," *IEEE Communication Magzine*, vol. 42, no. 5, pp. S2-S7, 2004.

[56] P. Hamel, S. Haddadi, F. Raineri, P. Monnier, G. Beaudoin, I. Sagnes, A. Levenson and A. M. Yacomotti, "Spontaneous mirror- symmetry breaking in coupled photonic-crystal nanolasers," *Nature Photonics*, vol. 9, pp. 311-315, 2015.

[57] S. Haddadi, P. Hamel, G. Beaudoin, I. Sagnes, C. Sauvan, P. Lalanne, J. A. Levenson and A. M. Yacomotti, "Photonic molecules: tailoring the coupling strength and sign," *Optics Express*, vol. 22, no. 10, pp. 12359-12368, 2014.

[58] M. Marconi, J. Javaloyes, F. Raineri, J. A. Levenson and A. M. Yacomotti, "Asymmetric mode scattering in strongly coupled photonic crystal nanolasers," *Optics Letters*, vol. 41, pp. 5628-5631, 2016.

[59] M. J. Adams, D. Jevtics, M. J. Strain, I. D. Henning and A. Hurtado, "High-frequency dynamics of evanescently-coupled nanowire lasers," *Scientific Report*, vol. 9, pp. 1-7, 2019.

[60] H. G. Winful and L. Rahman, "Synchronized chaos and spatiotemporal chaos in arrays of coupled lasers," *Physics Review Letter*, vol. 65, p. 1575, 1990.

[61] S. S. Wang and H. G. Winful, "Dynamics of phase-locked semiconductor laser arrays," *Applied Physics Letters*, vol. 52, no. 21, pp. 1774-1776, 1998.

[62] H. G. Winful and W. S. S, "Stability of phase locking in coupled semiconductor laser arrays," *Applied Physics Letters*, vol. 53, no. 20, pp. 1894-1896, 1998.

[63] M. Adams, B. N. C. Li, H. Susanto and I. Henning, "Effects of detuning, gain-guiding, and index antiguiding on the dynamics of two laterally coupled semiconductor lasers," *Physics Review A*, vol. 95, no. 5, p. 053869, 2017.

[64] H. Erzgraber, S. Wieczorek and B. Krauskopf, "Dynamics of two laterally coupled semiconductor lasers: Strong-and weak-coupling theory," *Physics Review E*, vol. 78, no. 6, p. 066201, 2008.

[65] J. Shena, J. Hizanidis, V. Kovanis and G. P. Tsironis, "Turbulent chimeras in large

semiconductor laser arrays," *Scientific Report*, vol. 7, no. 1, p. 42116, 2017.

[66] B. G. Lee, J. Kansky, A. K. Goyal, C. Pflügl, L. Diehl, M. A. Belkin, A. Sanchez and F. Capasso, "Beam combining of quantum cascade laser arrays," *Optics Express*, vol. 17, no. 18, pp. 16216-16224, 2009.

[67] T. -K. Kao, J. L. Reno and Q. Hu, "Phase-locked laser arrays through global antenna mutual coupling," *Nature Photonics*, vol. 10, no. 8, pp. 541-546, 2016.

[68] Z. Jia, L. Wang, J. Zhang, Y. Zhao, C. Liu, S. Zhai, N. Zhuo, J. Liu, L. Wang, S. Liu, F. Liu and Z. Wang, "Phase-locked array of quantum cascade lasers with an intracavity spatial filter," *Applied Physics Letters*, vol. 111, p. 061108, 2017.

[69] D. Kwong, A. Hosseini, J. Covey, Y. Zhang, X. Xu, H. Subbaraman and R. T. Chen, "On-chip silicon optical phased array for two-dimensional beam steering," *Optics Letters*, vol. 39, no. 4, pp. 941-944, 2014.

[70] J. K. Doylend, M. J. R. Heck, J. T. Bovington, J. D. Peters, L. A. Coldren and J. E. Bowers, "Two-dimensional free-space beam steering with an optical phased array on silicon-on-insulator," *Optics Express*, vol. 19, no. 22, pp. 21595-21604, 2011.

[71] C. Henry, "Theory of the linewidth of semiconductor lasers," *IEEE Journal of Quantum Electronics*, vol. 18, no. 2, pp. 59-64, 1982.

[72] S. Shahin, F. Vallini, F. Monifi, M. Rabinovich and Y. Fainman, "Heteroclinic dynamics of coupled semiconductor lasers with optoelectronic feedback," *Optics Letters*, vol. 41, no. 22, pp. 5238-5241, 2016.

[73] B. Bahari, A. Ndao, F. Vallini, A. El Amili, Y. Fainman and B. Kante, "Nonreciprocal lasing in topological cavities of arbitrary geometries," *Science*, vol. 358, no. 6363, pp. 636-640, 2017.

[74] M. P. Hokmabadi, N. S. Nye, R. El-Ganainy, D. N. Christodoulides and M. Khajavikhan, "Supersymmetric laser arrays," *Science*, vol. 363, no. 6427, pp. 623-626, 2019.

[75] M. Marconi, F. Raineri, A. Levenson, A. M. Yacomotti, J. Javaloyes, S. H. Pan, A. El Amili and Y. Fainman, "Mesoscopic limit cycles in coupled nanolasers," *Physical Review Letters*, vol. 124, no. 21, p. 213602, 2020.

[76] Q. Gu, B. Slutsky, F. Vallini, J. S. T. Smalley, M. P. Nezhad, N. C. Frateschi and Y. Fainman, "Purcell effect in sub-wavelength semiconductor lasers," *Optics Express*, vol. 21, no. 13, pp. 15603-15617, 2013.

[77] Q. Gu, J. S. T. Smalley, M. P. Nezhad, A. Simic, L. J. H, B. Slutsky, A. Mizrahi, V. Lomakin and Y. Fainman, "Subwavelength semiconductor lasers for dense chip-scale integration," *Advances in Optics and Photonics*, vol. 6, no. 1, pp. 1-56, 2014.

[78] E. Schlottmann, S. Holzinger, B. Lingnau, K. Ludge, C. Schneider, M. Kamp, S. Hofling, J. Wolters and S. Reitzenstein, "Injection locking of quantum-dot microlasers operating in the few-

photon regime," *Physical Review Applied*, vol. 6, p. 044023, 2016.

[79] S. Kreinberg, X. Porte, D. Schicke, B. Lingnau, C. Schneider, S. Hofling, I. Kanter, K. Ludge and S. Reitzenstein, "Mutual coupling and synchronization of optically coupled quantum-dot micropillar lasers at ultra-low light levels," *Nature Communications*, vol. 10, no. 1, p. 1539, 2019.

[80] T. Suhr, P. T. Kristensen and J. Mork, "Phase-locking regimes of photonic crystal nanocavity laser arrays," *Applied Physics Letters*, vol. 99, no. 25, p. 251104, 2011.

[81] B. Romeira and A. Foire, "Purcell effect in the stimulated and spontaneous emission rates of nanoscale semiconductor lasers," *IEEE Journal of Quantum Electronics*, vol. 54, no. 2, pp. 1-12, 2018.

[82] J. B. Khurgin and M. A. Noginov, "How do the Purcell factor, the Q factor and the Beta factor affect the laser threshold?," *Lasers & Photonics Review*, vol. 15, no. 3, p. 20000250, 2021.

[83] B. Ermentrout, Simulating, analyzing, and animating dynamical systems: a guide to XPPAUT for researchers and students, Philadelphia, PA, USA: Society for Industrial and Applied Mathematics, 2002.

[84] Y. Halioua, A. Bazin, P. Monnier, T. J. Karle, G. Roelkens, I. Sagnes, R. Raj and F. Raineri, "Hybrid III-V semiconductor/silicon nanolaser," *Optics Express*, vol. 19, no. 10, pp. 9221-9231, 2011.

[85] Y. Zhao, C. Qian, K. Qiu, Y. Gao and X. Xu, "Ultrafast optical switching using photonic molecules in photonic crystal waveguides," *Optics Express*, vol. 23, no. 7, pp. 9211-9220, 2015.

[86] K. A. Atlasov, K. F. Karlsson, A. Rudra, B. Dwir and E. Kapon, "Wavelength and loss splitting in directly coupled photonic-crystal defect microcavities," *Optics Express*, vol. 16, no. 20, pp. 16255-16264, 2008.

[87] Z. Gao, D. Siriani and K. D. Choquette, "Coupling coefficient in antiguided coupling: magnitude and sign control," *Journal of Optical Society of America B*, vol. 35, no. 2, pp. 417-422, 2018.

[88] P. Antonik, M. C. Wicks, H. D. Grinffiths and C. J. Baker, "Frequency diverse array radars," in *IEEE Conference on Radar,* 2006.

[89] A. Yao, W. Wu and D. Fang, "Frequency diverse array antenna using time-modulated optimized frequency offset to obtain time-invariant spatial fine focusing beampattern," *IEEE Transactions on Antennas and Propagation*, vol. 64, no. 10, pp. 4434-4446, 2016.

[90] Y. Xu, X. Shi, J. Xu and P. Li, "Range-angle-dependent beamforming of pulsed frequency diverse array.," *IEEE Transactions on Antennas and Propagation*, vol. 63, no. 7, pp. 3262-3267, 2015.

[91] G. Crosnier *et al.*, "Hybrid indium phosphide-on-silicon nanolaser diode," *Nature*

Photonics, vol. 11, no. 5, pp. 297-300, 2017.

[92] L. Liu *et al.*, "An ultra-small, low-power, all-optical flip-flop memory on a silicon chip," *Nature Photonics*, vol. 4, no. 3, pp. 182-187, 2010.

[93] P. McMahon *et al.*, "A fully programmable 100-spin coherent Ising machine with all-to-all connections," *Science*, vol. 354, no. 631, pp. 614-617, 2016.

[94] M. Fridman, M. Nixon, N. Davidson and A. A. Friesem, "Passive phase locking of 25 fiber lasers," *Optics Letters*, vol. 35, no. 9, pp. 1434-1436, 2010.

[95] M. Nixon, M. Friedman, E. Ronen, A. A. Friesem, N. Davidson and I. Kantor, "Synchronized cluster formation in coupled laser networks," *Physics Review E*, vol. 22, p. 223901, 2011.

[96] T. Wang, J. Zhou, G. P. Puccioni, W. Zhao, X. Lin, H. Chen, G. Wang and G. L. Lippi, "Methodological investigation into the noise influence on nanolasers' large signal modulation," *Optics Express*, vol. 29, no. 4, pp. 5081-5097, 2021.

[97] J. Mork and G. L. Lippi, "Rate equation description of quantum noise in nanolasers with few emitters," *Applied Physics Letters*, vol. 112, no. 14, p. 111403, 2018.

[98] A. Yang, T. B. Hoang, M. Dridi, C. Deeb, M. H. Mikkelsen, G. C. Schatz and T. W. Odom, "Real-time tunable lasing from plasmonic nanocavity arrays," *Nature Communications*, vol. 6, no. 1, 2016.

[99] S. Jiang, S. Deka, S. H. Pan and Y. Fainman, "Effects of High-β on Phase-locking Stability and Tunability in Laterally Coupled Lasers," *IEEE Journal of Selected Topics in Quantum Electronics*, vol. 28, p. 1800312, 2022.

[100] A. Yacomotti, S. Haddadi and S. Barbay, "Self-pulsing nanocavity laser," *Physical Review A*, vol. 87, p. 041804, 2013.

[101] J. Notaros, M. Notaros, M. Ravel, C. V. Poulton, M. J. Byrd and e. al, "Integrated optical phased arrays: LiDAR, augmented reality, and beyond," in *Integrated Photonics Research, Silicon and Nanophotonics*, 2019.

[102] J. Notaros, M. Raval, M. Notaros and M. R. Watts, "Integrated-phased-array-based visible-light near-eye holographic projector," in *Conference on Lasers and Electro-Optics*, San Jose, 2019.

[103] T. Baba, "Biosensing using photonic crystal nanolasers," *MRS Communications*, vol. 5, no. 4, pp. 555-564, 2015.

[104] K. Watanabe, M. Nomoto, F. Nakamura, S. Hachuda, A. Sakata, T. Wtanabe, Y. Goshima and T. Baba, "Label-free and spectral-analysis-free detection of neuropsychiatric disease biomarkers using an ion-sensitive GaInAsP nanolaser biosensor," *Biosensors and bioelectronics*, vol. 117, pp. 161-167, 2018.

[105] S. Kita, Y. Nishijima, H. Misawa and T. Baba, "Label-Free Biosensing Utilizing Ultrasmall Photonic Crystal Nanolaser," in *Advances in Optical Sciences Congress*, Honolulu, Hawaii, USA, 2009.

[106] X. Wu, Q. Chen, P. Xu, Y. C. Chen, B. Wu, R. M. Coleman, L. Tong and X. Fan, "Nanowire lasers as intracellular probes," *Nanoscale*, vol. 10, no. 20, pp. 9729-9735, 2018.

[107] M. Schubert, A. Steude, P. Liehm, N. M. Kronenberg, M. Karl, E. C. Campbell, S. J. Powis and M. C. Gather, "Lasing within Live Cells Containing Intracellular Optical Microresonators for Barcode-Type Cell Tagging and Tracking," *Nano Letters*, vol. 15, no. 8, pp. 5647-5652, 2015.

[108] A. H. Fikouras, M. Schubert, M. Karl, J. D. Kumar, S. J. Powis, A. Di Falco and M. C. Gather, "Non-obstructive intracellular nanolasers," *Nature Communications*, vol. 9, no. 1, p. 4817, 2018.

[109] M. Lorke, T. Suhr, N. Gregersen and J. Mork, "Theory of nanolaser devices: Rate equation analysis versus microscopic theory," *Physical Review B*, vol. 87, no. 20, pp. 1-10, 2013.

[110] S. Kedia, "“Laser emission from self-assembled active photonic crystal matrix," Journal of *Nanophotonics*, vol. 4, no. 1, p. 049506, 2010.

[111] K. Xu, "“Integrated Silicon Directly Modulated Light Source Using p-Well in Standard CMOS Technology," *IEEE Sensors Journal*, vol. 16, no. 16, pp. 6184-6191, 2016.

[112] T. C. P. Chui, D. R. Swanson, M. J. Adrians, J. A. Nissen and L. J. A, "Temperature fluctuations in the canonical ensemble," *Physical Review Letters*, vol. 69, no. 21, pp. 3005-3008, 1992.

[113] L. D. Landau and E. M. Lifshitz, Course of Theoretical Physics Vol 5: Statistical Physics, Pergamon Press, 1980.

[114] K. Kikuchi, "Fundamentals of Coherent Optical Fiber Communications," *Journal of Lightwave Technology*, vol. 34, no. 1, pp. 157-179, 2016.

[115] S. S. Harilal, N. L. Lahave and M. C. Phillips, "High-resolution spectroscopy of laser ablation plumes using laser-induced fluorescence," *Optics Express*, vol. 25, no. 3, p. 2312, 2017.

[116] S. Foster, A. Tikhomirov and M. Milnes, "Fundamental Thermal Noise in Distributed Feedback Fiber Lasers," *IEEE Journal of Quantum Electronics*, vol. 43, no. 5, pp. 378-384, 2007.

[117] H. Mestric, R. -A. Eichel, K. -P. Dinse, A. Ozarowski, J. V. Tol and L. C. Brunel, "High-frequency electron paramagnetic resonance investigation of the Fe3 impurity center in polycrystalline PbTiO3 in its ferroelectric phase," *Journal of Applied Physics*, vol. 96, no. 12, pp. 7440-7444, 2004.

[118] G. E. Shtengel, R. F. Kazarinov, G. L. Belenky, M. S. Hybersten and D. A. Ackerman, "Advances In Measurements Of Physical Parameters Of Semiconductor Lasers," *International Journal of High Speed Electronics and Systems*, vol. 9, no. 4, pp. 901-940, 1998.

[119] V. Braginsky, M. Gorodetsky and S. Vvatchanin, "Thermodynamical fluctuations and photo-thermal shot noise in gravitational wave antennae," *Physics Letters A*, vol. 264, no. 1, pp. 1-10, 1999.

[120] M. L. Gorodetsky and G. I. S, "Fundamental thermal fluctuations in microsphere," *Journal of the Optical Society of America B,* vol. 21, no. 4, p. 697, 2004.

[121] T. Liu and Q. J. Wang, "Fundamental frequency noise and linewidth broadening caused by intrinsic temperature fluctuations in quantum cascade lasers," *Physical Review B*, vol. 84, no. 12, 2011.

[122] K. V. Vliet and E. Chenette, "Noise spectra resulting from diffusion processes in a cylindrical geometry," *Physica,* vol. 31, no. 7, pp. 985-1001, 1965.

[123] K. M. V. Vliet and H. Mehta, "Theory of Transport Noise in Semiconductors," *Physica Status Solidi (B),* vol. 106, no. 1, pp. 11-30, 1981.

[124] K. Petermann, "Laser diode modulation and noise," Dordrecht: Kluwer, 1991, pp. 196-198.

[125] Q. Gu, J. S. T. Smalley, J. Shane, O. Bondarenko and Y. Fainman, "Temperature effects in metal-clad semiconductor nanolasers," *Nanophotonics,* vol. 4, no. 1, 2015.

[126] K. Ding, Z. Liu, L. Yin, M. Hill, J. H. Marell, P. J. V. Veldhoven, R. Noetzel and Z. Ning, "CW operation of a subwavelength metal-semiconductor nanolaser at record high temperature under electrical injection," in *IEEE Winter Topicals*, 2011.

[127] S. De, F. Bretenaker, R. Ghosh, R. Tualle-Brouri, A. Tropper, A. Amy-Klein, M. Alouini, I. Robert-Phillip and G. Baili, Noise in dual-frequency semiconductor and solid-state lasers, Paris: Universite Paris Sud - Parix XI, 2015.

[128] A. Nakagawa, S. Ishii and T. Baba, "Photonic molecule laser composed of GaInAsP microdisks," *Applied Physics Letters,* vol. 86, p. 041112, 2005.

[129] S. V. Boriskina, "Spectrally engineered photonic molecules as optical sensors with enhanced sensitivity: a proposal and numerical analysis," *Journal of the Optical Society of America B,* vol. 23, pp. 1565-1573, 2006.

[130] S. V. Boriskina, "Coupling of whispering-gallery modes in size-mismatched microdisk photonic molecules," *Optics Letters,* vol. 32, pp. 1557-1559, 2007.

[131] E. I. Smotrova, A. I. Nosich, T. M. Benson and P. Sewell, "Optical coupling of whispering-gallery modes of two identical microdisks and its effect on photonic molecule lasing," *IEEE Journal of Selected Topics in Quantum Electronics,* vol. 12, pp. 78-85, 2006.

[132] S. Ishii, A. Nakagawa and T. Baba, "Modal characteristics and bistability in twin microdisk photonic molecule lasers," *IEEE Journal of Selected Topics in Quantum Electronics,* vol. 12, pp. 71-77, 2006.

[133] H. Han and K. A. Shore, "Dynamics and stability of mutually coupled nano-lasers," *IEEE Journal of Quantum Electronics*, vol. 52, pp. 1-6, 2016.

[134] M. Parto, W. Hayenga, A. C. D. N. Marandi and M. Khajavikhan, "Realizing spin Hamiltonians in nanoscale active photonic lattices," *Nature Materials*, vol. 19, pp. 725-731, 2020.

[135] M. Parto, W. E. Hayenga, A. Marandi, D. N. Christodoulides and M. Khajavikhan, "Nanolaser-based emulators of spin Hamiltonians," *Nanophotonics*, vol. 9, pp. 4193-4198, 2020.

[136] N. Caselli, F. Intonti, F. Riboli *et al.*, "Antibonding ground state in photonic crystal molecules," *Physical Review B*, vol. 86, p. 035133, 2012.

[137] N. Caselli, F. Intonti, F. Riboli and M. Gurioli, "Engineering the mode parity of the ground state in photonic crystal molecules," *Optics Express*, vol. 22, pp. 4953-4959, 2014.

[138] M. Marconi, J. Javaloyes, P. Hamel, F. Raineri, A. Levenson and A. M. Yacomotti, "Far-from-equilibrium route to superthermal light in bimodal nanolasers," *Physical Review X*, vol. 8, p. 011013, 2018.

[139] M. Smit, J. J. Van der Tol and M. Hill, "Moore’s law in photonics," *Laser Photonics Review*, vol. 6, pp. 1-3, 2012.

[140] J. J. Wu, H. Gao, R. Lai *et al.*, "Near-infrared organic single-crystal nanolaser arrays activated by excited-state intramolecular proton transfer," *Matter*, vol. 2, pp. 1233-1243, 2020.

[141] H. Kim, W. J. Lee, A. C. Farrell *et al.*, "MonolithicInGaAsnanowire array lasers on silicon-on-insulator operating at room temperature," *Nano Letters*, vol. 17, pp. 3465-3470, 2017.

[142] H. Yan, R. He, J. Johnson, M. Law, R. J. Saykally and P. Yang, "Dendritic nanowire ultraviolet laser array," *Journal of America Chemical Society*, vol. 125, pp. 4728-4729, 2003.

[143] S. T. Ha, Y. H. Fu, N. K. Emani *et al.*, "Directional lasing in resonant semiconductor nanoantenna arrays," *Nature Nanotechnology*, vol. 12, pp. 1042-1047, 2018.

[144] A. Kodigala, T. Lepetit, Q. Gu, B. Bahari, Y. Fainman and B. Kante, "Lasing action from photonic bound states in continuum," *Nature*, vol. 541, p. 196, 2017.

[145] T. J. Lin, H. L. Chen, Y. F. Chen and S. Cheng, "Room-temperature nanolaser from CdSe nanotubes embedded in anodic aluminum oxide nanocavity arrays," *Applied Physics Letters*, vol. 93, p. 223903, 2008.

[146] K. Wang, Z. Gu, S. Liu *et al.*, "High-density and uniform lead halide perovskite nanolaser array on silicon," *Journal of Physical Chemistry Letters*, vol. 7, pp. 2549-2555, 2016.

[147] D. Wang, A. Yang, W. Wang *et al.*, "Band-edge engineering for controlled multi-modal nanolasing in plasmonic superlattices," *Nature Nanotechnology*, vol. 12, p. 889, 2017.

[148] S. Pourjamal, T. K. Hakala, M. Necada and e. al, "Lasing in Ni nanodisk arrays," *ACS*

Nano, vol. 13, pp. 5686-5692, 2019.

[149] W. Zhou, M. Dridi, J. Y. Suh and e. al, "Lasing action in strongly coupled plasmonic nanocavity arrays," *Nature Nanotechnology*, vol. 8, p. 506, 2013.

[150] X. Meng, J. Liu, A. V. Kildishev and V. M. SHalaev, "Highly directional spaser array for the red wavelength region," *Laser & Photonics Review*, vol. 8, pp. 896-903, 2014.

[151] M. P. Knudson, R. Li, D. Wang, W. Wang, R. D. Shaller and T. W. Odom, "Polarization-dependent lasing behavior from low- symmetry nanocavity arrays," *ACS Nano*, vol. 13, pp. 7435-7441, 2019.

[152] J. Y. Suh, C. H. Kim, W. Zhou and e. al, "Plasmonic bowtie nanolaser arrays," *Nano Letters*, vol. 12, pp. 5769-5774, 2012.

[153] F. van Beijnum, P. J. van Veldhoven, E. J. Geluk, M. J. de Dood, W. Gert and M. P. van Exter, "Surface plasmon lasing observed in metal hole arrays," *Physics Review Letters*, vol. 110, p. 206802, 2013.

[154] C. Huang, W. Sun, Y. Fan and e. al, "Formation of lead halide perovskite based plasmonic nanolasers and nanolaser arrays by tailoring the substrate," *ACS Nano*, vol. 12, pp. 3865-3874, 2018.

[155] Y. H. Chou, K. B. Hong, C. T. Chang and e. al, "Ultracompact pseudowedge plasmonic lasers and laser arrays," *Nano Letters*, vol. 18, pp. 747-753, 2018.

[156] W. E. Hayenga, M. Parto, H. Hodaei, P. LiKamWa, D. N. Christodoulides and M. Khajavikhan, "Coupled metallic nanolaser arrays," in *Conference on Lasers and Electro-Optics (CLEO)*, San Jose, 2017.

[157] W. E. Hayenga, M. Parto, E. S. Cristobal, D. N. Christodoulides and M. Khajavikhan, "Direct generation of structured light in metallic nanolaser arrays," in *Conference on Lasers and Electro-Optics (CLEO)*, San Jose, 2018.

[158] M. Parto, W. Wayenga, D. N. Christodoulides and M. Khajavikhan, "Mode-dependent coupling and vectorial optical vortices in metallic nanolaser arrays," in *Conference on Lasers and Electro-Optics (CLEO)*, San Jose, 2019.

[159] A. F. Koenderink, "Plasmon nanocavity array lasers: cooperating over losses and competing for gain," *ACS Nano*, vol. 13, pp. 7377-7382, 2019.

[160] M. B. Ross, C. A. Mirkin and G. C. Schatz, "Optical properties of one-, two-, and three-dimensional arrays of plasmonic nanostructures," *Journal of Physical Chemistry C*, vol. 120, pp. 816-830, 2016.

[161] G. Cossu, A. M. Khalid, P. Choudhury, R. Corsini and E. Ciaramella, "3.4 Gbit/s visible optical wireless transmission based on RGB LED," *Optics Express*, vol. 20, pp. B501-B506, 2012.

[162] P. Xu, J. Gong, X. Guo, C. Xin, H. Wu, P. Qing, X. Lin, W. Fang, D. Di and L. Tong, "Fast lasing wavelength tuning in single nanowires," *Advanced Optical Materials*, vol. 7, no. 20, p. 1900797, 2019.

[163] J. Cheng, C. L. Shieh, X. D. Huang and e. al, "Efficient long wavelength AlGaInAs vertical-cavity surface-emitting lasers for coarse WDM applications over multimode fibre," *Electronic Letters,* vol. 40, pp. 1184-1185, 2004.

[164] M. T. Hill and M. C. Gather, "Advances in small lasers," *Nature Photonics,* vol. 8, p. 908, 2014.

[165] W. Lewoczko-Adamczyk, C. Pyrlik, J. Hager, S. Schwertfeger, A. Wicht, A. Peters, G. Erbert and G. Trankle, "Ultra-narrow linewidth DFB-laser with optical feedback from a monolithic confocal Fabry-Perot cavity," *Optics Express*, vol. 23, no. 8, pp. 9705-9709, 2015.

[166] Y. Gao, S. Lee, R. Patel, J. -C. Lo, J. Sun, L. Zhu, J. Zhou and J. Hong, "High-performance hybrid-integrated silicon photonic tunable laser," in *Optical Fiber Communication Conference (OFC),* San Diego, California, United States, 2019.

[167] Y. Gao, J. -C. Lo, S. Lee, R. Patel, L. Zhu, J. Nee, D. Tsou, R. Carney and J. Sun, "High-Power, Narrow-Linewidth, Miniaturized Silicon Photonic Tunable Laser With Accurate Frequency Control," *Journal of Lightwave Technology*, vol. 38, no. 2, pp. 265-271, 2020.

[168] J. Kim, A. Shinya, K. Nozaki, H. Taniyama, C. -H. Chen, T. Sato, S. Matsuo and M. Notomi, "Narrow linewidth operation of buried-heterostructure photonic crystal nanolaser," *Optics Express*, vol. 20, no. 11, pp. 11643-11651, 2012.

[169] N. Li, D. Vermeulen, Z. Su, E. S. Magden, M. Xin, N. Singh, A. Ruocco, J. Notaros, C. V. Poulton, E. Timurdogan, C. Baiocco and M. R. Watts, "Monolithically integrated erbium-doped tunable laser on a CMOS-compatible silicon photonics platform," *Optics Express*, vol. 26, no. 13, pp. 16200-16211, 2018.

[170] F. Qian, Y. Li, S. Gradecak, H. -G. Park, Y. Dong, Y. Ding, Z. L. Wang and C. M. Lieber, "Multi-quantum-well nanowire heterostructures for wavelength-controlled lasers," *Nature Materials*, vol. 7, no. 9, pp. 701-706, 2008.

[171] Y. Fu, H. Zhu, C. C. Stoumpos, Q. Ding, J. Wang, M. G. Kanatzidis, X. Zhu and X. Jin, "Broad wavelength tunable robust lasing from single-crystal nanowires of cesium lead halide perovskites (CsPbX3, X = Cl, Br, I)," *ACS Nano*, vol. 10, no. 8, pp. 7963-7972, 2016.

[172] Y. J. Lu, C. Y. Wang, J. Kim, H. Y. Chen, M. Y. Lu, Y. C. Chen, W. H. Chang, L. J. Chen, M. I. Stockman, C. K. Shih and S. Gwo, "All-color plasmonic nanolasers with ultralow thresholds: autotuning mechanism for single-mode lasing," *Nano Letters,* vol. 14, no. 8, pp. 4381-4388, 2014.

[173] H. Zhu, Y. Fu, F. Meng, X. Wu, Z. Gong, Q. Ding, M. V. Gustafsson, M. T. Trinh, S. Jin and X. Y. Zhu, "Lead halide perovskite nanowire lasers with low lasing thresholds and high quality factors," *Nature Materials*, vol. 14, no. 6, pp. 636-642, 2015.

[174] Y. Lu, F. Gu, C. Meng, H. Yu, Y. Ma, W. Fang and L. Tong, "Multicolour laser from a single bandgap-graded CdSSe alloy nanoribbon," *Optics Express*, vol. 21, no. 19, pp. 22314-22319, 2013.

[175] X. Liu, Q. Zhang, J. N. Yip, Q. Xiong and T. C. Sum, "Wavelength tunable single nanowire lasers based on surface plasmon polariton enhanced burstein−moss effect," *Nano Letters*, vol. 13, no. 11, pp. 5336-5343, 2013.

[176] Z. Yang, D. Wang, C. Meng, Z. Wu, Y. Wang, Y. Ma, L. Dai, X. Liu, T. Hasan, X. Liu and Q. Yang, "Broadly defining lasing wavelengths in single bandgap-graded semiconductor nanowires," *Nano Letters*, vol. 14, no. 6, pp. 3153-3159, 2014.

[177] M. Zapf, R. Roder, K. Winkler, L. Kaden, J. Greil, M. Wille, M. Grundmann, R. Schmidt-Grund, A. Lugstein and C. Ronning, "Dynamical tuning of nanowire lasing spectra," *Nano Letters*, vol. 17, no. 11, pp. 6637-6643, 2017.

[178] S. Liu, C. Li, J. J. Figiel, S. R. J. Brueck, I. Brener and G. T. Wang, "Continuous and dynamic spectral tuning of single nanowire lasers with subnanometer resolution using hydrostatic pressure," *Nanoscale*, vol. 7, no. 21, pp. 9581-9588, 2015.

[179] R. Boeck, N. A. F. Jaeger, N. Rouger and L. Chrostowski, "Series-coupled silicon racetrack resonators and the Vernier effect: theory and measurement," *Optics Express*, vol. 18, no. 24, pp. 25151-25157, 2010.

[180] J. M. Ramirez *et al.*, "III-V-on-Silicon Integration: From Hybrid Devices to Heterogeneous Photonic Integrated Circuits," *IEEE Journal of Selected Topics in Quantum Electronics*, vol. 26, no. 2, pp. 1-13, 2019.

[181] M. Smit *et al.*, "An introduction to InP-based generic integration technology," *Semiconductor Science and Technology*, vol. 29, no. 8, p. 083001, 2014.

[182] Y. Han, W. K. Ng, Y. Xue, Q. Li, K. S. Wong and K. M. Lau, "Telecom InP/InGaAs nanolaser array directly grown on (001) silicon-on-insulator," *Optics Letters*, vol. 44, no. 4, pp. 767-770, 2019.

[183] N. Li, K. Liu, V. J. Sorger and D. K. Sadana, "Monolithic III–V on Silicon Plasmonic Nanolaser Structure for Optical Interconnects," *Scientific Reports*, vol. 5, no. 1, p. 14067, 2015.

[184] P. A. Morton, C. Xiang, J. B. Khugin, C. D. Morton, M. Trian, J. Peters, J. Guo, M. J. Morton and J. E. Bowers, "Integrated Coherent Tunable Laser (ICTL) With Ultra-Wideband Wavelength Tuning and Sub-100 Hz Lorentzian Linewidth," *Journal of Lightwave Technology*, vol. 40, no. 6, pp. 1802-1809, 2022.

[185] C. Xian *et al.*, "Laser soliton microcombs heterogeneously integrated on silicon," *Science*, vol. 373, no. 6550, pp. 99-103, 2021.

[186] A. Malik, J. Guo, M. A. Tran, G. Kurczveil, D. Liang and J. E. Bowers, "Widely tunable, heterogeneously integrated quantum-dot O-band lasers on silicon," *Photonics Research*, vol. 8, no.

10, pp. 1551-1557, 2020.

[187] C. Xiang *et al.*, "Narrow-linewidth III-V/Si/Si3N4 laser using multilayer heterogeneous integration," *Optica*, vol. 7, no. 1, pp. 20-21, 2020.

[188] M. -K. Kim, A. M. Lakhani and M. C. Wu, "Efficient waveguide-coupling of metal-clad nanolaser cavities," *Optics Express*, vol. 19, pp. 23504-23512, 2011.

[189] R. E. Burgess, Fluctuation phenomena in solids, New York: Academic Press, 1969.